Non-Cartesian MR Microscopy for Cancer Imaging in Small Animals

by

Prachi Pandit

Department of Biomedical Engineering
Duke University

Date:_________________________
Approved:

____
G. Allan Johnson, PhD, Supervisor

____
Gregg Trahey, PhD

____
Kathryn Nightingale, PhD

____
Carlo Tomasi, PhD

____
Daniel Sullivan, MD

____
Kevin King, PhD

Dissertation submitted in partial fulfillment of
the requirements for the degree of Doctor
of Philosophy in the Department of
Biomedical Engineering in the Graduate School
of Duke University

2010

ABSTRACT

Non-Cartesian MR Microscopy for Cancer Imaging in Small Animals

by

Prachi Pandit

Department of Biomedical Engineering
Duke University

Date:___________________________
Approved:

____
G. Allan Johnson, PhD, Supervisor

____
Gregg Trahey, PhD

____
Kathryn Nightingale, PhD

____
Carlo Tomasi, PhD

____
Daniel Sullivan, MD

____
Kevin King, PhD

An abstract of a dissertation submitted in partial
fulfillment of the requirements for the degree
of Doctor of Philosophy in the Department of
Biomedical Engineering in the Graduate School
of Duke University

2010

Abstract

Mouse models of cancer are an invaluable tool for studying the mechanism of the disease and the effect of new therapies. Recent years have seen an explosive growth in the development of such models and consequently there is an increased need for better imaging techniques to study them. The goal of this work was to develop a technique that satisfied the requirements for preclinical cancer imaging: high spatial resolution, good soft tissue differentiation, excellent motion immunity, fast and non-invasive imaging to enable high-throughput, longitudinal studies.

T_2-weighted and diffusion-weighted magnetic resonance imaging (MRI) has been shown to be effective for tumor characterization clinically. But translation of these techniques to the mouse is challenging. The higher spatial resolution and faster physiologic motion make conventional approaches very susceptible to phase artifacts. Additionally, at higher magnetic fields required for these studies, T_2^* and T_2 are significantly shorter and T_1 is longer, making in vivo imaging even harder.

A rigorous cancer imaging protocol was developed by optimizing and integrating various components of the system, including MR hardware, animal handling, and pulse sequence design to achieve reliable, repeatable and rapid imaging. The technique presented here relies heavily on the non-Cartesian sampling strategy of PROPELLER (Periodically Rotated Overlapping ParallEL Lines with Enhanced Reconstruction) MRI. The novel data acquisition and reconstruction overcomes the adverse effects of physiological motion, allows for rapid setup and acquisition and provides excellent tissue contrast. The sequence was optimized to enable T_2-weighted and diffusion-weighted imaging in

tumor-bearing mice with in-plane resolution of 117μm and slice thickness of 1mm. Multi-slice datasets covering the entire thorax and abdomen were acquired in ~30 minutes.

The imaging protocol developed here was applied to a high-throughput, longitudinal study in a mouse model of liver metastases. The liver is a common site of distal metastases in colon and rectal cancer, and if detected early has an improved prognosis. Unfortunately, severe respiratory motion make it hard to image. The relative merits of the proposed PROPELLER technique were analyzed with respect to the accepted gold-standard for abdominal cancer imaging, computed tomography (CT).

The non-Cartesian MR microscopy technique proposed here is a valuable tool in the "Cancer analysis toolkit". It allows for high-throughput, longitudinal experiments in free-breathing mice generating both structural and functional information with minimal artifacts and excellent spatial resolution. This work should find broad applications in various mouse models of cancer for studying the pathology of the disease, its progression as well as its response to treatment.

Dedicated to my grandmothers

Sudha Kogekar *and* ***Kusum Pandit***

two strong women in my life

who taught me

to always do my very best

and

to never accept anything less

Contents

List of Tables

List of Figures

List of Abbreviations

2D	2 Dimensional
3D	3 Dimensional
ADC	Apparent Diffusion Coefficient
BW	Bandwidth
CIVM	Center for In Vivo Microscopy
CNR	Contrast to Noise Ratio
CPMG	Carr-Purcell-Meiboom-Gill
CT	Computed Tomography
DWI	Diffusion-weighted Imaging
ESP	Echo Spacing
ETL	Echo Train Length
FDA	Food and Drug Administration
FID	Free Induction Decay
FOV	Field of View
FSE	Fast Spin Echo
FT	Fourier Transform
GE	General Electric
GRE	Gradient Echo
H&E	Hematoxylin and Eosin
IP	Intraperitoneal
NEX	Number of Excitations
MR	Magnetic Resonance

MRI	Magnetic Resonance Imaging
PROPELLER	Periodically Rotated Overlapping ParallEL Lines with Enhanced Reconstruction
QA	Quality Assurance
RARE	Rapid Acquisition with Relaxation Enhancement
RF	Radio Frequency
ROI	Region of Interest
SE	Spin Echo
SNR	Signal to Noise Ratio
T_1	Time constant for longitudinal magnetization recovery
T_2	Time constant for transverse magnetization decay
TE	Echo Time
TR	Repetition Time

Acknowledgements

I not only use all the brains that I have, but all that I can borrow.

*- **Woodrow Wilson** (28th President of the US)*

I would like to thank several brilliant and wonderful people who have helped and guided me on this journey. First and foremost, is my advisor Al Johnson. Al has been an exceptional mentor to me, not only in the scientific aspects, where he taught me to think critically, write precisely and to always be curious, but also, as he would say, in the "real-world" aspects. I am deeply indebted to him for presenting me with the opportunity to meet some of the best people in the field and teaching me through example the fine balance between modesty and confidence. Al always made sure that I never felt I was too far from home – from giving me a hard time for slouching in my chair to taking me to lunch and making me laugh with his anecdotes when I was going through a particularly stressful time. Thank you Al!

The most time I have spent with in the lab, has been with Yi Qi. Any success that I have achieved would have been impossible without her enthusiastic support and tireless dedication. Her grit, patience and commitment to perfection kept me on track during the highs and lows of this project. Her beautifully crocheted scarf kept me warm during the long hours in the freezing magnet room.

I thank Kevin King for the summer internship opportunity in 2007, where I first started working on PROPELLER. I am grateful to him for being available to answer all my questions ever since and for his continued interest, encouragement and guidance.

I wish to express my sincere gratitude to the other members of my thesis committee: Kathy Nightingale, Gregg Trahey, Carlo Tomasi, and Daniel Sullivan for taking an interest in my project and guiding me towards its completion. I am particularly grateful to Dr. Sullivan for steering me towards a harder, though finally, a much more comprehensive project in the final stages of my research

I would like to thank several collaborators. Jennifer Story and Beth Hollister from Piedmont Research Inc. were invaluable in providing numerous disease models and accommodating my crazy schedules and Duke's numerous rules. I thank Sam Johnston for his help with the CT studies and for patiently answering all my questions. I am grateful to Dr. Brian Berridge for humoring my lack of knowledge and abundance of curiosity while interpreting histology. I am indebted to Dr. Rendon Nelson for bringing in the clinical perspective to my preclinical work. He has been exceptionally encouraging during every interaction I have had with him. I wish I could have worked with him more.

All the wonderful people at CIVM helped create a highly productive and immensely enjoyable atmosphere for me during my five years here. I thank Gary Cofer for guiding me through the EPIC jungle of pulse sequence programming. I am appreciative of Lucy Upchurch for her ability to handle any crisis in the lab, and to do it cheerfully. She has taught me the importance of having the right attitude. I thank James Cook for "caring" when my computer revolted and ensuring that no data got lost. I am grateful to Larry Hedlund for generously sharing his photography skills and patiently accommodating my specific requirements, be it for my histology slides, or my visa ID photos. I thank Sally Zimney, Tawynna Gordon and Kathy Barbour for shielding me from ugly paperwork.

I am indebted to Bastian Driehuys for giving me access to his "career guidance center" and for enthusiastically sharing his insights on writing, science and life.

I have been lucky to experience the camaraderie of an excellent group of fellow students. In particular, I thank Nilesh Mistry and Gabe Howles for getting where I came from and for helping me grow up. I have enjoyed our friendship. I am grateful to John Nouls for helping me in designing phantoms, and giving me good advise in this final stretch, but mostly just for staying back in the lab. I am grateful also to Zackary Cleveland for his unique sense of humor that helped me put things in perspective when I was agonizing over tiny details. I thank Ergys Subashi for many hare-brained conversations, belly-aching laughs and breath-sapping triathlons. It has been fun!

I am immensely grateful to my best friends and roommates Leelavati Narlikar and Madhuwanti Vaidya, with whom I have spent the most memorable of times during my stay in Durham. I am also grateful to Prasant Potuluri for patiently showing me the way and being my own personal GPS for the last five years. I thank Prajakta Palkar for making my long hikes to and from the parking lot extremely enjoyable. Very special and heartfelt thanks to Mohsin Roowalla for his love and support, and for always knowing how to make me laugh out loud.

Finally, I would like to thank my family. I am deeply appreciative of the time that I got to spend with my grandparents, Balkrishna and Kusum Pandit, and Sadanand and Sudha Kogekar, and the impact it had on my value system. Thank you for teaching me through your own examples the importance of education, integrity and hard work.

To my brother, Chinmay Pandit, thank you for your support and wisdom, and for making me laugh when I called to cry. And most importantly to my parents, Nirmala and Ravi Pandit, thank you for your love and encouragement. Your faith in my abilities gave me the strength to start this journey and your pride in my achievements gave me the drive to follow it through.

Prachi Pandit
Duke University
April 2010

1. Introduction

1.1 Motivation

Cancer is a group of diseases characterized by uncontrolled growth and spread of abnormal cells. According to the American Cancer Society, it accounts for 23% of all deaths in the United States, second only to heart disease. Globally, the World Health Organization predicts, cancer deaths will increase from 7.4 million in 2004 to 11.8 million in 2030. Cancer can be reduced and controlled by implementing evidence-based strategies for cancer prevention, early detection and targeted treatment. Continued research for over a hundred years has provided us with extensive and ever-growing knowledge about the causes of cancer, and the interventions to prevent and manage it.

Animal models have been an essential tool in cancer research, and will continue to be so for years to come (de Dios, 2002). These models are created by transferring or inactivating certain genes to make the animals susceptible to cancer via the same factors that affect humans. The two main aspects of cancer research that have benefited from animal models are: (1) mechanistic studies of the genes/proteins/signaling pathways involved in cancer onset and progression; and (2) design, characterization and evaluation of new therapeutic approaches.

The most common animal models used for cancer research are mouse models. Mice have genetic and physiological properties similar to those of humans. Through the Mouse Genome Project, the entire genetic code for mice has been fully sequenced. Manipulating the genome with the knockout technique has traditionally been easier in the mouse than the rat, resulting in an abundance of mouse models of various cancers. Due to their small size, mice are easy and cheap to house. Finally, a short gestation period and a fast tumor growth rate make mice a more convenient model to study. Disease-related changes in the mouse can be observed in a matter of weeks, as opposed to years in larger animals or humans.

Traditionally, the easiest available means of studying cancer in animal models were end-point methods that involved biopsies and then conventional histology of the excised tissue. Large cohorts were necessary to demonstrate statistically significant results. Recent years have seen an increased interest in non-invasive imaging as a more rigorous means of studying such models. Longitudinally imaging the same animal at multiple timepoints can achieve more valuable information than would be obtained from multiple individual animals. In longitudinal studies, the animal acts as its own control, and the dynamic data collected is unambiguous.

Magnetic resonance imaging (MRI) is ideally suited for such applications. It is non-invasive and non-destructive. This allows for studies that can monitor changes in the same animal over time. It imposes no harmful radiation, nor does it induce any secondary effects that could potentially confuse the results of a cancer therapy study. MRI offers high spatial resolution and excellent soft tissue contrast. This facilitates accurate visualization of morphology and excellent delineation of structures. MRI is unique in its ability to provide contrast via a number of different mechanisms by changing certain imaging parameters. The different mechanisms are governed by different structural or functional properties of the tissues, making MR a very versatile imaging tool. MRI is also inherently digital; this permits easy quantitative data analysis.

The focus of this dissertation is to develop and implement a rigorous imaging protocol that will employ MR contrast mechanisms for tumor characterization in mouse models of cancer.

1.2 Challenges

Magnetic resonance microscopy in a live animal presents several challenges. The first challenge is the simultaneous demand of high spatial resolution and high signal to noise. A mouse is approximately 3000 times smaller than a man. To obtain a comparable definition of structure as that in humans, mice need to be imaged at much higher spatial resolution. Microscopy implies imaging at the microscopic scale (voxel size < 0.03 mm^3).

The image quality metric of particular importance when differentiating between healthy and cancerous tissue is the contrast to noise ratio (CNR). The second challenge is the acquisition of high CNR images at high field strengths necessary to overcome the first challenge. Field strength affects tissue relaxation properties. T_2^* and T_2 (transverse relaxation) decrease while T_1 (longitudinal relaxation) increases as the field strength increases. A combination of specialized hardware and customized pulse sequence is necessary for faster data acquisition to ensure sufficient signal and contrast while acquiring T_2-weighted images.

Long T_1 makes longer repetition times (TR) essential to assure sufficient recovery of longitudinal magnetization before the subsequent excitation. This increases the imaging time. This is the third challenge in this application. The imaging time needs to be minimized to enable high throughput. Another incentive for lowering imaging time is to reduce the time for which the animals are under anesthesia, an important criterion when considering sick animals.

The fourth challenge is the faster physiological motion in mice. The cardiac rate of a mouse is 10 times faster, and the respiratory rate is 5 times faster than that of a human. This causes considerable artifacts in the acquired data. Existing techniques that overcome this either lead to increased imaging time or increased animal trauma or both.

1.3 Specific Aims

The Center for In Vivo Microscopy has previously developed considerable infrastructure critical to this effort. This work extends it further for the specific preclinical application of high-throughout, longitudinal cancer imaging. The key phases of this work are:

1.3.1 Infrastructure development

1. Integrate specialized hardware for small animal imaging, including the static magnetic field, gradient coils, and RF coils.
2. Develop and streamline the animal handling protocol, including anesthesia and physiological signal monitoring, to ensure easy and rapid setup necessary for longitudinal, high throughput studies.
3. Design and develop quality assurance standards to ensure consistent and reliable results in longitudinal experiments.

1.3.2 Pulse sequence development

1. Identify and implement a suitable imaging sequence that satisfies the requirements of the study within the constraints of the infrastructure.
2. Develop the pulse sequence and the reconstruction technique to enable high-field T_2-weighted imaging.
3. Design and implement a novel imaging sequence for diffusion-weighted imaging.

1.3.3 Application to animal model

1. Identify an appropriate disease model and optimize the imaging parameters for that particular disease model.
2. Identify an acceptable gold standard for the particular model against which this work can be compared and validated.
3. Design and implement a high-throughput, longitudinal experiment to study the disease progression with both modalities, the technique developed here and the gold standard.
4. Develop a standardized Matlab routine to analyze the results across multiple mice and multiple timepoints, with both modalities.
5. Demonstrate the results and compare the advantages/disadvantages of the two modalities over various metrics, including spatial resolution, CNR, imaging time.
6. Validate the results with complimentary histology data.

2. Background

2.1 Non-invasive imaging

Non-invasive imaging techniques have revolutionized the way mouse cancer models are used in laboratories. These techniques have made it possible to study a broad range of tumor-relevant parameters at both the cellular and molecular level. Due to the non-invasive nature of these techniques, the same animal can be imaged at multiple time-points. This makes the animal its own control and the changes in the tumor parameters can be observed longitudinally. Another advantage of these techniques is the reduced number of experimental animals required to obtain statistically significant results.

These are some of the collective advantages of all non-invasive imaging techniques. Yet, no single imaging technique is ideal for all applications when it comes to imaging tumors in mice. Each modality has its own specifications that make it preferable for one application over another. Following is a brief review of a few of the most commonly used imaging techniques. Table 1 summarizes the salient features of each.

2.1.1 Nuclear Imaging

Nuclear imaging includes Positron Emission Tomography (PET) and Single Photon Emission Computed Tomography (SPECT). Both techniques are based on the detection of γ-rays arising from radioisotope decay. These are highly sensitive techniques for tumor imaging as they target the body's biochemistry or function as opposed to anatomy or structure. Careful design of the molecular probes enables targeting a specific molecular pathway. The cancer-specific pathways that can be imaged with PET and SPECT include mechanisms of gene expression, tumor hypoxia, and tumor metabolism. Unfortunately the lack of anatomical landmarks makes it difficult to localize the regions of specific activity in nuclear images. In recent years, multi-modality imaging has been gaining in popularity where PET images are co-registered with higher-resolution anatomical images acquired with either MRI or CT.

Table 1 :Comparison of commonly used non-invasive imaging techniques for murine cancer imaging (Koo et al., 2006; Lyons, 2005; Weissleder, 2002)

Modality	**Resolution**	**Acquisition time**	**Advantages**	**Disadvantages**
PET/SPECT	1 – 2mm	Minutes	High sensitivity	Low spatial resolution Radiation to animal
Optical Imaging	1-10mm	Seconds to minutes	High sensitivity	Low spatial resolution High attenuation with increased tissue depth
CT	100μm	Minutes	Good spatial resolution Good for lung and bone imaging	Poor soft tissue contrast Radiation to animal
MRI	100 -1000μm	Minutes to hours	Good spatial resolution Good anatomical and functional information	Low sensitivity Long acquisition time Long image processing time

2.1.2 Optical Imaging

There are two main types of Optical imaging techniques used for imaging tumors, Optical Bioluminescence Imaging (BLI) and Optical Fluorescence Imaging (FLI). Both techniques rely on detection of light emitted from within living tissue. FLI requires initial excitation of the fluorescent marker by a shorter wavelength light whereas in BLI the emission arises from the substrate itself. Planar images are acquired with a charge-coupled device camera. The main advantages of Optical Imaging are high sensitivity and ability of almost-continuous real-time acquisition. This technique is excellent for imaging organs and structures close to the skin surface, but finds limited use for imaging internal organs due to wavelength-dependent absorption and scattering of light by tissue, thus limiting the penetration depth.

2.1.3 Computed Tomography

Computed Tomography (CT) yields high-resolution anatomical images in small animals. CT contrast relies on the differences in the x-ray absorption properties of the tissues. Thus CT is good at differentiating bone and air from surrounding soft tissue. It is unfortunately not particularly good at differentiating between soft tissues, as there is little difference in their x-ray absorption. A number of iodine or barium contrast agents are in routine use to help in soft tissue delineation. The spatial resolution and sensitivity in CT depends on the radiation exposure and the amount of contrast agent. This can potentially limit the longitudinal utility of the study. Nevertheless, the high spatial resolution and fast imaging speeds make CT a good choice for high-throughput studies.

2.1.4 Magnetic Resonance Imaging

Magnetic resonance imaging (MRI) is a very versatile modality for imaging tumors in small animals as it provides both high-resolution anatomical information as well as functional information of tumor physiology. MRI is typically based on visualizing protons (^1H), owing to their abundance. Water, with two ^1H atoms in each molecule, makes up approximately 60% of the body. It also has a variety of biophysical magnetic signatures in different tissues that can be exploited to maximize contrast between healthy and diseased tissues. Over the last few years, MRI has been used for tumor detection, cancerous and precancerous tissue characterization, visualization of angiogenesis, etc. The non-invasive, non-destructive, non-radioactive nature of MRI makes it an ideal choice for longitudinal studies of mouse models. In addition, MRI offers a variety of contrast mechanisms that can be employed for visualizing different cancer biomarkers. The main disadvantages of MRI are the long acquisition and processing times and the relatively lower sensitivity compared to nuclear and optical imaging techniques. The main advantages are the high spatial resolution and the ability to obtain anatomical as well as functional information. MRI has the flexibility of setting up a wide range on experimental conditions (T_1, T_2, T_2^* - weighting) and chemical agents to enhance contrast. It is also sensitive to dynamic processes like diffusion, perfusion and flow, which are an excellent means for studying tumor vasculature and oxygenation.

This work focuses on Magnetic Resonance Imaging as the primary modality for in vivo cancer imaging in mice. Following is a brief explanation of the source of signal and contrast in MRI, specifically aimed at visualizing tumors in free-breathing animals.

2.2 Basics of Magnetic Resonance Imaging

2.2.1 Source of MR Signal

All spinning charged particles create electromagnetic fields. One such particle found in abundance in the human body is the hydrogen nucleus. The human body is approximately 60% water (H_2O) and 20% fat ($-CH_2-$), both of which have hydrogen (^1H). The hydrogen nucleus has a single proton with a spin angular momentum of either $+\frac{1}{2}$ or $-\frac{1}{2}$giving rise to a net magnetic field or a magnetic dipole moment to the nucleus. (Even number of nucleons in the nucleus pair up according to Fermi statistics, thereby canceling each other's magnetic fields, and causing the net magnetic field to be zero. Conversely, in the case of odd number of nucleons, one stays unpaired, giving rise to a magnetic dipole moment). In the absence of an external magnetic field, the axes of the magnetic dipole moments of the hydrogen nuclei are arranged in a random fashion and they cancel each other out. But in the presence of a strong external magnetic field

B_0, they align themselves in the direction of the magnetic field in one of two energy states, parallel or anti-parallel. The preference is to be in the parallel state (the lower energy state) and eventually over time more spins line up along the direction of B_0, causing a net magnetic moment M_0. This essentially is the source of signal in Magnetic Resonance Imaging.

The net magnetization M_0 precesses at the Larmor frequency ω_0 given by

$$\omega_0 = \gamma B_0 \tag{2.1}$$

γ, the gyromagnetic ratio is specific to the nucleus being magnetized. In the case of hydrogen, γ is 42.58 MHz/T.

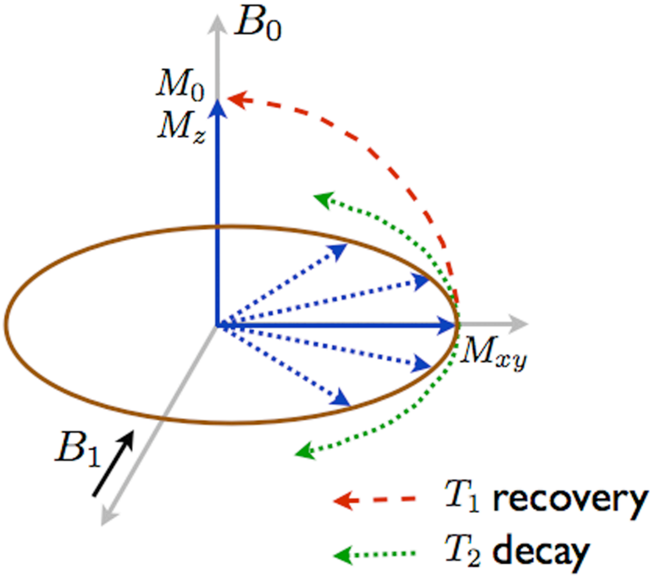

Figure 1: MR signal evolution in the presence of a static magnetic field B_0 and a rotating magnetic field B_1

The net magnetization M_0, when subjected to an RF pulse at the Larmor frequency in an orthogonal plane, experiences a torque that causes it to rotate. This RF excitation pulse

B_1 is chosen such that the net magnetization rotates on to the transverse plane. Figure 1 shows the progression of the magnetization.

Following the RF excitation, the longitudinal component of the magnetization M_z recovers to its equilibrium state of M_0 due to energy transfer from the protons to the surrounding lattice. This Spin-Lattice relaxation is defined by the time constant T_1.

$$\frac{dM_z}{dt} = -\left(\frac{M_z - M_0}{T_1}\right) \tag{2.2}$$

$$M_z(t) = M_0\left(1 - e^{-t/T_1}\right) \tag{2.3}$$

The transverse component of the magnetization M_{xy} decays to 0 through Spin-Spin relaxation. This occurs due to the dipolar interaction of spins with neighboring spins, causing them to lose phase coherence. Spin-spin relaxation is defined by the time constant T_2.

$$\frac{dM_{xy}}{dt} = -\frac{M_{xy}}{T_2} \tag{2.4}$$

$$M_{xy}(t) = M_0 e^{-t/T_2} \tag{2.5}$$

T_1 and T_2 are constants that depend on the tissues being imaged and form the basis of much of the contrast in MRI.

A pulse sequence is a series of RF and gradient pulses that is applied to a spin system to manipulate the magnetization of that spin system and spatially encode the resulting RF signal. An RF excitation pulse causes the equilibrium magnetization to tip onto the transverse plane, thereby causing a free induction decay (FID) to form. For conventional RF and gradient refocused sequences, the FID is refocused in the transverse plane to form a spin or gradient echo. This occurs at the Echo Time (TE). The time between two consecutive excitation pulses is the Repetition Time (TR). The magnitude of the resulting MR signal, S is given by

$$S \propto \rho M_0 (1 - e^{-TR/T_1}) e^{-TE/T_2} \tag{2.6}$$

where ρ is the spin density.

Spin echo and gradient echo are two of the most frequently used sequences. A spin echo (SE) sequence uses two RF pulses to form an echo, whereas a gradient echo (GRE) sequence uses a single RF pulse followed by gradient pulses. The GRE sequences are typically faster than the SE sequences, but they have the disadvantage of being more influenced by magnetic field inhomogeneity. This causes changes in the relaxation parameters (specifically T_2^*), which affects the contrast in the image.

2.2.2 MR contrast mechanisms for cancer imaging

Contrast in an MR image is obtained by manipulating the various timing parameters in a MR sequence. As seen in the earlier section, changes in TE and TR change the amount by which the total MR signal is weighted by the relaxation properties T_1 and T_2 to provide T_1-weighted and T_2-weighted contrast respectively. Both these types of contrasts are used extensively for imaging cancer. This section gives a brief explanation of these two contrast mechanisms (Bloembergen et al., 1948), along with a third mechanism dependent on local spin diffusion – diffusion-weighted contrast, in the context of cancer imaging.

T_1-weighted contrast

The image acquisition parameter that affects T_1 contrast is TR. T_1 is the longitudinal magnetization recovery time. Tissues with short T_1 values recover faster than those with long T_1 values. Thus as can be seen from Fig. 2, at long TR both tissues have recovered and have comparable signal intensities, while at short TR the difference between the tissue signal is maximized.

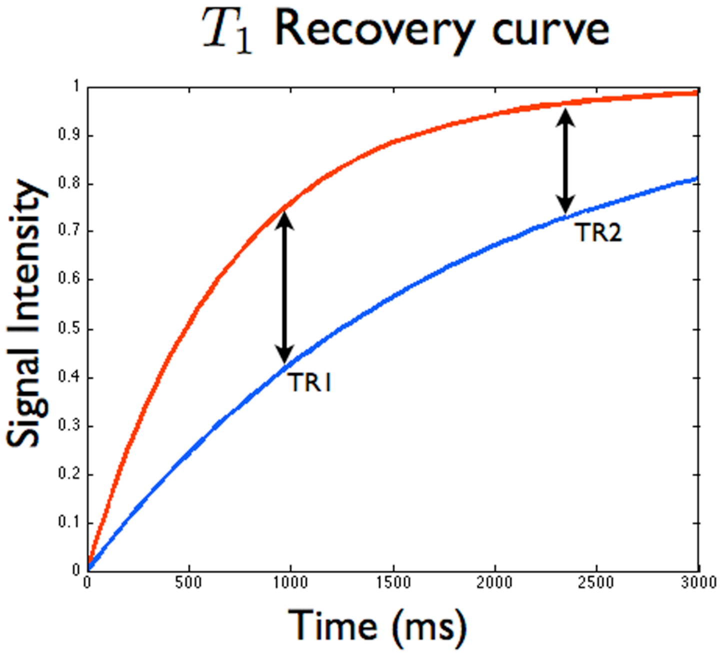

Figure 2: Recovery curves for longitudinal magnetization - Source of T_1 contrast

T_1 relaxation is caused by energy exchange between spins and the surrounding lattice by the process of molecular tumbling. Collisions due to molecular tumbling cause a constant change in molecular movement (rotation, vibration, translation). The duration at which these changes occur is the correlation time (τ_C), and the number of nuclei that tumble at the associated frequency is described by the spectral density function J(ω). Effective T_1 relaxation occurs when J(ω) has energies that match the Larmor frequency.

T_1 is dependent on magnetic field strength; tissue T_1 is longer at higher fields (Bottomley et al., 1984; DiFrancesco et al., 2008). At higher frequencies, the spectral density function decreases and energy exchange is inefficient. As the Larmor frequency at higher fields is higher, the T_1 is lengthened.

T_1 can be altered by exogenous contrast agents. These are external agents that can be introduced into specific targeted tissues where they act to reduce the T_1 of that tissue. There are several applications where T_1-shortening contrast agents are used as they improve the contrast and the signal in the image in addition to reducing the imaging time. In the context of cancer imaging, intravenous contrast agents are used for dynamic contrast enhanced (DCE) MRI to measure abnormalities in tumor, including vessel flow, blood volume, and permeability.

T_2-weighted contrast

T_2 contrast is governed by the choice of TE. T_2 is the time required for the transverse magnetization to decay. At longer TE, the difference between the tissues with short T_2, that have lost more of their transverse magnetization and tissues with long T_2, that still retain theirs, increases. This can be seen from Fig. 3.

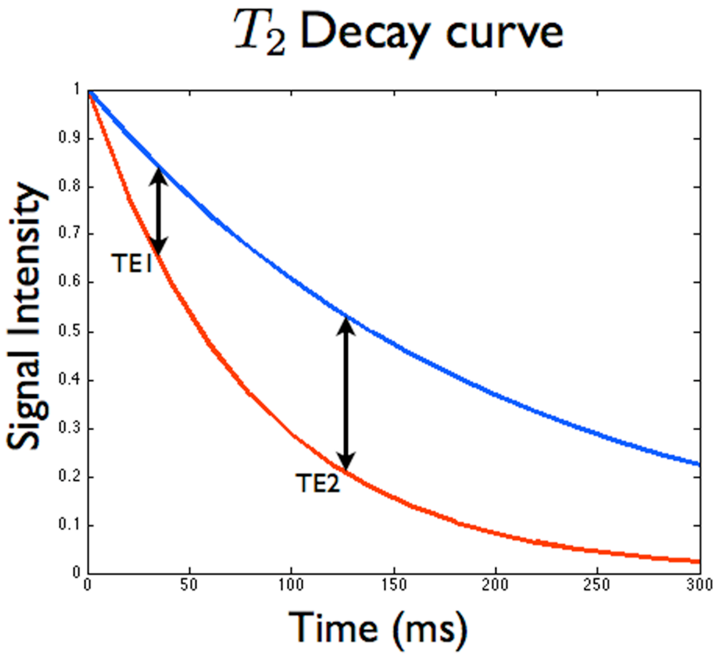

Figure 3: Decay curves for transverse magnetization - Source of T_2 contrast

T_2 relaxation is caused by loss of phase coherence between spins, which arises from intrinsic magnetic field inhomogenieties, i.e internal to the proton system. For a rapidly tumbling molecule (free protons), the rapid fluctuations in the local magnetic field average out and it sees a relatively homogenous local field and hence undergoes little dephasing resulting in long T_2. Conversely, a slowly tumbling molecule (bound protons), sees a fairly static magnetic field inhomogeniety and is hence more effectively dephased, resulting in short T_2.

T_2 also changes with field strength. At higher field strengths, due to chemical exchange between bound and bulk water in tissues, the tissue T2 decreases (DiFrancesco et al., 2008; Zhong et al., 1989).

Cancer is characterized by disrupted cellular structure and sometimes higher water content. This causes variations in the tissue relaxation properties; for example, cancerous tissue typically has a longer T_2 than the surrounding normal parenchyma. T_2 values are also much smaller than T_1 values and hence a small increase in T_2 corresponds to a larger percentage increase than the same increase in T_1. This makes T_2 a more sensitive indicator of structural changes arising from disease. In the cancer context, T_2-weighted imaging is extensively used due to its excellent soft-tissue contrast and the absence of contrast agent administration.

Diffusion-weighted contrast

The decay of the transverse magnetization is governed by the spin-spin interactions, and the fluctuations in the local magnetic field. A third factor that also affects the transverse magnetization, and is a much used contrast mechanism for cancer imaging, is the self-diffusion of water molecules. Water molecules undergo constant random Brownian motion. In the presence of a magnetic field, this diffusion of protons from one region to another causes alterations in the local magnetic field of the protons, causing differences in their precession rates and hence dephasing of the net magnetization. These effects are very small compared to the T_2 decay and are normally ignored, but if a large magnetic gradient is applied concurrently, the dephasing effect is amplified and the signal decay is significant. The resultant magnetization is then given by

$$M_{xy}(t) = M_0 e^{-t/T_2} e^{\left(-\gamma^2 G^2 D t^3 / 3\right)} \qquad (2.7)$$

where G is the applied gradient and D is the diffusion constant. The signal decay is indicative of the diffusion of water molecules over distances comparable to cell dimensions. The amount of diffusion is affected by various tissue properties, like molecular viscosity, membrane permeability between intra and extra cellular compartments, directionality of structures within the cells that impede or enhance water mobility as well as the actual water content in the cells. These properties of tumor tissues change over the course of the disease; for example, viable tumor cells with intact membranes restrict water diffusion whereas necrotic tumors with disrupted membrane have increased water diffusion. These differences are exploited in diffusion-weighted imaging to obtain functional information in cancer studies.

2.3 Literature Review

This section provides a brief literature review, with special attention paid to reports of MRI in mouse models of cancer. With significant advancements being made in the MR imaging technology as well as the added interest in studying animal models of diseases, recent years have seen a lot of progress in the field of preclinical cancer research.

In small animals, MRI has been used for studying cancer of various different organs, such as pancreas (Grimm et al., 2003), liver (Baboi et al., 2009; Cai et al., 2005; Gambarota et al., 2008), brain (McConville et al., 2007), colon (Mook et al., 2008), breast (Jansen et al., 2008), prostate (Degrassi et al., 2007; Fei et al., 2007; Nastiuk et al., 2007).

MRI is now not only being used to study macroscopic effects of cancer, like changes in tumor volume, but also to detect changes that take place at cellular and molecular levels. Development of targeted contrast agents has further expanded the boundaries of cancer imaging. A wide range of imaging techniques is being used to capture various aspects of cancer, like tumor cell apoptosis (Blankenberg, 2008; Brindle, 2003; Kim et al., 2008), angiogenesis (Saxena et al., 2007), cell movement tracking, tumor staging (Baboi et al., 2007; McConville et al., 2007), etc.

Due to the various different kinds of cancers and the different organs that they affect, there is no single technique that works best for all cancer imaging studies. Nevertheless there are some common criteria that must be met by all high throughput, longitudinal preclinical studies. The next chapter discusses the requirements of such a small animal cancer imaging protocol.

3. Requirements for a Cancer Imaging Protocol

A cancer imaging protocol, as defined in this body of work, is a set of procedures that can be collectively used for tumor detection and characterization by employing various contrast mechanisms depending on the type of tumors that are being studied. Such a protocol has to be safe, affordable, non-invasive and with a low rate of false positives. It also needs to be able to cover the whole mouse, while at the same time be reasonably fast so as to enable high throughput.

This chapter describes the requirements of a Cancer Imaging protocol in mice and the challenges that they present. Solutions to the specific challenges have been mentioned in brief, while the details are presented in Chapters 4 and 5.

3.1 High spatial resolution

An average mouse weighs about 25g. That makes the mouse over 3000 times smaller than a 70kg human. Thus scaling down the MR imaging to get as relevant a data from a mouse is not a trivial task. To get comparable definition and delineation of structure so as to enable the detection of the smallest of tumors, much higher spatial resolution is needed. Typical spatial resolution used for cancer imaging in humans is 1-2mm (5mm slice). In the case of mice, the goal is to be able to image at planar resolutions in the range of 50-150μm and slice thickness of 1mm.

The higher spatial resolution in murine imaging is achieved by imaging at high fields. Typical clinical scanners are 1.5 - 3T. The imaging in this study was carried out on a 7T magnet. In MRI, signal increases with increasing magnet strength

$$SNR \propto B_0^{\left(1\,to\,\frac{7}{4}\right)} \tag{3.1}$$

The SNR increase is lower when the subject noise is much greater than the electronic noise and higher when it is much less. In the small animal, the gain is somewhere between these two extremes. This gain in signal is used to obtain higher spatial resolution. But imaging at high fields has its own set of challenges. At higher fields, the tissue T_1 is longer and the T_2^* (higher susceptibility losses) and T_2 are significantly shorter. This results in slower longitudinal recovery and faster transverse decay.

3.2 High contrast resolution

MR imaging provides a variety of contrasts that are indicative of inherent tissue properties like T_1, T_2, T_2^* and diffusion, and which can be used to characterize different tissues, differentiate between healthy and diseased tissue, visualize tumor vasculature, etc. The focus of this work is primarily on T_2-weighted contrast, for tumor detection and characterization (diseased tissue has a higher T_2 as compared to healthy tissue), and diffusion-weighted contrast to obtain quantitative information regarding the cellular properties of the tumor tissue.

As noted in the earlier section, getting good contrast resolution at higher fields is not straightforward. Both hardware and software optimizations are necessary to overcome this challenge. The high duty cycle gradient coils on the 7T magnet have a rise time of 100μs and maximum strength of 77 G/cm. This enabled faster imaging and helped minimize the impact of the rapid signal loss associated with the shorter T_2* at high fields.

Additionally, novel encoding strategies that use multi-echo acquisitions to minimize T_2^* losses and enable better T_2 and diffusion contrast were developed and implemented. The details are provided in Chapters 5 and 6.

3.3 Large field of view

A cancer screening protocol, as defined here, implies a need to examine as large a region as possible. This requirement is particularly important in the case of metastatic and spontaneous internal tumor models.

Due to the differences in the anatomy and the resolution scales used, imaging the mouse brain and imaging the mouse body are two very distinct tasks. In this work, the focus is primarily on imaging the mouse body, from the neck to the flank, and will henceforth be referred to as whole body imaging. Thus the volume to be covered is about 5cm x 3cm x 3cm. This requires an RF coil that is homogeneous over that big a region. It is also important that the coil not be too large as compared to the object volume, as that has the adverse effect of minimizing SNR. The System Integration chapter of this document gives more details of the hardware used to address the large field of view requirement.

3.4 Immunity to motion

Movement during the course of data acquisition causes artifacts in images. In live subject imaging, this movement is due to physiological processes like respiration and the beating of the heart. The respiratory rate of a mouse is about 5 times faster than that of humans and the cardiac rate is about 600 beats/minute compared to about 60 beats/minute in humans. The respiratory motion particularly affects the organs in the abdominal cavity, which is the region that this study is targeting. Thus immunity to motion is one of the prime requirements for our cancer imaging protocol in mice.

The traditional approach to dealing with motion has been to acquire respiratory and/or cardiac gated images. This significantly improves the image quality, but it also increases the image acquisition time as well as the animal preparation time. This problem has been addressed by implementing a non-Cartesian encoding technique, which, due to oversampling of data in the central regions of k-space and the trajectory used for data collection, is inherently insensitive to motion. Chapters 4 and 5 cover this aspect of the dissertation in greater detail.

3.5 High throughput

A high throughput in vivo imaging protocol requires efficiency in two aspects of the study: the animal preparation time, and the actual imaging time. In these studies the mice will be free-breathing. This drastically reduces the animal setup, as it is no longer necessary to intubate the mice. Intubation, in addition to being time consuming, is also difficult to perform on mice and has a high mortality rate. The animal setup chosen for this protocol requires less than 10 minutes and is very efficient due to the integrated positioning and monitoring apparatus that is being used for the study. The details of the animal setup are provided in the System Integration chapter.

Using an appropriate imaging technique that takes into account the limitations imposed on such a study helps minimize the imaging time. At high fields, tissues have longer T_1 relaxation times and hence the repetition time (TR) between excitations in the imaging sequence has to be longer that that used at lower fields (~3s). Efficient use of this down time can be made by the right choice of pulse sequences used for data acquisition. The section on MR encoding strategies in Chapter 4 gives a comprehensive explanation on the choice of the multi-slice, multi-echo sequence that is used in this protocol to minimize imaging time.

3.6 Longitudinal ability

An important requirement for the cancer imaging protocol is the ability to carry out longitudinal experiments so that it can be applied for a biologically relevant preclinical study. Thus the protocol needs to be repeatable and consistent so that data acquired over multiple imaging sessions can be registered and used together to glean quantitative information over the course of the study. This need is met by using an easy, unambiguous animal setup with a consistent positioning apparatus. The anesthetic regime used during the studies and the constant monitoring of the physiological signals ensures animal survivability, which is of utmost importance, especially taking into account the already compromised state of the animals. Chapter 4 provides the details of the animal handling procedures used for this protocol.

3.7 Measurement consistency (Quality control)

Tied in closely with the longitudinal ability is the requirement to assess the accuracy, consistency and the reproducibility of the results. A rigorous preclinical cancer study requires imaging many different mice over multiple time-point. The analysis of the acquired data relies on the assumption that the imaging sequence yields the same baseline signal in each case. However, signal intensity in MR experiments can change between acquisitions for reasons other than the underlying biology that is being studied. These changes can be related to the MRI system – instability of the excitation pulse, eddy currents, etc. Also, since the mice have variable tumor burden, both between mice and between time-points, there are variations in the RF coil match and tune, causing further changes in signal intensity. Thus it is important to be able to normalize the acquired information so that the quantitative parameters extracted from the data are consistent. A quality control phantom with known imaging markers was designed and used during the studies to satisfy this requirement. Chapter 4 provides further details. In the case of diffusion-weighted imaging, the phantom served an additional function; this is presented in Chapter 6.

4. System Integration

Though the core of this research is pulse sequence development, designing a protocol for in vivo cancer imaging in mice involves much more than just that. For a thorough, biologically relevant study to be undertaken, all components of the system – including the magnet, coils, animal handling, and protocol QA, need to be optimized. This chapter discusses the main components of system integration that are necessary to ensure reliable, repeatable and rapid imaging that fulfills the requirements defined in Chapter 3.

4.1 MR Hardware

4.1.1 Main magnet and gradient coils

Table 2 shows the comparison between a human and a mouse. To acquire the level of structural detail comparable in scale to clinical imaging, mice need to be imaged at planar resolutions in the range of 50-150 μm. The higher spatial resolution is obtained by imaging at higher magnetic fields (Marzola et al., 2003).

Table 2: Human to mouse comparison

Parameter	Human	Mouse
Weight (kg)	70	0.02
Breathing rate (breaths/min)	20	100
Heart rate (beats/min)	60	600

All the imaging studies were carried out on a 7T, 150 mm bore, Magnex magnet with a GE EXCITE console on the EPIC Lx12M4 software platform (GE Healthcare, Milwaukee, WI).

As mentioned earlier, high fields are associated with rapid signal decay due to higher susceptibility-induced losses (DiFrancesco et al., 2008; Malisch et al., 1991; Zhong et al., 1989). To ensure sufficient signal and contrast while acquiring T_2-weighted images, it is important to be able to acquire data with as short an inter-echo spacing as possible.

Figure 4: 7T magnet with GE EPIC console

This need was met by a specialized set of hardware. The 7T magnet uses shielded gradient coils (Resonance Research Inc., Billerica, MA) with a maximum gradient strength of 770 mT/m and a rise time of 100 μs. High power amplifiers (Copley Controls, Canton, MA) drive the gradients. The comparison between the Resonance Research gradient coils and standard clinical gradient coils is shown in Table 3. The strong gradients with high slew rate, high duty cycle and high power amplifiers enabled compact sequences, i.e. shorter echo spacing, and hence less time between acquisitions where signal loss could occur.

Table 3: Comparison of a standard clinical system with the 7T small animal system

Parameter	Clinical System	Animal System
Field strength (T)	3	7
Gradient strength (mT/m)	40	770
Gradient rise time (μs)	286	100

4.1.2 RF coil

Radiofrequency coils are used for two main functions – exciting the magnetization in the specimen, and receiving the signal from the excited spins. The prime considerations for a RF coil are homogeneity of the magnetization transmit response (excitation pulse) and the sensitivity and uniformity of the RF receive response. It is important to have a coil that is homogeneous and highly sensitive over the entire field of view being imaged. Another requirement from the coil is that the coil volume be as close to the object volume as possible so as to maximize the SNR.

Figure 5: M2M Quadrature RF coil used for murine imaging

A 35 mm diameter quadrature transmit/receive volume coil (M2M Imaging Corporation, Cleveland, OH) was purchased for these studies (Fig. 5). This coil is easy to match and tune for mice ranging in weight from 20-30g. It is homogeneous over a 5cm range at the center of the coil and the circumference is such that a mouse fits snugly in it.

4.2 Animal Handling

One of the main components of our protocol that needed particular attention was the animal handling procedures, since the animals were frequently quite sick. The requirements that govern the choices made in this aspect of the work are the need to enable high throughput and longitudinal studies on tumor-bearing mice. With this in mind, the animal handling system had to provide for the following:

i. Minimal animal preparation time
ii. Limited invasive procedures
iii. Safe and reliable chemical restraints
iv. Reliable physiological monitoring
v. Reproducible positioning

4.2.1 Chemical restraint and physiological monitoring

A number of different anesthesia approaches were examined. The first approach was intubating the mouse and ventilating with inhaled Isoflurane. This provided greater control over the respiratory motion, but intubation is a time-consuming process with a high mortality rate. In addition, the procedure was much too invasive to allow proper recovery of the mouse. Thus this satisfied neither the high throughput nor the longitudinal requirement. The second approach to be tested was intraperitoneal injections of Nembutal and Butorphanol. This is less traumatic for the animals, but injectable anesthetics have a short therapeutic window. Thus to ensure that the animal stayed anesthetized over the course of the imaging sessions, it was necessary to place an IP catheter. As the focus of this study is abdominal imaging, the catheter was right in the field of view (FOV). Additionally, due to intraperitoneal delivery, the response of the anesthetic was slower, making precise control harder.

The anesthetic approach that was most effective was inhaled Isoflurane . The Isoflurane was delivered via a nosecone. The fast response time of Isoflurane, along with continuous monitoring of animal respiration, provided the most precise control for the chemical restraint. The animals in this case were left to breathe on their own. This minimized the animal preparation time and maximized the animal survival rate. Novel imaging strategies (described in Chapters 4 and 5) minimized the artifacts associated with motion arising from the free-breathing animals.

All animal procedures followed the Duke Institutional Animal Care and Use Committee (IACUC) guidelines. The temperature (thermocouple probe) and the breathing rate (pressure pillow) of the mouse were continuously monitored (SA Instruments Inc.) and used to regulate the anesthetic dose and the body temperature of the animal. This ensured that the mice stayed anesthetized over the duration of the study without compromising their survival.

4.2.2 Animal positioning

Reproducible and rapid animal positioning is critical in this study. For longitudinal studies, the cancer imaging protocol needed to be repeated on the same animal a number of times during the course of disease progression. Thus consistent positioning of the anatomical landmarks was necessary to enable easy image registration of these various datasets. Secondly, the animal positioning system needed to accommodate the anesthesia delivery system and the physiological monitoring hardware. Thirdly, it needed to be adjustable so that animals with varying size and tumor burden could be positioned easily and fast. And lastly, it needed to fit easily and snugly at the center of the RF coil. The animal cradle designed by Gabriel Howles-Banerji, a graduate student at the CIVM, met these requirements, and was chosen for this study.

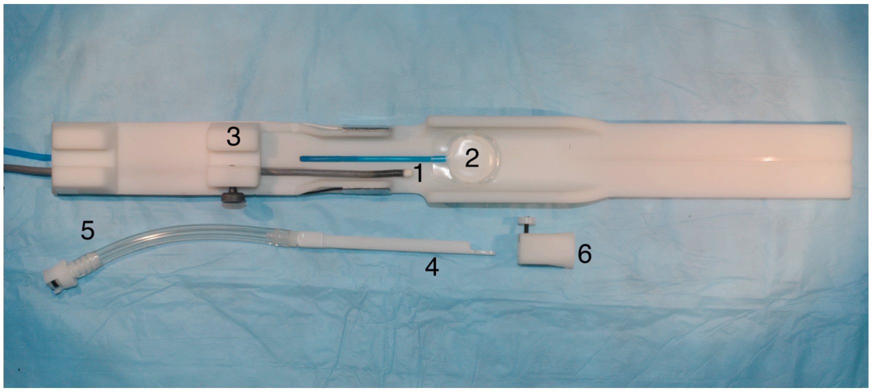

Figure 6: The integrated mouse cradle. Temperature probe (1) and respiratory pillow (2) used for physiological signal monitoring. A bracket with a thumbscrew (3) secures the drawbar assembly. The drawbar (4) delivers Isoflurane anesthesia from an incoming line (5) directly to the animal's nose. The nosecone (6) slides over the drawbar where the animal incisors are inserted and is clamped down.

Figure 6 shows the integrated animal cradle (Howles et al., 2009). The top component in the figure shows the main cradle that holds the mouse and the monitoring transducers – temperature probe (1) and respiratory pillow (2). A bracket with a thumbscrew (3) secures the drawbar (4), which has a small hole where the incisors of the mouse are inserted. The nosecone (6) slides over the drawbar and is clamped down. The Isoflurane is delivered from the incoming line (5) directly into the animal's nose. The mouse is positioned in the cradle with its abdomen over the respiratory pillow. The temperature probe sits snuggly under the neck to measure the surface body temperature. The animal cradle slides easily into the RF coil and is securely and consistently positioned to ensure that the desired region of interest (the abdomen, in this case) is at the center of the coil.

With these optimized animal-handling procedures, the animal setup time was reduced to less than 10 minutes, and the animal survival rate was up to 100%.

4.3 Quality control for imaging consistency

Rigorous analysis of a biological model necessitates repeatable results from a large sample of animals, often times acquired longitudinally. Thus it is important to have some known markers in the image to ensure consistent measurement.

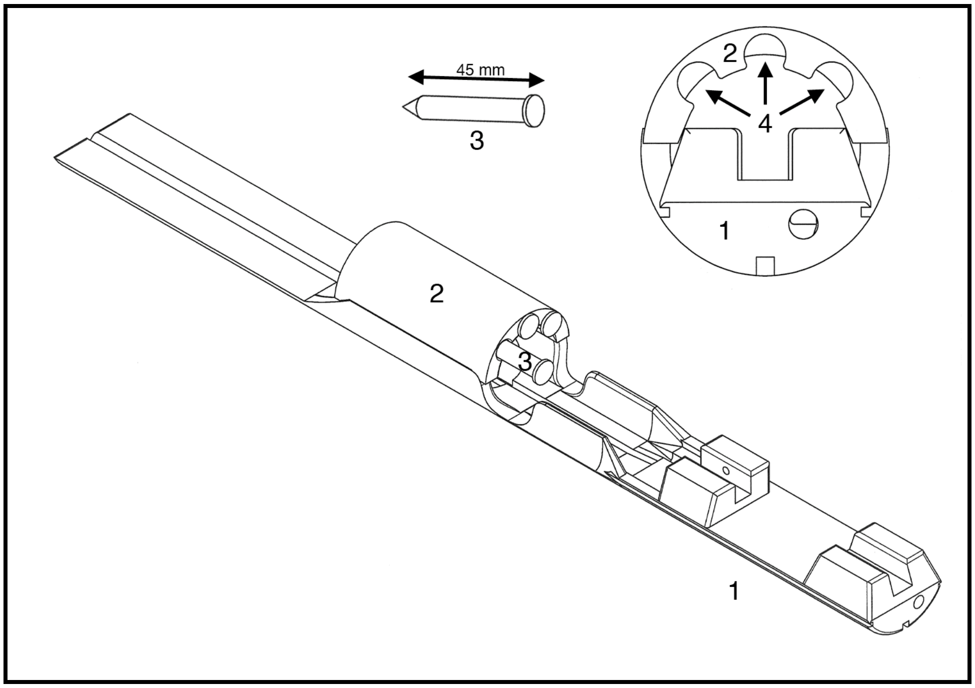

Figure 7: QA phantom with animal cradle. Up to three phantom vials (3) can be placed in the holder (2), which clicks into place over the walls of the animal cradle (1). The front view (top-right) shows the three notches (4) where the phantom vials are inserted.

A phantom holder that could hold upto three vials with different marker solutions was designed for this purpose. This holder was fabricated to fit on top of the animal cradle, in such a way that it did not push down on the mouse and distort its body.

Figure 7 shows the phantom along with the animal cradle. The phantom holder (2) snaps on the walls of the animal cradle (1) and the whole assembly slides in and fits snuggly into the RF coil. The holder has three notches (4) that run along its length to accommodate upto three vials (3) for different marker solutions. These vials can be easily slipped in and out of the holder.

4.3.1 T_2-weighted imaging

The main purpose of the marker phantom for the T_2-weighted imaging studies was to ensure consistency and reproducibility in the acquired data. As noted earlier, the signal intensity in a MR experiment can change between acquisitions due to various system parameters. Thus two vials with known marker solutions were placed in the imaging FOV to track inter-scan signal intensity variations. The two marker solutions used in the longitudinal T_2-weighted imaging studies were:

1. 3% Agarose solution

   The agarose solution was chosen as it has relaxation properties equivalent to those seen in tissues (Mitchell et al., 1986), and when prepared properly is exceedingly stable. The standard procedure (Mitchell et al., 1986; Walker et al., 1988) were followed to create this phantom.

2. $CuSO_4$ solution diluted with D_2O

   The second solution to be used was distilled water doped with a low concentration of $CuSO_4$ (1.8g/l) (Delakis et al., 2004). The signal levels from this solution were found to be much higher than those obtained from the mouse body. This reduced the dynamic range of the signal within the mouse body and hence the phantom solution was further diluted with D_2O to reduce the signal intensity (3:1 dilution).

Both the phantom vials (plastic tubes) were completely filled with the marker solutions and sealed with Parafilm to make them airtight. This ensured that the markers remained stable over the course of the study. The $CuSO_4$ marker corresponded with the higher signal intensity levels in the mouse, while the Agarose marker corresponded with the intermediate intensities.

4.3.2 Diffusion-weighted imaging

For the diffusion-weighted imaging, in addition to the above, the quality control phantom fulfilled another important function – extraction of quantitative diffusion information. Without the knowledge of the novel imaging sequence used for these DWI studies, an extensive explanation is not possible at this stage. Chapter 6 provides a detailed description. In brief – with the diffusion-weighting strategy used in this study, analytical calculation of b-values is not straightforward. A more feasible technique in this case is to back-calculate the b-values using known ADC values, for the different diffusion-weighting steps. Thus for the DWI studies, the markers were also used as the known ADC values (or controls).

A number of different solutions (Delakis et al., 2004; Laubach et al., 1998) with different ADC values were used. The ADCs for these solutions were measured using a standard Cartesian spin echo sequence (Stejskal and Tanner, 1965). As the diffusion coefficient is temperature dependent, the temperature was maintained between 33-34°C during the course of the experiment. This corresponds to the temperature range used for the animal studies. Table 4 summarizes the different markers used.

Table 4: Marker solutions and their measured Apparent Diffusion Coefficients (ADC)

Solution	Apparent Diffusion Coefficient
3% Agarose	2.66×10^{-3} mm^2/s
2% Agarose	2.77×10^{-3} mm^2/s
$CuSO_4$ (2:1 dilution with D_2O)	2.08×10^{-3} mm^2/s
$CuSO_4$ (3:1 dilution with D_2O)	1.98×10^{-3} mm^2/s
Sucrose solution (400g/l)	0.92×10^{-3} mm^2/s

4.4 Software – MR encoding strategies

The preceding three sections describe the hardware that has been optimized to meet the requirements of this study. The final part of the system integration is the software, namely the MR encoding techniques used to acquire data. The MR pulse sequence satisfies the remaining requirements:

1. Immunity to motion

   With the decision of using free-breathing mice for this study, image artifacts arising due to respiratory and cardiac motion are of prime concern.

2. Reduced imaging time

   For a high-throughput study, in addition to minimizing the animal preparation time, the actual data acquisition time also needs to be minimized.

3. High contrast resolution

   The goal of this study is to enable tumor visualization in mouse models. Thus it is critical to achieve excellent contrast between diseased tissue and normal parenchyma. The contrast mechanisms that this study targets are T_2-weighted and diffusion-weighted contrast.

Preliminary work

The main focus of this work has been the development of specialized MR pulse sequences. Starting with the basic spin echo sequence, it was progressively optimized to finally implement an efficient sequence for imaging cancer in mice. This section provides a summary of the preliminary work done during pulse sequence development. Subsequent chapters provide a rigorous analysis of the final sequences that were used for the cancer study.

Multi-slice Spin Echo Acquisition

For whole body imaging in mice, there are two possible MR imaging approaches - 3D volumetric acquisitions or 2D multi-slice acquisitions. Each approach has its own set of advantages and disadvantages.

In 3D volumetric imaging, a thick slab or the whole object is excited using an RF pulse and then phase encoding is applied in the through-plane direction to enable encoding in that plane. This is in addition to the regular in-plane phase encoding. In contrast, for 2D multi-slice imaging, the RF pulse itself is used to excite a slice, which is typically thinner than the slab used in 3D encoding. Much better resolution can be obtained in the through-plane direction in 3D imaging as compared to 2D multi-slice imaging. This is because there are inherent limits to obtaining a perfect RF excitation profile, whereas it is much easier to increase the number of phase encoding steps. Nevertheless, a slice as thin as 800 μm can be acquired with the 2D approach. The in-plane resolution in both cases is equivalent and the sensitivity of both approaches is also equivalent (Johnson et al., 1999). Due to the three-dimensional Fourier encoding used, 3D images have much larger datasets and hence require more memory and processing time during reconstruction. Additionally, data corruption (due to motion or hardware malfunction) in even a single acquired line causes artifacts in the entire dataset, whereas in 2D multi-slice acquisitions only that particular slice is affected. Another important difference between the two techniques, which is of particular importance for this application, is the difference in image acquisition times. As already noted, the tissue T_1 at high fields is very long, and hence to obtain good T_2-weighted images, a long repetition time (TR ~ 3s) is necessary to allow sufficient T_1 recovery. Due to the volume excitation used in 3D imaging, a single line of k-space can be acquired in one TR, thus making the total imaging time prohibitively long. On the other hand, in 2D multi-slice imaging, the long TR can be used efficiently by employing multiple RF excitations centered at different frequencies to acquire a k-space line from each slice in the total volume. Thus a choice was made to implement a multi-slice 2D sequence as opposed to a 3D volumetric sequence. This is intimately tied to one of the requirements defined for this work – high throughput imaging.

The second choice regarding the MR imaging sequence was between gradient echo (GRE) and spin echo (SE) acquisition. The SE sequence is a much more robust sequence for T_2-weighted imaging, especially if the external field is not particularly homogeneous. In a non-uniform field, the external field induced T_2' is much smaller than T_2.

$$\frac{1}{T_2^*} = \frac{1}{T_2'} + \frac{1}{T_2} \tag{4.1}$$

Thus the former dominates the latter and severe extrinsic signal loss is observed. The T_2' signal loss can be recovered (reversed) by refocusing the magnetization as is done in SE acquisition, thereby, making it possible to acquire a T_2-weighted image as opposed to a T_2^*-weighted. Thus this work focuses on SE acquisitions.

As the first step in the pulse sequence development process, a Cartesian multi-slice spin echo sequence was implemented. We chose to write an in-house sequence in EPIC Lx12M4 as opposed to using a standard product sequence provided on the GE Excite console. The GE sequences have been developed for clinical imaging and have FDA-imposed limits for patient safety. These translate as limits on gradient strength as well as gradient switching rates, thus making inefficient use of the gradient amplifiers and high-strength gradient coils available at the CIVM.

Figure 8 shows the k-space trajectory (Fourier domain data acquisition order) and the pulse sequence diagram for the Cartesian multi-slice SE sequence. This was the first multi-slice sequence implement at the CIVM as most work here had historically relied on 3D volumetric acquisitions for high-resolution MR microscopy.

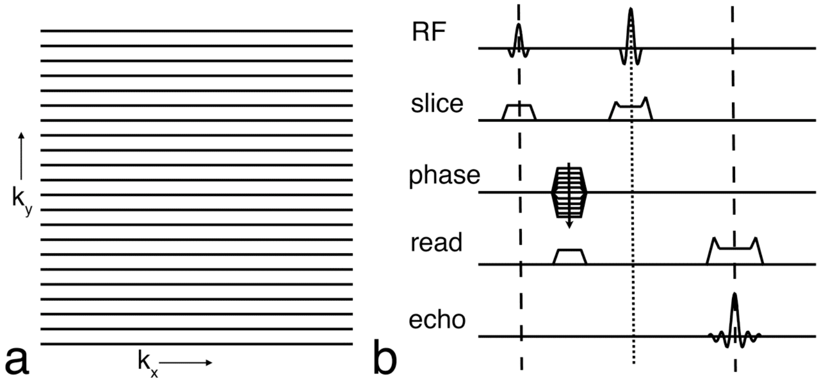

Figure 8: Cartesian multislice spin echo sequence. (a) k-space trajectory and (b) pulse sequence diagram as implemented on GE EPIC Lx12M4.

Projection Acquisition

The next important requirement from the imaging sequence for this work was immunity to motion. This was especially important after taking into account the earlier decision to use free-breathing mice. This need was met by the next step in sequence development – non-Cartesian data acquisitions.

Figure 9a shows the k-space trajectory for the Projection acquisition sequence. Unlike the Cartesian sequences where the data is acquired along a rectilinear grid (Fig. 8a), the data sampling in a Projection acquisition is akin to the spokes of a wheel. The sampling density in the center of k-space is significantly higher in the latter acquisition scheme. This has the following advantages:

- The central region of k-space contributes the most to the overall image appearance. The oversampling of this region in Projection acquisition causes averaging of data inconsistencies in the acquired views. This provides greater immunity to artifacts arising due to such errors.

- Undersampling artifacts in Projection acquisition are typically less objectionable than those in Cartesian acquisitions – lower intensity peripheral streaks as opposed to replication. Thus fewer views than the Nyquist-mandated limit are acceptable.
- Periodic motion, like respiratory or cardiac motion, during data acquisition causes periodic ghosts in Cartesian images. The number of ghosts and the distance between them is dependent on the period of the motion relative to TR. These ghosts tend to lie within the region of interest, thus making the image incomprehensible. On the other, periodic motion in Projection acquisition causes radial streaking. The streaks closest to the object have very low intensity and significant steaks occur farther away from it. Thus the region of interest is minimally affected due to this motion (Glover and Pauly, 1992).

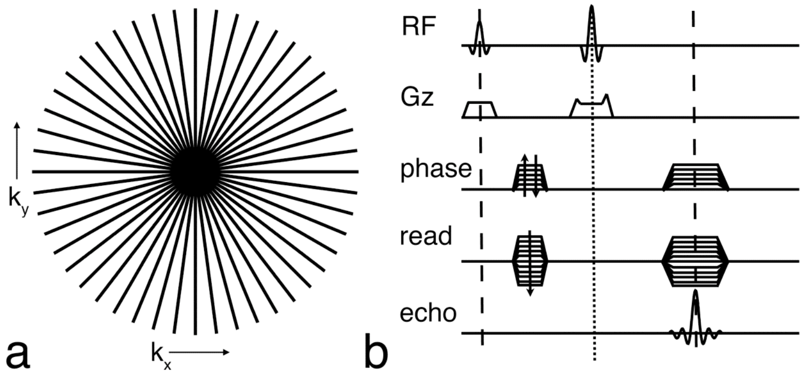

Figure 9: Multislice spin echo Projection acquisition. (a) k-space trajectory and (b) pulse sequence diagram as implemented on GE EPIC Lx12M4.

These advantages made Projection acquisition a very attractive scheme for imaging free-breathing animals. For the next step in sequence development a multi-slice spin echo sequence with Projection acquisition was implemented. The pulse sequence diagram for this scheme is depicted in Figure 9b.

It is important to note that Projection acquisition is not without limitations. The first is the effect of B_0 inhomogeneity and gradient inaccuracies on radially acquired data. These inconsistencies on Cartesian datasets manifest themselves as shifts in just the readout direction and can be readily corrected. In the case of Projection acquisition, they create a radial smear. Imperfect gradients result in timing errors during data acquisition and the echo centers no longer line up in the center of k-space, causing artifacts in the images. Gradient correction during data acquisition as well as post-processing during data reconstruction (Ahn and Cho, 1987; Peters et al., 2003) was employed to correct for these errors.

The second is longer imaging time. Data acquisition time of a Projection SE sequence is $\pi/2$ times longer than that of a Cartesian SE sequence with similar resolution. A larger number of projections need to be acquired in order to ensure adequate sampling (to meet the Nyquist sampling criterion) in the outer regions of k-space. The solution for this led to the next step in the progression of pulse sequence development.

Multi-echo Acquisition

In a spin echo sequence, an RF excitation pulse tips the magnetization into the transverse plane, which is then refocused by a second RF pulse to form a spin echo. This transverse magnetization can be repeatedly refocused to acquire multiple spin echoes by playing out additional refocusing pulses. Such a multi-echo sequence generates a train of echoes refocused at times TE_1, TE_2, TE_3, etc where typically

$$TE_2 = 2 \times TE_1, TE_3 = 3 \times TE_1, \ldots \tag{4.2}$$

The multi-echo sequence can be used in two ways:

- Each echo from an echo train is used to fill its own independent k-space and then a series of images with varying TEs is reconstructed. Such a technique is used to calculate T_2 maps.
- Each echo from an echo train is spatially encoded distinctively and used to fill a separate line in a single k-space. This gives a single image with an effective TE that equals the TE of the echo that samples the central k-space line.

This work focuses on the latter, also referred to as Fast Spin Echo (FSE) or Rapid Acquisition with Relaxation Enhancement (RARE) (Hennig et al., 1986). Such a multi-echo implementation has the following two advantages that make it particularly appealing for this application;

1. Reduction in imaging time

   In a multi-echo sequence, the number of lines of k-space acquired per excitation is equal to the echo train length. Thus, with an echo train length of L, the number of excitation and thus the imaging time needed to acquire an image is $\left(1/L\right)^{th}$ of that required for a spin echo sequence. Thus a multi-slice, multi-echo sequence is an extremely efficient sequence given the long TR that is necessary for high-field, in vivo imaging.

2. Increased signal for corresponding T_2 weighting

   T_2-weighted images for tumor visualization typically require long TE to enhance the distinction between and within tumor tissues. It is important to note here that even if two images are acquired at the same TE, their appearance can differ depending on the number of preceding refocusing pulses. Signal loss due to molecular diffusion, field inhomogeneity and J coupling is reduced as the spacing between the refocusing pulses is decreased (Carr and Purcell, 1954). Thus a spin echo image with a long TE (that has only one refocusing pulse) has much lower signal levels than a multi-echo image with a similar effective TE (multiple refocusing pulse with smaller duration between refocusing pulses to minimize signal decay) (Low et al., 1993).

The other advantages are lower sensitivity to off-resonance effects, such as B_0-field inhomogeneity, and reduced signal loss due to magnetic susceptibility effects. The disadvantages include higher RF power deposition (though this is of less consequence in the small animal application), blurring and edge enhancement (degree of which depends on the particular k-space trajectory), and increased lipid signal intensity (fat suppression using a chemically selective pulse is a possible solution).

There are significant challenges in implementing a multi-echo sequence. As the number of refocusing pulses in a sequence increases, the number of echoes generated increases. The imperfections in the RF pulses cause these echoes to have differing phases as well as temporal locations. In order to obtain a good reconstructed image from a multi-echo sequence it is important to design the sequence such that these echoes occur at the desired position and with the correct phase. Following is a brief discussion on coherence pathways in a sequence with multiple RF pulses and the Carr-Purcell-Meiboom-Gill (CPMG) (Carr and Purcell, 1954; Meiboom and Gill, 1958) condition that ensures proper alignment of echoes in a multi-echo sequence.

Coherence Pathways and the CPMG Condition

An RF excitation pulse tips the magnetization into the transverse plane. An RF refocusing pulse refocuses this magnetization. In the case of an imperfect refocusing pulse, in addition to refocusing the magnetization in the transverse plane, it also tips some of the magnetization in to the longitudinal plane and leaves some of the transverse magnetization unchanged. The effect on the longitudinal magnetization is similar; with some left intact, some inverted, and some tipped into the transverse plane. Subsequent refocusing pulses further divide the magnetization. Within the interval between the refocusing pulses, the transverse components of the magnetization continue to accumulate phase, while the longitudinal components stay intact. These phase evolutions of the magnetization components as seen in a phase diagram are called the coherence pathways. Figure 10 shows the coherence pathways for a train of RF pulses.

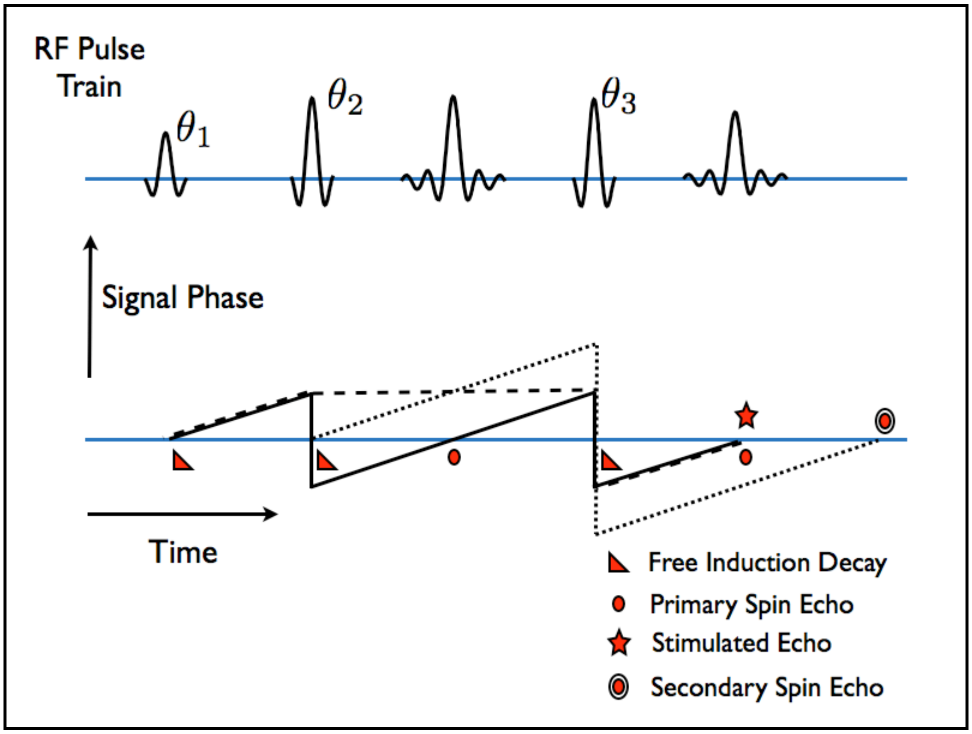

Figure 10: Coherence pathways for a sequence with multiple RF pulses (from 'Handbook of MRI Pulse Sequences').

Coherence pathways that experience phase reversal at every refocusing pulse form primary spin echoes. An imperfect refocusing pulse produces a free induction decay (FID). Phase reversal of the FID by subsequent refocusing pulses forms secondary spin echoes. A stimulated echo is formed when a coherence pathway, which is initially in the transverse plane is returned to the longitudinal plane by an imperfect refocusing pulse and then reexcited into the transverse plane by another imperfect refocusing pulse. The number of echoes increases exponentially as the number of refocusing pulses increases. These echoes, that are produced by various coherence pathways do no match in phase and temporal resolution, and when acquired within the same acquisition window cause signal cancellation and thus poor SNR. To ensure that such a condition does not occur, a multi-echo sequence needs to satisfy the CPMG conditions:

- Condition I
    1. Refocusing pulses must be 90° out of phase with respect to the excitation pulse.
    2. The refocusing pulses must be evenly positioned in the sequence with equal spacing between two consecutive refocusing pulses.
    3. Spacing between two refocusing pulses must be twice the spacing between the excitation pulse and the first refocusing pulse.
- Condition II

    The phase accumulated by a spin isochromat between any two consecutive refocusing pulses must be equal.

$$\gamma \int_{t_1}^{t_2} B(t)dt = \gamma \int_{t_2}^{t_3} B(t)dt = \ldots = \gamma \int_{t_{N-1}}^{t_N} B(t)dt \tag{4.3}$$

    t_i is the time at which the i^{th} refocusing pulse is played out in the sequence.

These design guidelines, in addition to the earlier decisions of using a multi-slice non-Cartesian sequence, formed the basis of the final sequence that was implemented and subsequently used for all the imaging studies.

A multi-echo sequence supports almost all k-space sampling strategies, including non-cartesian trajectories like projection (Hall and Sukumar, 1984), spiral (Block et al., 1997), PROPELLER (Pipe, 1999), etc. The PROPELLER sequence was chosen due to the numerous advantages that its novel sampling trajectory and enhanced reconstruction offer.

Chapter 5 describes the PROPELLER implementation for T_2-weighted imaging, and Chapter 6 extends the discussion to diffusion-weighted imaging.

5. T_2-weighted PROPELLER

Continued efforts to improve image quality in the clinical arena have led to the development of novel imaging sequences that provide higher signal, better contrast, and increased immunity to motion. This work builds upon that by J.G Pipe in the development of Periodically Rotated Overlapping ParallEL Lines with Enhanced Reconstruction (PROPELLER) (Pipe, 1999). A unique method of data collection and reconstruction makes this sequence inherently motion-insensitive and permits for the correction and prioritized weighting of data corrupted by certain kinds of motion. When implemented as a fast spin echo (FSE) sequence, PROPELLER can be used to obtain excellent T_2-weighted contrast.

5.1 Basic PROPELLER

The PROPELLER sequence was implemented as a modification of the standard FSE sequence on the EPIC Lx12.4 software platform. Figure 11a shows the k-space trajectory for PROPELLER and the pulse sequence diagram for the horizontal blade acquisition is shown in Fig. 11b. A slice-selective 90° RF pulse is used for excitation, which is then followed by a train of 180° RF refocusing pulses. The refocusing pulses are also slice-selective and are flanked on either side by "crusher" gradients to suppress the FID arising due to imperfections in the refocusing pulses. Gradients are also applied on either side of the readout gradients for the same purpose. Phase-encoding gradients are applied after the refocusing pulse and rewound after the readout gradients. This step is essential for maintaining phase coherence of the echoes, i.e., the Carr-Purcell-Meiboom-Gill (CPMG) condition (Carr and Purcell, 1954; Meiboom and Gill, 1958). Phase-encoding gradients are applied concurrently with the crusher gradients on the readout axis to minimize the inter-echo spacing (to reduce susceptibility-induced losses at high-fields). Subsequent blades are acquired by rotating the readout and phase gradients about the slice-select axis. Together, the blades sample the whole of the k-space, while each blade samples the circular region in the center of k-space.

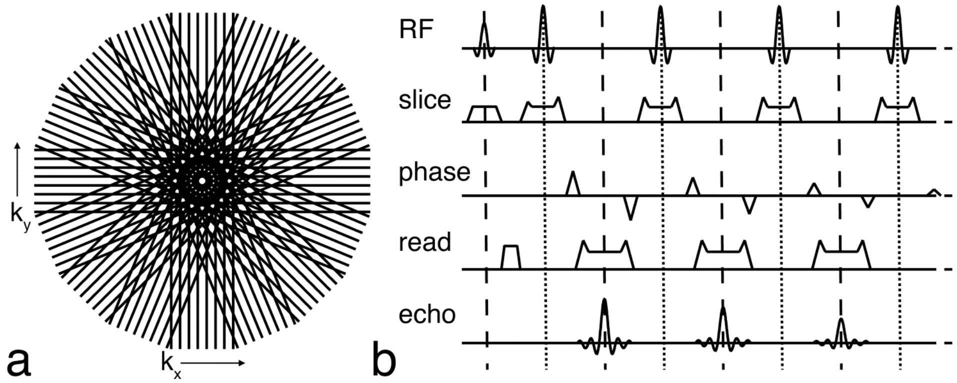

Figure 11: k-space trajectory (a) traversed by PROPELLER and the pulse sequence diagram (b) for the same as implemented on GE EPIC Lx12M4.

The oversampling of the central region of k-space (Fig. 11a) gives PROPELLER all the benefits that are characteristic of the Projection sequence; insensitivity to artifacts from motion, undersampling, and data inconsistencies between views. At the same time, due to the Cartesian nature of each blade, which is acquired in a single echo train, the data acquisition time is shorter. Furthermore, PROPELLER is unique in its ability to correct for motion. Each blade acquired in PROPELLER is in fact a low-resolution representation of the whole dataset (with full sampling along the direction of the blade, but undersampled in the orthogonal direction). This provides inherent navigational information to a dataset acquired with PROPELLER. This information is used to correct for in-plane bulk translational and rotational motion that might have occurred during data collection. Through-plane motion correction is achieved by discarding blades that have been severely affected by motion (the image quality is still maintained as the oversampling of the central k-space reduces the sensitivity to undersampling artifacts).

The pulse sequence diagram for the PROPELLER sequence in Fig. 11b shows the pulses played out during a single echo train (the horizontal blade). Subsequent echo trains are acquired after rotation of the read (x) and phase-encoding (y) gradients about the slice (z) axis. The angle of rotation is given by

$$\theta = \frac{\pi}{N} \tag{5.1}$$

$$N = \frac{M}{L} \times \frac{\pi}{2} \tag{5.2}$$

N is the total number of blades, M is the desired image matrix size and L is the number of echoes in the echo train (this is typically the same as the number of lines in the blade).

On a high field system, there are limitations on the length of the echo train (ETL) that can be prescribed due to faster T_2 decay and susceptibility related artifacts. The high-performance gradient coils make it possible to have very short echo spacing, thus alleviating some of the signal loss, but for longer echo trains, the later echoes make minimal contribution to the image.

The second factor that needs to be taken into account while deciding the ETL is the desired echo time, and thus the amount of T_2-weighting. The effective TE of the acquired image is defined as the time at which the echo passing through the center of k-space is acquired. Typically, the middle echo in the echo train samples the central k-space line. Thus a longer echo train has a longer TE, while a shorter ETL corresponds to a shorter TE. Longer TEs are necessary for higher T_2-weighting, which translates as increased contrast in tumor imaging.

The third factor is the relationship between the ETL and the width of the blade in the PROPELLER trajectory. Wider blades enable better motion correction. Traditionally, in clinical applications of PROPELLER, a single echo train is used to acquire one whole blade.

The above limitations led to the development of the modified 2-shot PROPELLER that is discussed in the next section.

5.2 2-shot PROPELLER

In conventional PROPELLER, a single echo train (one acquisition) is used to acquire one complete blade, as shown in Fig. 12a, where decreasing echo amplitude signifies echoes sampled later in the echo train. T_2 decay during the echo train limits the length of the echo train that can be prescribed, which in turn, affects TE, and hence the T_2-weighting of the image; and blade width, and hence the motion correction ability of the sequence. To overcome this, the modified PROPELLER uses two echo trains (two acquisitions or shots) to acquire a single blade. Three different blade acquisition orders are employed to increase the flexibility in echo times. In the early echo scheme (Fig. 12b), the first echo in the echo trains is used to sample the lowest phase-encoding line (the center of k-space). The effective TE in this case is small, equal to the inter-echo time, and the images have minimal T_2-weighting. The intermediate echo scheme (Fig. 12c) and the late echo scheme (Fig. 12d) have the central and the last echo in the echo train sampling the center of k-space respectively. These are the two schemes used predominantly for T_2-weighted imaging.

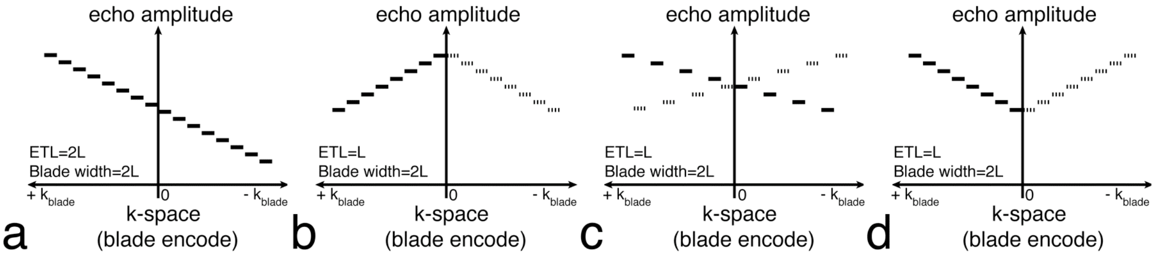

Figure 12: Echo number to blade position correspondence in (a) conventional PROPELLER and (b-d) 2-shot PROPELLER with (b) early, (c) intermediate, and (d) late acquisition order. The echo number increases as the echo amplitude decreases. For 2-shot PROPELLER (b-d), the bold and the dotted lines represent the two echo trains that make up a single blade. Effective echo time is defined as the time at which the echo at the k-space center is acquired.

In 2-shot PROPELLER, two echo trains are used for k-space filling of one blade. Thus, for an echo train length of L, the blade width is 2L. The total number of blades required to cover the complete k-space (i.e., to ensure that the data is Nyquist sampled) is

$$N = \frac{\pi}{2} \times \frac{M}{2L} \tag{5.3}$$

M is the desired image matrix size. The incremental angle between two successive blades in k-space is then given by

$$\theta = \frac{\pi}{N} \tag{5.4}$$

MATLAB (The Mathworks Inc., Natick, MA) was used for image reconstruction. Figure 13 outlines the steps followed during reconstruction, which is essentially the standard PROPELLER reconstruction flow (Pipe, 1999), but with two modifications. First, for 2-shot PROPELLER, the echo data are first reordered depending on the acquisition order (early/intermediate/late) used. This is done during the acquisition phase, so that the raw data has the blades in the correct sequence. Then image-space phase correction is carried out for each blade to align the point of rotation with the center of k-space. The second modification to the reconstruction flow is that only through-plane motion correction is employed. As the mice are anesthetized and securely positioned in the cradle throughout the course of the experiment, there is no in-plane rigid body translational and rotational motion. There are two types of motion encountered in the mouse from respiration— through-plane, and expansion (anterior to posterior). Since these two motions are strongly correlated, our method (that corrects for through-plane motion) effectively addresses both. This correction is carried out during reconstruction by prioritizing the data from each blade based on correlation with the averaged central data and minimizing the contribution of the blades that encounter through-plane motion. In the final reconstruction step, the corrected data are gridded onto a Cartesian array with density compensation applied to take into account the non-uniform sampling. The final image is obtained as the magnitude of the inverse Fourier transform of this data.

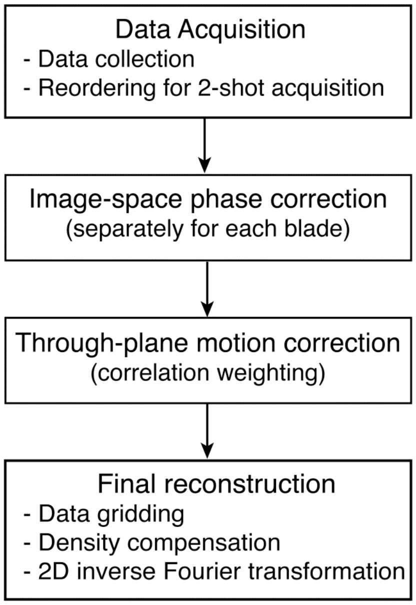

Figure 13: Reconstruction flow for 2-shot PROPELLER for high-field small animal imaging.

Results

The comparison of the conventional single-shot and the 2-shot PROPELLER sequences with the Cartesian fast spin echo present a wide selection of parameters. Here, the comparisons have been constrained to those with similar acquisition parameters and spatial resolution. Table 5 provides a summary of the acquisition parameters that were maintained constant for all three protocols.

Table 5: Imaging parameters that we maintained constant for the comparison between Cartesian fast spin echo, conventional single-shot PROPELLER and 2-shot PROPELLER sequences.

Parameter	Value
Repetition time	3 s
Echo time	~70 ms
Bandwidth	125 kHz
Field of view	30 mm
Image matrix	256 x 256
Number of slices	13
Slice thickness	1 mm
Total imaging time	30 minutes

Figure 14a, 14b show two representative slices from a multi-slice Cartesian fast spin echo sequence in a free-breathing mouse. Figure 14c, 14d show the same slices in the same free-breathing mouse acquired with the single-shot PROPELLER sequence. And Fig. 14e, 14f show the same slices from a 2-shot PROPELLER sequence. The imaging time was set to 30 minutes, representing a reasonable time for high-throughput studies. The animals were anesthetized using inhaled isoflurane, but they were breathing on their own. The reduction in motion artifacts with PROPELLER is dramatic. The Cartesian data (Fig. 14a, 14b) is severely degraded by ghosting artifacts arising from respiratory motion. Both PROPELLER datasets at the same levels (Fig. 14c, 14d and 14e, 14f) are nearly artifact-free. An ETL of 20 was used for the single-shot PROPELLER and FSE, whereas the 2-shot PROPELLER used an ETL of 10 with the late echo-ordering scheme. The acquisition time was maintained constant by adjusting the number of signal averages (NEX). NEX for single-shot acquisition (Fig. 14c, 14d) is twice that of the 2-shot acquisition (Fig. 14e, 14f). Signal-to-noise ratio (SNR) was compared in the inner and outer medulla of the kidney for single-shot (Fig. 14d) and 2-shot (Fig. 14f) sequences. The SNR in the 2-shot PROPELLER image (Fig. 14f) is 20-40% higher in the inner and outer medulla (8.07 and 13.24, respectively) than the single-shot PROPELLER (5.64 and 10.82, respectively). The higher signal also causes the peripheral streaking artifacts, which arise due to signal variations within views, to be more evident in the 2-shot technique. This can be seen in Fig. 14e and 14f where the images have been windowed down to see the background. The use of two shots preserves the higher frequencies much more effectively. Note, for example, that smaller vessels within the liver can be seen with 2-shot PROPELLER (Fig. 14e) than with conventional single-shot PROPELLER (Fig. 14c). The edge definition within the layers of the kidney is superior in Fig. 14f.

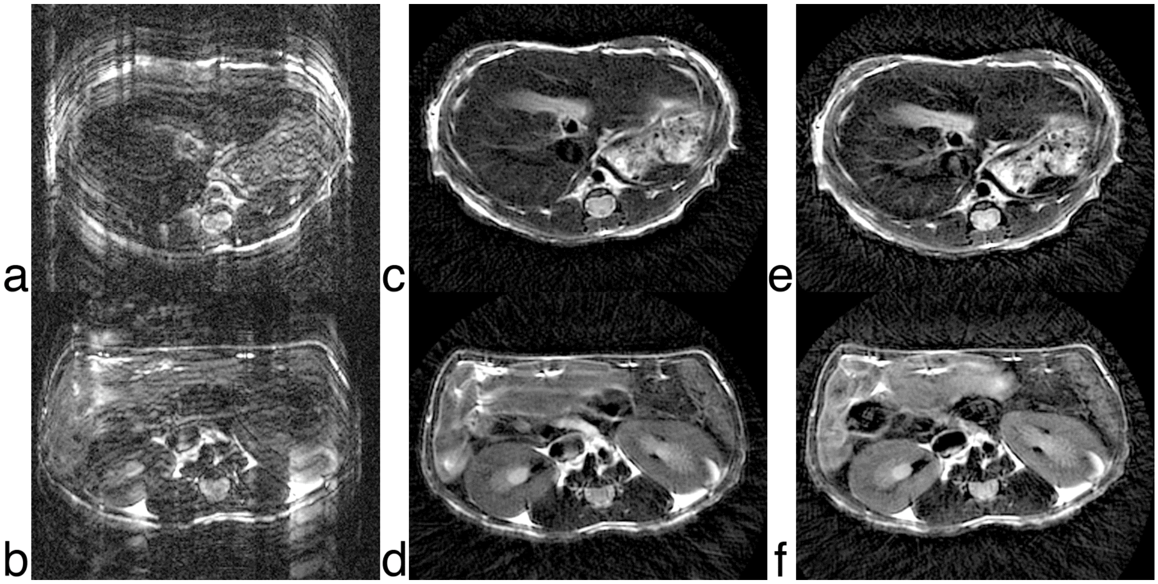

Figure 14: Comparison between standard Cartesian fast spin echo (a, b), conventional PROPELLER (c, d), and 2-shot PROPELLER (e, f). Multi-slice datasets with similar imaging parameters were acquired with all three sequences (117 μm in-plane, 1 mm slice thickness (13 slices), TR/TE = 3 s/ 70 ms, BW = 125 kHz, imaging time = 30 minutes). This figure shows two identical slices, one through the liver (a, c, e) and one through the kidneys (b, d, f).

T_2 contrast is governed by the effective echo time. Effective echo time is defined as the time at which the central line of k-space is acquired. In 2-shot PROPELLER, changing the length of the echo train, as well as varying the blade acquisition order, can vary the effective echo time. Figure 15 shows a series of images with increasing TE, obtained, in this case, by varying the echo train length. All three datasets were acquired using the 2-shot PROPELLER technique with the intermediate echo-ordering scheme. The imaging parameters are shown in Table 6. The number of blades in each case is adjusted depending on the ETL to ensure full Nyquist sampling of data at the periphery of k-space. To ensure sufficient SNR, the imaging time for all three datasets was fixed to about 45 minutes, which was maintained constant by increasing the number of excitations (NEX) for the longer echo train length scans.

Table 6: Imaging parameters for Figure 5 a-c.

Figure	ETL	Number of blades	Effective TE	TR	In-plane resolution	Slice thickness	NEX
5a	8	25	34ms	3s	117μm	1 mm	18
5b	12	16	48ms	3s	117μm	1 mm	28
5c	16	12	62ms	3s	117μm	1 mm	36

Figure 15 a-c show the same slice from multi-slice datasets acquired at different effective echo times. At a TE of 34ms (Fig 15a), the inner medulla (region 1) and outer medulla (region 2) are virtually indistinguishable, but at longer TEs, as the T_2-weighted contrast increases, the renal layers can be easily separated. The contrast evolution in the T_2-weighted images with increasing echo times is shown in Fig 15d.

$$CNR=\left(\frac{signal_1 - signal_2}{\sigma_{noise}}\right) \tag{5.5}$$

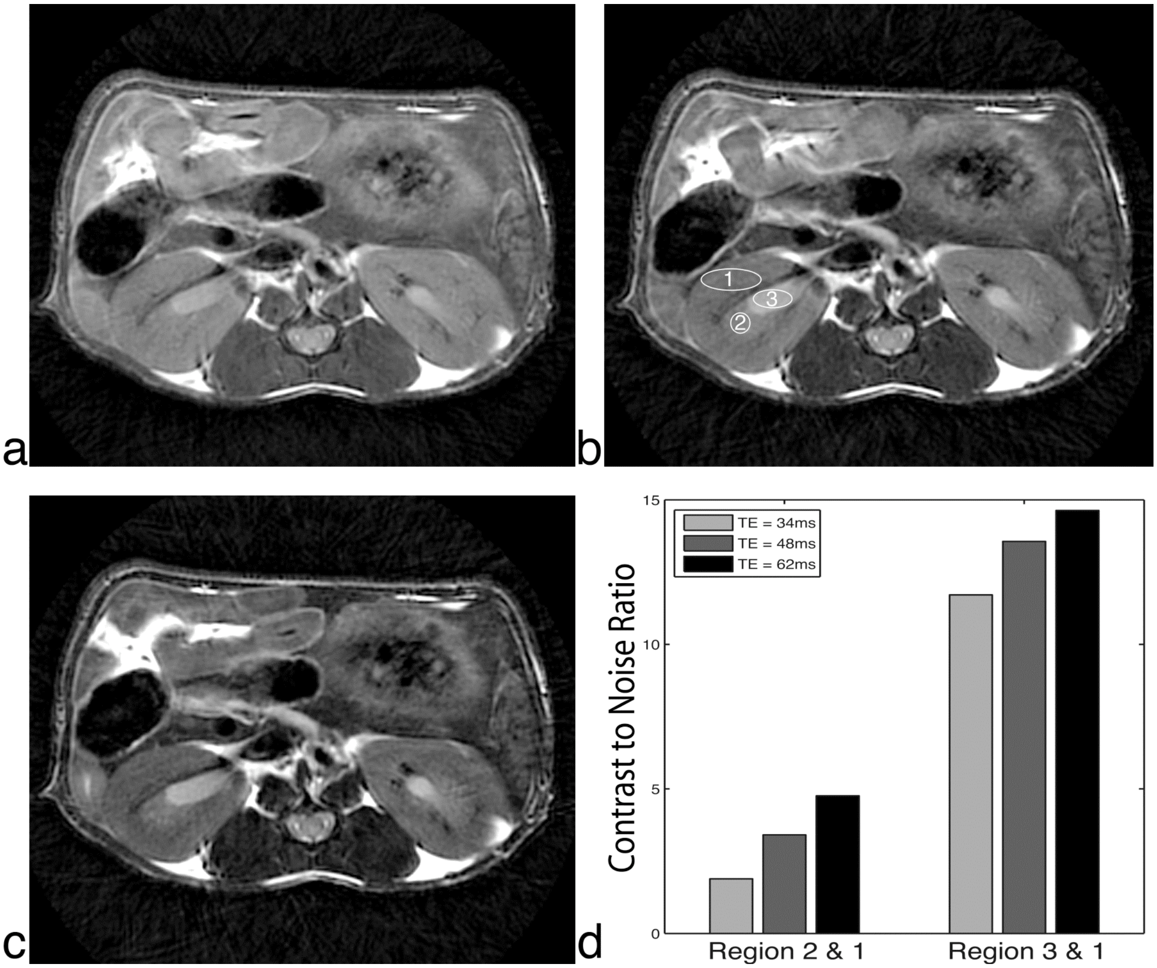

Figure 15: T2-weighted images of kidneys in a free-breathing mouse. 117 μm in-plane, 1 mm slice thickness (13 slices), TR = 3 s, BW = 125 KHz, imaging time ~ 45 minutes. Effective echo times were varied by changing the ETL of the scans (a) TE = 34 ms, ETL = 8, (b) TE = 48 ms, ETL = 12, (c) TE = 62 ms, ETL = 16, (d) CNR between theouter renal medulla (region 1) and the renal cortex (region 2) and the inner medulla (region 3).

Figure 16 shows the final set of images acquired in a free-breathing mouse with metastatic cancer in the liver. The liver is positioned immediately underneath the diaphragm, where the respiratory motion is greater than in any other part of the body. Nevertheless, the PROPELLER images are nearly artifact-free. The multi-slice datasets covered the entire abdominal region, from the lungs to the kidneys. All four datasets were acquired with the 2-shot PROPELLER sequence with the intermediate acquisition order. An identical representative slice, from all four datasets is shown in Fig. 16 a-d. As the echo time increases from Fig. 16a (27 ms) to Fig. 6d (69 ms), the T_2-weighting in the images increases. The relative contrast between the viable liver and the tumor tissue also increases accordingly, 43.2%, 55.9%, 63.2%, and 69.2%. The contrast is calculated as a percentage difference between the signal intensities between the tumor tissue and the viable liver, relative to the viable liver.

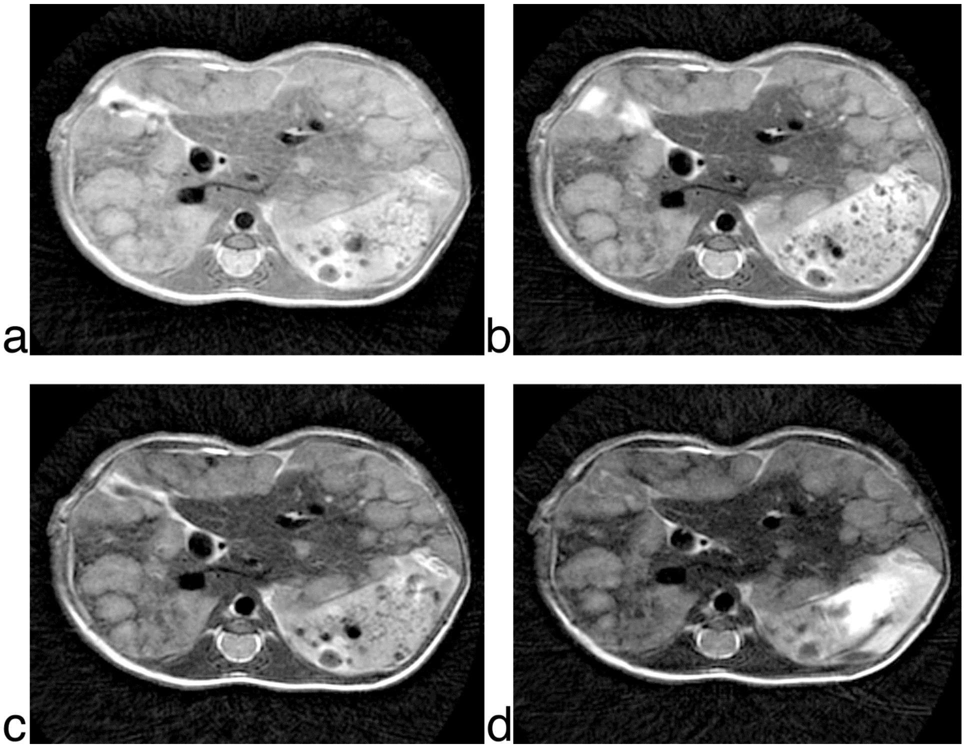

Figure 16: Liver tumor images from a free-breathing mouse acquired over a range of increasing echo times. 117 μm in-plane, 1 mm slice thickness (21 slices), TR = 2.5 s, BW = 125 KHz, ESP = 6.856 ms, imaging time ~ 40 minutes. (a) TE = 27ms, ETL = 6, (b) TE = 41ms, ETL = 10, (c) TE = 55ms, ETL = 14, (d) TE = 69ms, ETL = 18

Images at higher TEs show an additional definition in the tumor abnormal parenchyma. Note for example, Fig. 16d, where increased inhomogeneity can be seen within the tumor.

Discussion

The main advantage of this technique is in its robustness against motion. Both the conventional single-shot and 2-shot PROPELLER sequences effectively eliminate respiratory artifacts that make Cartesian strategies virtually useless for free-breathing animals. Additionally, the artifacts due to uncorrected motion and undersampling are expressed benignly in the form of peripheral streaking in image space (Fig. 14). This is characteristic of all non-Cartesian data acquisition schemes that oversample the center of k-space (Glover and Pauly, 1992). Though unlike the commonly used projection acquisition schemes, which merely offer relative immunity to motion, the PROPELLER data acquisition scheme is more robust as it also allows for correction and/or rejection of data corrupted by motion. PROPELLER oversamples a bigger area at the center of k-space and obtains inherent navigator information that makes this possible.

The 2-shot scheme provides higher SNR than the conventional single-shot scheme. At high fields, T_2 decay is faster, and hence signal variation between views is larger. This causes increased artifacts, mainly seen in the periphery of image space. As the signal in the 2-shot scheme is higher, artifacts also appear brighter (Fig. 14e, 14f). The 2-shot blade data can be acquired using one of three acquisition orders defined earlier, thus permitting three different effective echo times for a particular blade width. The early echo scheme provides T_1-weighted or proton density-weighted images, while the intermediate and late echo schemes are used for acquiring T_2-weighted images. Unlike the conventional PROPELLER sequence, where the central echo in the echo train typically defines the effective TE, this technique allows flexibility in choosing imaging parameters that provide the most significant information for the desired application in the region of interest. Note for example, the liver tumor images, where greater heterogeneity can be seen within the tumor in Fig. 16d, but Fig. 16c has higher CNR (15.08 in Fig. 16c compared to 9.49 in Fig. 16d). In this case, changing the ETL varied effective TE, but changing the acquisition order in the blades will do the same.

The early and late acquisition schemes are essentially segmented approaches, while intermediate acquisition is interleaved. These acquisition schemes may have different responses to motion. But these effects are probably second order, since the correlation function for motion correction is derived from the whole blade. Moreover, the motion for this specialized application is relatively restricted. Finally, the majority of the improvements come from the inherent averaging at the center of k-space.

To ensure adequate signal in the high-resolution datasets, signal averaging was carried out during all imaging experiments. For a fair comparison between images, the imaging time for all datasets in an experiment was kept constant. For a fixed imaging duration, datasets acquired with shorter ETL had fewer signal averages. Thus, for the same blade width, the number of signal averages for the 2-shot scheme was half of that for the single-shot scheme. But, since later echoes in a short echo train make a more substantial contribution to the overall signal than the later echoes in a long echo train, the 2-shot technique retains more high-frequency information and the overall SNR is also higher (as can be seen from Fig. 14).

One inherent problem with FSE imaging is the discontinuities in the acquired data arising from T_2 decay (Mulkern et al., 1991; Mulkern et al., 1990). These occur when there is substantial delay (and hence T_2 decay) between the first and the last line of k-space acquired in a single excitation. T_2 decay is more rapid at high-field strengths due to higher susceptibility-induced losses (Malisch et al., 1991). Thus, the signal discontinuity between consecutive echoes is more prominent. Correction of artifacts associated with this problem is thus more important at high-fields (Zhou et al., 1993).

In Cartesian FSE, T_2 signal discontinuities cause blurring and ghosting in the image. This is seen along the phase-encoding direction. The complicated data acquisition strategy in PROPELLER makes interpreting these artifacts more difficult, particularly when considered in conjunction with other sources of artifacts, such as motion, phase errors due to eddy currents, gradient imperfections, etc. The higher signal levels in 2-shot PROPELLER cause a concomitant increase in the artifact levels associated with signal discontinuity (Fig. 14). The need to reduce these artifacts led to the final step in the PROPELLER sequence modification for this high-field murine imaging application.

5.3 High-field correction

PROPELLER data acquisition uses a Carr-Purcell-Meiboom-Gill (CPMG) echo train where each phase-encode line is acquired by a different echo. Thus, each phase-encode line has its own echo time, which is a multiple of the echo spacing. This results in a k-space with discontinuous T_2-weighting along the width of the blade, i.e. the phase-encode direction. The decay along the readout direction can be ignored, particularly if the receiver bandwidth is high. We refer to this T_2-weighting function along the phase-encode direction as $W(k_y)$.

$$W\left(k_y\right) = e^{-n\left(k_y\right)\times ESP/T_2} \tag{5.6}$$

Here, n is the echo index. The acquired data are then given by

$$S\left(k_x, k_y\right) = S_0\left(k_x, k_y\right) \bullet W\left(k_y\right) \tag{5.7}$$

The reconstructed image is

$$I(x,y) = I_0(x,y) * w(y) \tag{5.8}$$

I_0 is the ideal image reconstructed from S_0, which does not experience any discontinuous T_2-weighting.

Contrast in an image is predominantly determined by the low-frequency data. To obtain higher T_2-weighted contrast, early echoes in the echo train are used to sample the outer lines in the blade, while the later echoes are used for the center of the blade. This results in a T_2-weighting function, as shown in Fig. 17c.

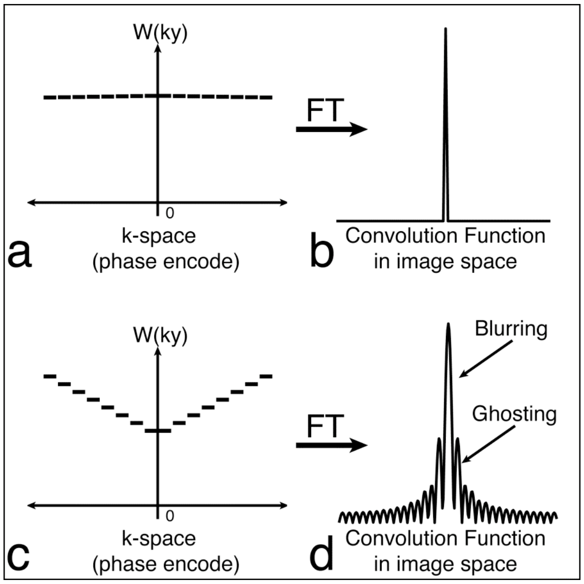

Figure 17: T2-weighting function along the phase-encode direction for (a) conventional spin echo sequence, and (c) multi-echo spin echo sequence. (b) and (d) are the Fourier transforms of (a) and (c) respectively.

In conventional spin echo images, $W(k_y)$ is constant (Fig. 17a) and its Fourier transform (FT) is a delta function (Fig. 17b). So, the reconstructed image in this case is the ideal image. For the weighting function shown in Fig. 17c, the acquired image is a convolution of the ideal image with the FT of $W(k_y)$. From Fig. 17d, note that such a weighting will give rise to blurring (widening of main peak) and ghosting (side lobes) in each blade and hence considerable artifacts in the complete reconstructed image.

These artifacts are alleviated with the following simple correction technique. From Eq. [5.7] and [5.8], deconvolution in the image space or alternatively, division in the k-space (by $W(k_y)$) will effectively reduce the discontinuous nature of the acquired data. This would ideally require a complete T_2 map of the data, but a simpler (faster), though less accurate method, is to use an average/global T_2 value.

$W(k_y)$ is derived from an additional acquisition of a reference blade. This blade is acquired in the same way as the actual data blade (2-shot in this case), but without phase-encoding gradients. So, each line in the reference blade samples the same $k_y = 0$ line in k-space, but at a different echo time. The signal decay seen along the reference blade is thus representative of the T_2 decay in the specimen. The scaling factor $W(k_y)$ is an array of scalars that is extracted from the magnitude of the complex-valued data for each line in the blade, and is normalized with the magnitude of the first acquired line in that blade—the first echo in the echo train. Each data blade is then divided by this scaling factor $[W(k_y)^{-1}]$ to generate a corrected k-space with uniform weighting in the phase direction. The corrected blade now looks more like Fig. 17a instead of Fig. 17c. This correction is carried out for each blade in all the slices.

The data acquisition follows the 2- shot PROPELLER trajectory discussed previously (Pandit et al., 2008). The sequence was modified to include two additional excitations for one reference blade data collection. The reference blade acquisition is identical to the actual data acquisition, but with the phase-encoding turned off. The total number of blades acquired is now

$$N = \frac{\pi}{2} \times \frac{M}{2L} + 1 \tag{5.9}$$

where M is the desired image matrix size. The incremental angle between two successive blades is function of the number of data blades and is thus given by

$$\theta = \frac{\pi}{N - 1} \tag{5.10}$$

Image reconstruction is carried out in MATLAB (The Mathworks Inc., Natick, MA), and follows the same procedure described previously, but with the additional module for T_2 signal discontinuity correction. The correction factor is generated from the reference blade data that are collected for each slice. This correction factor is then used to scale the actual data for that slice. Figure 18 outlines the data acquisition and reconstruction process.

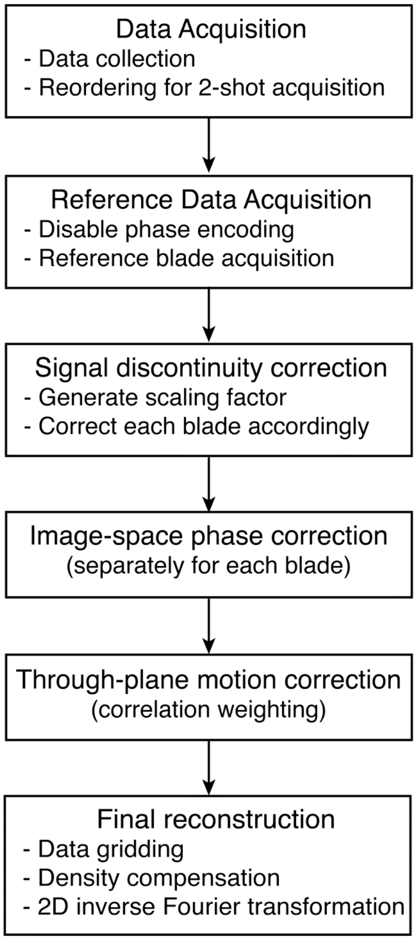

Figure 18: Data acquisition and reconstruction flow for 2-shot PROPELLER with correction for discontinuous T2-weighting.

The performance of this technique was first evaluated in computer simulations and phantom data. The phantom used in this experiment was a 30mm diameter bottle of water doped with copper sulphate (5mM concentration) with a homogeneous T_2 of 125 ms chosen to highlight the artifacts. The artifacts and the effects of the correction algorithm were studied for the imaging parameters listed in Table 7. All data were acquired using the 2-shot PROPELLER technique in which the early echoes are at the outer edges of the blade and the later echoes are at the center.

Table 7: Image parameters for simulation and phantom studies.

ETL	Blade Width	Number of data blades	Effective TE	TR / BW	Resolution In-plane/Slice
8	16	25	57 ms	4s / 125 kHz	195 μm/2 mm
12	24	16	86 ms	4s / 125 kHz	195 μm/2 mm
16	32	12	114 ms	4s / 125 kHz	195 μm/2 mm

Computer simulations were performed on a two-dimensional uniform phantom, similar to the one used in the phantom experiments. PROPELLER raw data were generated by periodic rotations of the Fourier transform of the phantom. T_2 decay along the width of the blade was modeled by scaling the rotated data as shown in Fig. 17c. T_2^* decay along the readout direction was ignored. Computer simulations were carried out to correspond with the imaging parameters chosen in the phantom experiments.

Results

Figure 19 shows the results of the computer simulations, as well as the phantom experiments for three different sets of acquisitions with varying echo train lengths (ETL) as described in Table 7. Column 1 in Fig. 19 shows the results from the computer simulation, and column 3 shows the results from the phantom experiment on the 7T magnet. Signal discontinuities due to T_2 decay along the phase-encode direction cause rings to appear in the reconstructed image of the uniform circular phantom. As the echo train length increases, the time between the first and last echo acquisition increases and thus the magnitude of the signal discontinuities in the acquired data increases. Figure 19 shows that increasing ETL causes more, but narrower, rings to appear in the reconstructed image; 1 ring for ETL = 8 (Fig. 19a, 19c), 2 for ETL = 12 (Fig. 19e, 19g) and 3 for ETL = 16 (Fig. 19i, 19k). This corresponds with the changes in the FT of the T_2-weighting function, $W(k_y)$, shown in column 2 (Fig. 19b, 19f, 19j). As the ETL increases, the number of side lobes increases, while their width decreases.

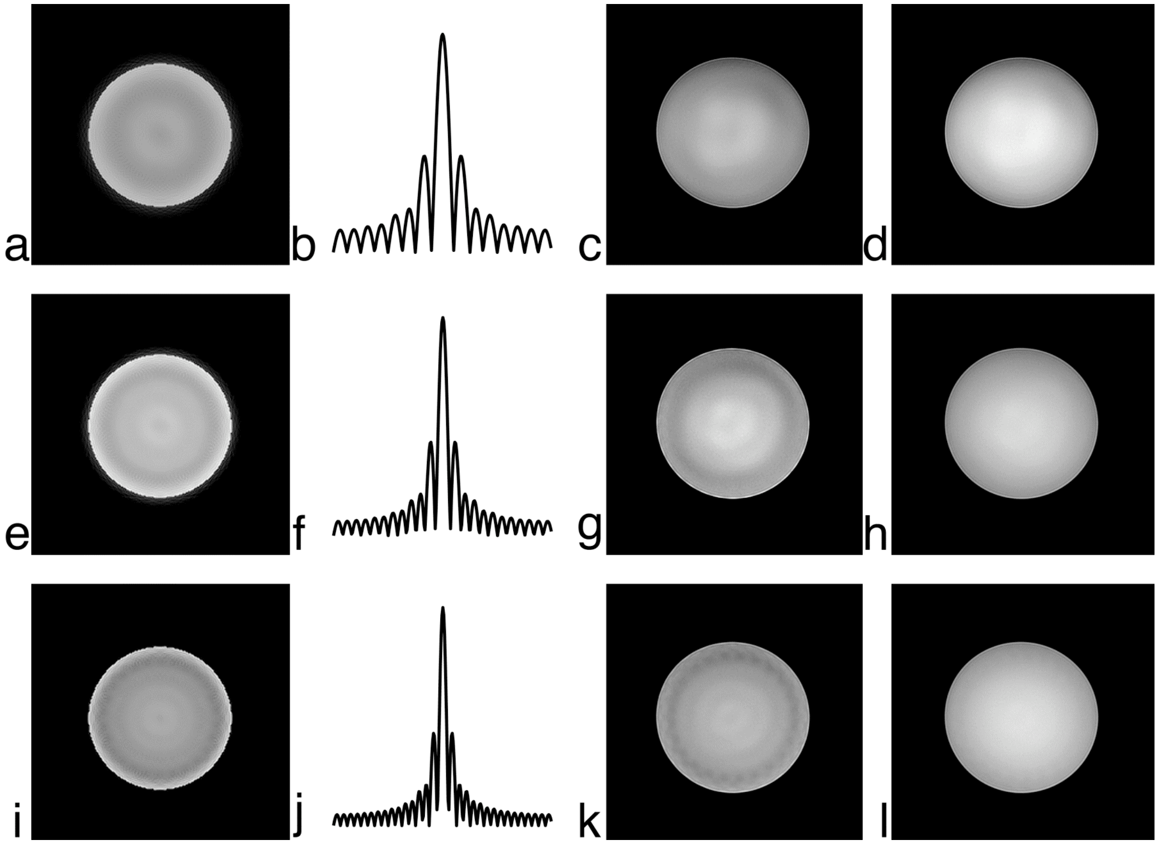

Figure 19: Computer simulation and phantom experiment results for three sets of images with varying ETL, (a-d) ETL = 8, (e-h) ETL = 12, and (i-l) ETL = 16. Computer simulation (column 1) and phantom results (column 3) for reconstruction without T_2 discontinuity correction are in good agreement. Column 2 shows the Fourier transform of the T_2-weighting function, i.e., the convolution function in the image space. Last column shows the phantom images reconstructed with the T_2 discontinuity correction.

The last column in Fig. 19 shows the reconstructed phantom image after correcting for T_2 discontinuities using the technique described in this paper. The corrected images have a more uniform signal profile, and the rings that were present in the uncorrected images can no longer be seen. Another improvement is the absence of the bright edge, caused by high-pass filtering from the T_2-weighting function, which is evident in the uncorrected images.

Figure 20 shows three representative slices from a multi-slice dataset acquired in a free-breathing mouse with multiple lesions in the lung. The first row (Fig. 20a, 20b, 20c) shows the dataset without the correction, while the second row (Fig. 20d, 20e, 20f) is the same dataset reconstructed with the correction algorithm. Table 8 lists the image acquisition protocol used for the in vivo studies.

Table 8: Acquisition protocol for lung tumor imaging in free-breathing mice.

Imaging sequence	2-shot PROPELLER with late echo ordering
Blade width	20
Number of blades	20
Echo time	78 ms
Repetition time	3 s
Bandwidth	125 kHz
In-plane resolution	117 µs
Slice thickness	1 mm
Number of slices	21
Number of excitations	20
Imaging time	42 minutes

The image reconstruction with the correction algorithm is clearly superior. Each slice in Fig. 20 shows improvement in a distinct feature of the image. Note the signal drop-off (arrows) in the muscles in Fig. 20a, which is absent in Fig. 20d. In Fig. 20e, the arrow points to a small lesion ($0.1mm^3$) in the lung. This lesion is not discernible in Fig. 20b. The third slice (Fig. 20c, 20f) shows the liver vasculature. The corrected image shows improvement in both the background liver tissue, as well as in the blood vessels. Smaller branches in the vasculature can be seen more clearly at the edge of the liver in Fig. 4f than in Fig. 20c.

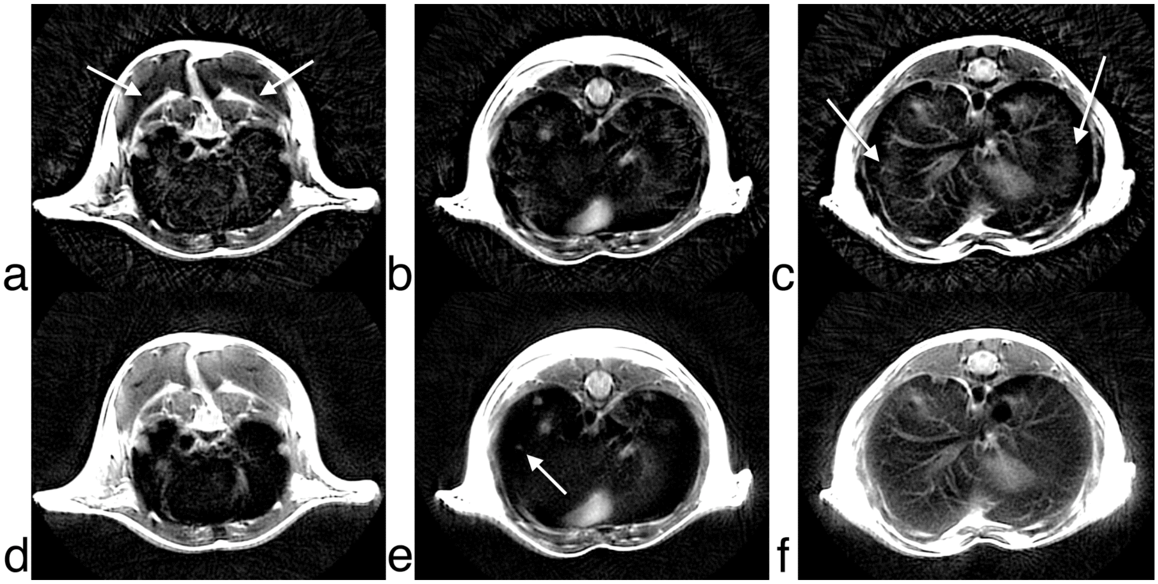

Figure 20: Comparison between images reconstructed without (a, b, c) and with (d, e, f) T2 discontinuity correction. Each column shows a different slice from a multi-slice dataset acquired in a free-breathing mouse. 117 µm in-plane, 1 mm slice thickness (21 slices), TR/TE = 3s/68ms, BW = 125 kHz, ETL = 10, imaging time ~ 40 minutes. Arrows point to specific aspects in the slice that show improvement due to the correction algorithm.

The results of the longitudinal experiment are shown in Fig. 21 with the uncorrected (shown on the left) and corrected (shown on the right) reconstruction. The image sequence shows the longitudinal growth of the small lesion shown in Fig. 20e (also Fig. 21b). Multi-slice datasets covering the thorax and abdomen were acquired with an interval of 12 days between consecutive time points. The lesion grows from 0.10mm^3 on day 1 (Fig. 21b) to 0.38mm^3 on day 12 (Fig. 21d) and 0.71mm^3 on day 23 (Fig. 21f). Artifacts in the uncorrected image make it difficult to detect the lesion in Fig. 21a. The lesion can be seen in Fig. 21c and 21e, though the ghosting and streaking make extraction of any quantitative information difficult.

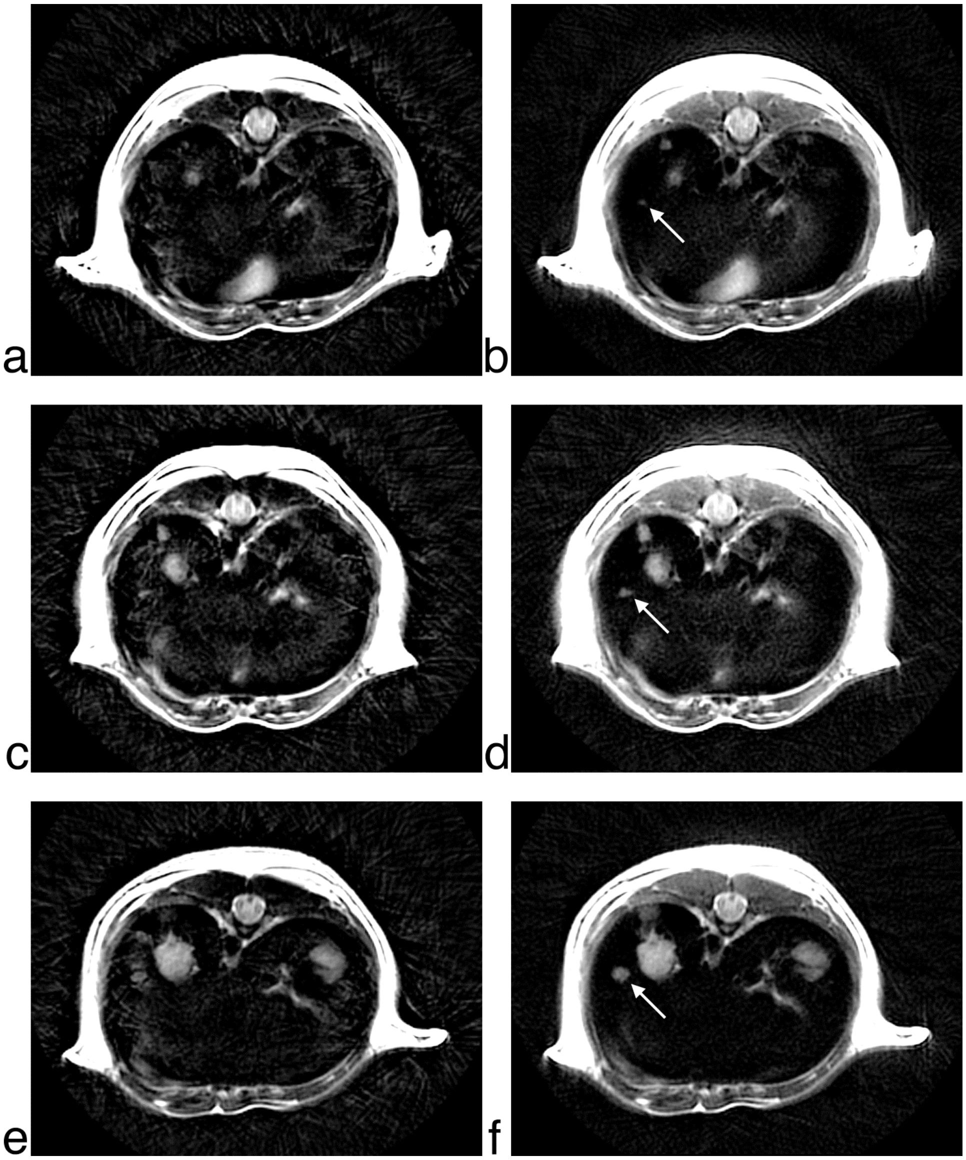

Figure 21: Lung tumor images from a free-breathing mouse acquired at three time-points following the tumor growth. Image reconstruction is carried out without (a, c, e) and with (b, d, f) T2 discontinuity correction. 117 µm in-plane, 1 mm slice thickness (21 slices), TR/TE = 3s/68ms, BW = 125 kHz, ETL = 10, imaging time ~ 40 minutes. (a, b) Day 1, (c, d) Day 12, and (e, f) Day 23. Arrows track the growth of the same lesion.

Discussion

T_2 signal decay along the length of the echo train causes discontinuous weighting of k-space data in FSE-based PROPELLER acquisitions. As shown in Fig. 17d, convolution with the weighting function results in blurring and ghosting in the reconstruction. In PROPELLER, the problem goes a step further. The weighing function causes blurring and ghosting in each blade, but the complete dataset is obtained by acquiring blades rotated around the center of k-space. Thus, this causes the ghosts to also be rotated, resulting in distinct rings in the image for an object with homogeneous T_2 (Fig. 19). As the ETL increases, the discontinuities within the blade get larger, $W(k_y)$ gets sharper, the width of the side lobes in the FT of $W(k_y)$ decreases, and their number increases (Fig. 19b, 19f, 19j). This increases the number of rings in the reconstructed image. Simulation results, as well as phantom data, demonstrate this phenomenon.

For objects with a broader spectrum of T_2 values, the artifacts are harder to interpret. Like all data inconsistencies in non-Cartesian datasets, these too manifest as streaks in the image. This is evident from the in vivo images (Fig. 20, 21). Measurement of the aggregate decay yields a first-order measure of the discontinuities, which can be used in the correction algorithm.

A lung tumor model was used to demonstrate the advantages of the 2-shot PROPELLER technique and the necessity for correction of the discontinuous T_2-weighting in multi-echo acquisitions at high-fields. The dark air spaces in the lungs make the artifacts (bright streaks) more pronounced, whereas in any other part of the body they would be harder to differentiate. For the same reason, removal of these artifacts is also more evident in the lungs.

The correction technique described here brings about a clear improvement in several areas of the image. Note, for example the signal drop-off in the muscles in Fig. 20a. Later echoes in the echo train sample the center of k-space (for heavier T_2-weighting), which brings about this loss in low-frequency information. The scaling in the correction technique helps retrieve this information, as is seen in Fig. 20d. Column 2 in Fig. 20 illustrates the improvement due to the reduction in the high-frequency noise (streaking artifacts) that interferes with the high-frequency information in the image (tiny lesion). In Fig. 20f, we can see improvement in both the low-frequency (liver parenchyma) and the high-frequency (peripheral vasculature) components of the image.

To ensure adequate signal in the high-resolution datasets, signal averaging was carried out during all in vivo imaging experiments. The imaging time was set to approximately 40 minutes, representing what we believe to be a reasonable tradeoff between image quality and throughput. The correction technique requires only one additional blade and hence, does not cause a significant increase in the total imaging time.

5.4 Conclusion

T_2-weighted imaging has proven to be a good mechanism for abdominal imaging due to the excellent soft-tissue contrast that can be obtained. Clinical studies focusing on the abdominal region rely on breath-hold imaging to mitigate the effects of respiratory motion (Choe et al., 1997; Keogan and Edelman, 2001). In small animal imaging, scan-synchronous ventilation is the method of choice. Intubation or tracheotomy of the animals (Mai et al., 2005) allows maximum control on the respiration, but this is highly invasive and time-consuming. The alternative is to track the respiratory motion in spontaneously breathing animals and synchronize the data acquisition with the respiratory cycle (Baboi et al., 2007; Cassidy et al., 2004; Garbow et al., 2008; Takahashi et al., 2007). The main drawback of this method is the dependence of repetition time on the respiratory period. This adversely affects the image contrast, as well as restricts the number of slices that can be acquired. The technique proposed here avoids these limitations by relying on the imaging sequence to detect and reject views acquired during respiration. It also gives excellent T_2-weighted images and provides the flexibility in choosing the most appropriate parameters to get the optimal contrast in different parts of the body.

The multi-slice, multi-echo approach makes efficient use of the longer TR that is necessary to minimize the effects of longer T_1 at high field. Also, at high magnetic field strength, the susceptibility-induced signal losses are high. Multi-echo techniques yield better T_2-weighted images compared to conventional single-echo spin-echo techniques (Low et al., 1993). The use of a train of 180° pulses refocuses the magnetization at shorter intervals and minimizes the T_2^* losses.

A negative consequence of multi-echo imaging at high-fields is the discontinuous T_2-weighting of the k-space data in the phase encode direction. The simple correction technique implemented in this work corrects for the ensuing image artifacts by acquiring an additional reference blade during data acquisition. This reference blade data are used to deconvolve the effect of signal discontinuities from the data blades.

Another important consideration for improved image quality is to have as short an inter-echo spacing (ESP) as possible (Vinitski et al., 1993). This was achieved by overlapping the phase-encoding gradients with the “crusher” gradients on the readout gradient. Additionally, as the extent of the blade in the phase direction is restricted to the central regions of k-space, the phase encoding gradients in PROPELLER have smaller amplitudes. This, in combination with the use of gradient amplifiers with rapid rise time (770 mT/m in 100 μs) allowed for a short ESP of 6.8 ms. Reducing the width of the slice-selective gradients can further shorten the echo spacing. More sophisticated RF refocusing pulses offer additional opportunities for fine-tuning of the sequence.

The current protocol is restricted to axial images. In PROPELLER, sagittal and coronal images cause streaking artifacts when the object volume extends beyond the field of view. Prescribing the field of view to cover the entire extent of the coil overcomes this, but at the expense of reduced image resolution. Alternatively, an asymmetric field of view can be acquired at the cost of higher pulse sequence complexity (Devaraj and Pipe, 2009). The second concern is lipid signal enhancement (Henkelman et al., 1992). This is seen in all RARE sequences, particularly when late echoes are used to sample the center of k-space. This effect increases with decreasing echo spacing. Lipid signal suppression using frequency-selective pulses is a possible remedy. The drawback in this case is reduced SNR due to water signal saturation or attenuation that is unavoidable in these techniques.

Though there is room for further enhancements in the sequence, the results show the tremendous improvement that the sequence provides. Importantly, it satisfies all the requirements that were put forth in the Software Section of Chapter 4 – immunity to motion, reduced imaging time, and high contrast resolution. Chapter 6 builds upon this sequence to obtain diffusion-weighted contrast.

6. Diffusion-weighted PROPELLER

Diffusion-weighted imaging relies on contrast originating from the differences in the motion of water molecules between different tissues. This technique provides qualitative and quantitative information on changes taking place at the cellular levels. As such, it is fast emerging as a technique for cancer imaging, with applications in tumor detection and characterization (Kim et al., 1999; Koh et al., 2006; Moteki and Sekine, 2004), as well as monitoring and predicting treatment response (Chen et al., 2007; McConville et al., 2007; Roth et al., 2004; Zhao et al., 1996).

This chapter describes the extension of the 2-shot PROPELLER technique to diffusion-weighted imaging. Thus all the advantages of the PROPELLER technique for high-field murine imaging are retained with the additional benefit of obtaining functional information.

6.1 Theory

Water molecules undergo constant random (Brownian) motion. When unrestricted, this is the free diffusion of water described by Einstein's diffusion equation.

$$x_{rms} = \sqrt{2Dt} \tag{6.1}$$

where x_{rms} is the root-mean-squared displacement in time t for a system with a diffusion coefficient D. But in biologic tissues, the presence of cell membranes, macromolecules, fibers, etc restricts the mobility of the water molecules. The degree of restriction is directly proportional to the cellular density.

In the presence of magnetic field gradients, this diffusion of water molecules causes a phase dispersion of the transverse magnetization, resulting in attenuation of the net signal. In typical imaging sequences, the signal decay due to diffusion is much smaller as compared to T_2 relaxation, and thus usually ignored. But special pulse sequences that can amplify the diffusion effect can be used for measuring it.

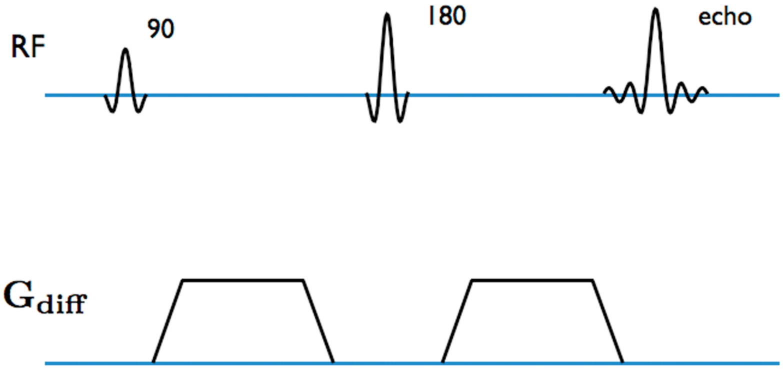

Figure 22: Concise representation of the commonly used diffusion-weighted imaging sequence with bipolar diffusion gradients

Most prevalent sequences that allow for in vivo detection and quantification of the water diffusion are based on a technique developed by Stejskal and Tanner (Stejskal and Tanner, 1965). Figure 22 shows a concise representation of the sequence. A symmetric pair of diffusion-sensitizing gradients (G_{diff}) is applied around the refocusing pulse to differentiate between static molecules and moving water molecules. The phase information acquired by the static molecules from the first diffusion gradient is rephased by the second diffusion gradient, leaving the signal intensity intact. By contrast, in moving molecules, the phase information from the first gradient is not completely rephased by the second gradient. This causes signal loss. Thus water diffusion is detected as signal attenuation.

Bloch (Bloch, 1946) originally described the rate of change of magnetic moment as being dependent on the precession caused by external magnetic fields, and the effect of T_1 and T_2 relaxation. Combining Eq. [2.2] and [2.4], the Bloch equations are given by,

$$\frac{dM}{dt} = \gamma M \times B - \frac{M_{xy}}{T_2} - \frac{M_z - M_0}{T_1} \tag{6.2}$$

Torrey (Torrey, 1956) added an addition term to the equation to include the effect of diffusion (D) on the magnetic moment.

$$\frac{dM}{dt} = \gamma M \times B - \frac{M_{xy}}{T_2} - \frac{M_z - M_0}{T_1} + \nabla \cdot D \nabla M \tag{6.3}$$

This is based on Fick's laws of diffusion, where, for a spin concentration C,

$$\frac{dC}{dt} = \nabla \cdot D \nabla C \tag{6.4}$$

So, updating Eq. [2.6] to take diffusion into account, the effective MR signal that is acquired is

$$S \propto \rho M_0 (1 - e^{-TR/T_1}) e^{-TE/T_2} e^{-bD} \tag{6.5}$$

or

$$S = S_0 e^{-bD} \tag{6.6}$$

where S_0 is the net signal in the absence of diffusion-sensitizing gradients, D is the apparent diffusion coefficient (ADC) – the quantitative metric that defines the diffusion in a biologic tissue and b is the parameter describing the sensitivity of the sequence to water diffusion. The b-value depends on the diffusion gradient amplitude, the duration of the applied gradient and the time interval between the gradients.

$$b = \gamma^2 \int_0^{TE} \left[\int_0^{t} G(t'')dt'' \right]^2 dt \tag{6.7}$$

Smaller b-values (~ 100 s/mm^2) are sufficient to cause measurable signal attenuation for water molecules with a large degree of motion, e.g. within the intravascular spaces. But for slow-moving water molecules, in the extra and intracellular spaces, much larger b-values are required (~ 1000 s/mm^2) (Koh and Collins, 2007).

For the cancer imaging application, it is important to be able to evaluate changes in the tumor microenvironment. Thus diffusion-weighted images need to reflect changes taking place at the cellular scale. The large b-values necessary to enable this are obtained by increasing the amplitude and duration of the diffusion-sensitizing gradients, as well as by increasing the time interval between them. This is an acceptable technique for diffusion-weighted imaging using gradient echo or spin echo acquisitions, but in the case of multi-echo acquisitions, it is harder to implement.

In a multi-echo acquisition, the application of bipolar diffusion gradients as described above causes the CPMG conditions to be violated. Referring to Chapter 4, Section 4, the CPMG conditions are:

- Condition I
    1. Refocusing pulses must be 90° out of phase with respect to the excitation pulse.
    2. The refocusing pulses must be evenly positioned in the sequence with equal spacing between two consecutive refocusing pulses.
    3. Spacing between two refocusing pulses must be twice the spacing between the excitation pulse and the first refocusing pulse.
- Condition II

    The phase accumulated by a spin isochromat between any two consecutive refocusing pulses must be equal.

$$\gamma\int_{t_1}^{t_2} B(t)dt = \gamma\int_{t_2}^{t_3} B(t)dt = \ldots = \gamma\int_{t_{N-1}}^{t_N} B(t)dt \tag{6.8}$$

t_i is the time at which the i^{th} refocusing pulse is played out in the sequence.

When the diffusion-sensitizing bipolar gradients are applied on either side of the first refocusing pulse, Condition II is no longer satisfied when there is motion. The spins are left with spatially varying and unknown phases at the end of the diffusion gradients and the sequence is now more susceptible to inhomogeneity in B_1. A number of schemes have been published that combat the violation of the CPMG condition for multi-echo acquisitions.

Some of the proposed techniques separate the components of the net magnetization that destructively interfere (Alsop, 1997; Mori and van Zijl, 1998; Norris et al., 1992) to enable stable echo magnitudes throughout the echo train. The drawback in this case, is the reduction of signal intensity by a factor of 2. Other techniques (Le Roux, 2002; Pipe et al., 2002) use the quadratic phase modulation of the refocusing pulses to produce a sustained echo train. The data acquisition in this case is quite complicated and significant post-processing is required before image reconstruction. Additionally, all these techniques have been implemented at lower field strengths (1.5T). At higher field strengths, recovering from the CPMG violation is much harder. Very little literature is available on FSE-based non-CPMG DWI at high fields. A few groups have published work on clinical 3T magnets (Attenberger et al., 2009; Sarlls and Pierpaoli, 2008), but there is a striking lack of publications at 7T.

This work addresses the problem by acquiring diffusion-weighted images using PROPELLER MRI while maintaining the CPMG condition.

6.2 PROPELLER DWI with distributed diffusion gradients

Figure 23 shows the pulse sequence diagram of the diffusion-weighted PROPELLER sequence with distributed diffusion gradients. The diffusion gradients are essentially just larger area crusher gradients (circled in red) played out on either side of the refocusing pulses on the slice-selective gradient axis.

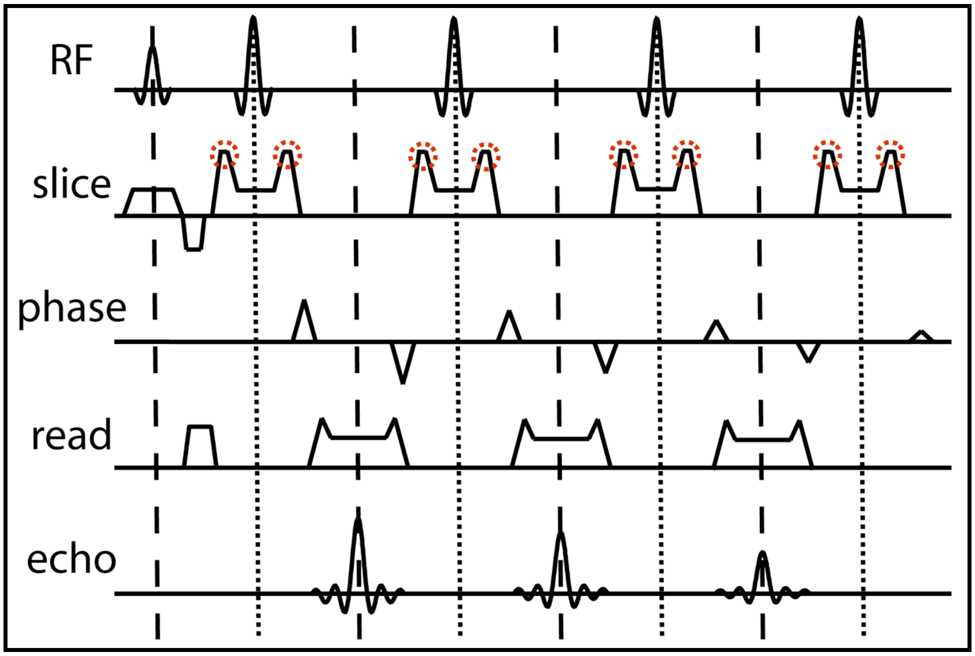

Figure 23: Pulse sequence diagram for diffusion-weighted PROPELLER using distributed diffusion gradients (circled in red)

As the diffusion gradients are symmetrically placed around all refocusing pulses, the CPMG condition in this case is still maintained. Also, since there are multiple little gradients, each one is not prohibitively large as is the case with bipolar diffusion gradients. This allows the echo spacing to still be relatively short, which for a high-field application, is a definite benefit. Increasing the amplitude of these distributed gradients increases the diffusion sensitivity. Additionally, increasing the area of the crusher gradients around the readout gradient as well can further increase the diffusion sensitivity of the sequence.

Figure 24 shows the results of the preliminary experiment that demonstrated the proof of this concept. The experiment used a phantom consisting of three solutions with different diffusion coefficients: glycerol (0.8×10^{-3} mm^2/s), water (2.06×10^{-3} mm^2/s), and acetone (4.8×10^{-3} mm^2/s).

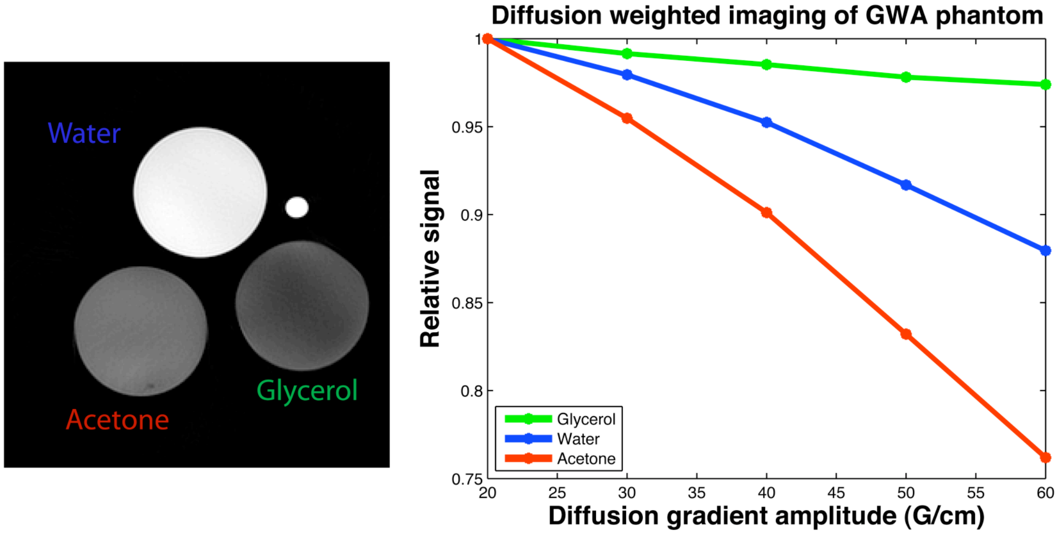

Figure 24: Phantom results for diffusion-weighted PROPELLER using distributed diffusion gradients. The signal intensity for the all three solutions decreases with increasing gradient amplitude. The rate of signal decay correlates with the diffusion coefficients of the solutions, with acetone having the fastest decay and glycerol the slowest.

As expected, the signal decreases with increasing gradient amplitude (and hence gradient area) for all three solutions. The rate of signal decay is different for the three solutions and corresponds with the differing diffusion coefficients of the three solutions. Acetone has the largest diffusion coefficient and hence the fastest decay rate. Glycerol, which has the lowest diffusion coefficient, shows the most gradual signal decay.

Thus this experiment demonstrates that the proposed DWI sequence with distributed diffusion gradients is able to distinguish solutions based on their diffusion characteristics. But for rigorous analysis of biologic tissues, it is important to be able to extract quantitative parameters from the images, in this case the apparent diffusion coefficient (ADC).

ADC calculation requires that the b-value of the sequence be known (Eq. [6.6]). Traditionally, the b-value of a sequence has been calculated analytically using Eq. [6.7], where TE (echo time) is the time interval between the excitation pulse and received echo. But for the PROPELLER sequence, each acquired echo has a distinct TE, and the effective TE for the entire image is defined as the time interval between the excitation pulse and the echo that samples the central line of k-space. Likewise, each echo has a distinct b-value (cumulatively calculated till the TE for that echo), while the image as a whole has an effective b-value. Using a definition similar to that for effective TE, the effective b-value can be calculated from Eq. [6.6] by replacing TE with effective TE.

Table 9 lists the calculated effective b-values for 2-shot PROPELLER (ETL = 6) with distributed diffusion gradients for three different acquisition orders depending on the echo used to sample the center of k-space: early (first echo), intermediate (fourth echo) and late (sixth echo). The echo spacing (ESP) was kept constant at 8.5 ms and each diffusion gradient was 1.3 ms wide. The b-values were calculated for increasing diffusion amplitudes starting with a baseline value of 15 G/cm going up to 55 G/cm in increments of 5 G/cm.

Table 9: Calculated b-values for 2-shot PROPELLER with distributed diffusion gradients for early, intermediate and late echo ordering with increasing diffusion gradient amplitudes.

Gradient Amplitude (G/cm)	Early echo order (s/mm^2)	Intermediate order (s/mm^2)	Late echo order (s/mm^2)
15	6.69	26.75	40.13
20	11.89	47.56	71.34
25	18.58	74.31	111.46
30	26.75	107.00	160.50
35	36.41	145.64	218.46
40	47.56	190.23	285.34
45	60.19	240.76	361.13
50	74.31	297.23	445.85
55	89.91	359.65	539.47

The calculated b-values for the late ordering are in the range typically obtained with Stejskal-Tanner bipolar gradients with similar gradient amplitudes but with pulse widths three times as long as the ones used here. So the question is, are they accurate?

A phantom experiment with the same imaging parameters as those in the above calculations was carried out. The phantom was a water bottle with an ADC of 2.06×10^{-3} mm^2/s. Thus, using this known ADC, the b-values were experimentally determined from the acquired images. The experimental b-values are given in Table 10.

Table 10: Experimentally determined b-values for identical imaging parameters as used in Table 9.

Gradient Amplitude (G/cm)	Early echo order (s/mm^2)	Intermediate order (s/mm^2)	Late echo order (s/mm^2)
15	0	0	0
20	15.36	18.40	21.99
25	32.76	41.88	50.11
30	54.34	69.94	84.58
35	78.22	102.75	125.77
40	106.09	139.81	172.35
45	136.14	181.55	225.47
50	168.07	227.37	285.39
55	203.04	276.60	350.36

Figure 25 shows a graphical comparison of the experimental b-values and the theoretically calculated b-values. For the theoretical values, the b-value for gradient amplitude of 15 G/cm is subtracted from the higher amplitude b-values so as to match the experimentally determined values where the gradient amplitude of 15 G/cm is the baseline and thus assumed to have a b-value of 0.

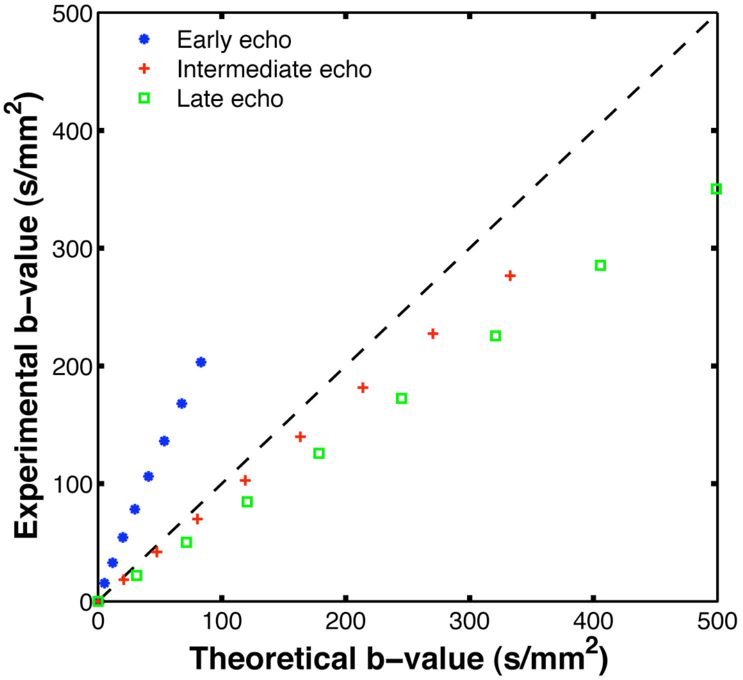

Figure 25: Comparison between experimentally determined and theoretically calculated b-values for diffusion-weighted 2-shot PROPELLER with distributed diffusion gradients

The experimentally determined b-values were larger than the theoretical b-values for the early echo ordering. For the intermediate and late ordering, the theoretical values were larger than those observed experimentally. This is reasonable, as the theoretical calculation did not take into account the sampling strategy and the proximity of the other lines (echoes) in the blade that have a different b-value. The true b-value for such a sampling strategy would be a weighted combination of the b-values seen by each echo. Since the theoretical calculation assumed a single b-value, it under-estimated the b-values for the early ordering and over-estimated the values for the later echo ordering schemes. Nonetheless, as expected, the later echo ordering schemes had larger b-values than the early echo ordering. Thus, the decision was made to use the late ordering scheme for the DWI studies. Since theoretical determination of b-values did not provide an accurate estimation of the true b-value, a better technique for quantitative information extraction was needed.

6.3 Methods

A practical solution was to back-calculate the b-values using known ADC values, for each of the diffusion-weighting steps. The known ADC values, or controls were chosen based on available literature (Delakis et al., 2004; Laubach et al., 1998) so as to span a biologically relevant range – 0.4 to 5.0×10^{-3} mm^2/s. The ADC values of the controls were first determined using a standard spin echo sequence (Stejskal and Tanner, 1965). Since this measurement is temperature sensitive, the magnet bore was maintained at a temperature of 33-34°C. This corresponded to the temperature range used for the animal studies. Sinusoidal diffusion gradients with a pulse width of 3.5ms were played out on either side of the refocusing pulse (TE/TR = 12 ms/2s). The gradient amplitude was progressively increased from 0 to 70 G/cm in steps of 7 G/cm to get 11 diffusion-weighting steps with b-values ranging from 0 to 726 s/mm^2. The ADC values were determined using a non-linear least squares fitting algorithm. These values were confirmed with those found in literature (Ong et al., 2005).

Table 11: Controls and their measured ADC (Reproduction of Table 4)

Solution	**Apparent Diffusion Coefficient**
3% Agarose	2.66×10^{-3} mm^2/s
2% Agarose	2.77×10^{-3} mm^2/s
$CuSO_4$ (2:1 dilution with D_2O)	2.08×10^{-3} mm^2/s
$CuSO_4$ (3:1 dilution with D_2O)	1.98×10^{-3} mm^2/s
Sucrose solution (400g/l)	0.92×10^{-3} mm^2/s

6.4 Phantom Experiments

In the phantom experiment, the same controls (from above) were reimaged using the PROPELLER sequence with distributed diffusion gradients. The diffusion gradient (crushers on z-axis) amplitude was varied from 7 G/cm to 70 G/cm while the pulse width was kept constant at 1.3 ms. Using the 2-shot technique with late-echo acquisition (ETL = 6), images were acquired for an effective TE of 50.5 ms and TR of 2s. The temperature was again maintained between 33-34°C.

6.4.1 Results

Figure 26 shows the signal response to increasing gradient amplitude, i.e. increasing diffusion-weighting for SE and PROPELLER. For SE data (left), the signal decays as expected. For PROPELLER data (right), both the Agarose and $CuSO_4$ solutions show signal decay. The Sucrose solution, contrary to logic, shows increase in signal with increasing gradient amplitude.

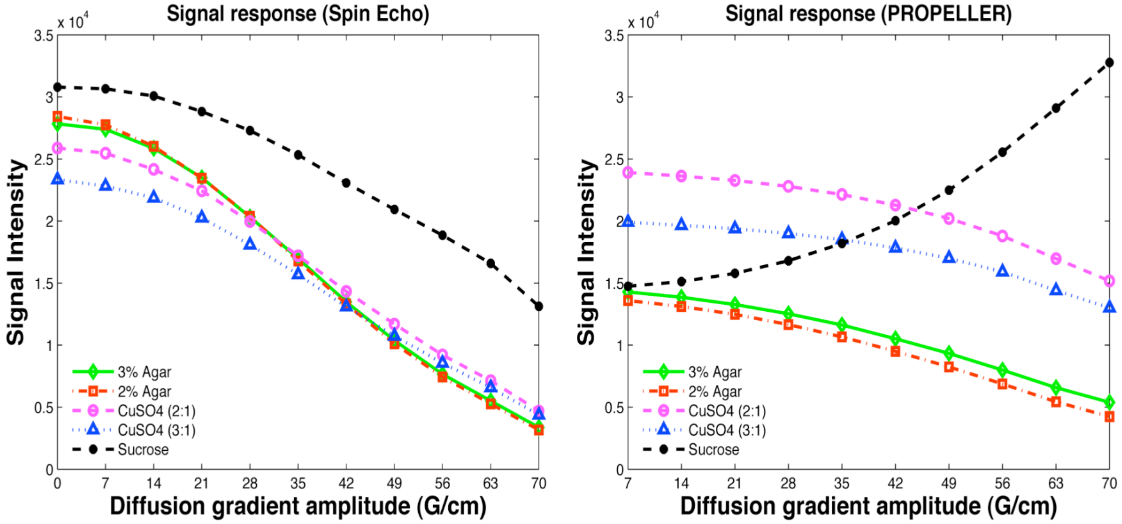

Figure 26: Signal decay as a function of increasing diffusion gradient amplitude for (left) spin echo sequence with Stejskal-Tanner diffusion gradients and (right) PROPELLER with distributed diffusion gradients.

Calculated b-values for the different diffusion-weighting steps with the PROPELLER sequence are shown in Fig. 27. For obvious reasons, the Sucrose data were not used for these calculations. There is good agreement between the b-values calculated from the two $CuSO_4$ solutions, but those from the Agarose solutions are significantly higher.

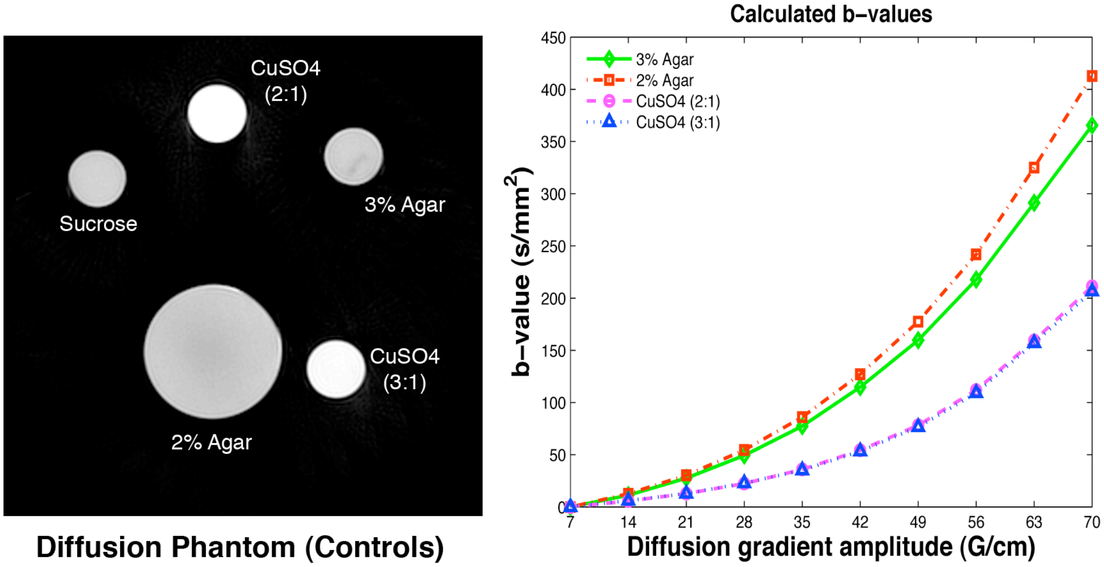

Diffusion Phantom (Controls)

Figure 27: Calculated b-values for PROPELLER DWI with distributed diffusion gradients for different gradient amplitudes using the known controls.

6.4.2 Discussion

Signal attenuation due to diffusion increases as the area of the diffusion-weighting gradient is increased. The larger gradient pulses cause greater amplification of the dephasing effect due to diffusion of molecules. Thus the unexpected increase in Sucrose signal at higher gradient amplitudes (Fig. 26) was confusing. The same experiment was repeated multiple times, but the signal increase was consistent. The distributed-diffusion PROPELLER sequence is a much more complicated sequence than was originally believed.

The PROPELLER sequence uses a multi-echo acquisition. Imperfections in the refocusing pulses cause numerous different coherence pathways to be formed. A possible explanation for the signal increase could be that the magnetization gets flipped to the longitudinal axis by an imperfect refocusing pulse and hence does not decay as much. The Sucrose solution might retain more magnetization towards the end of the echo train, while that from the other solutions gets dissipated. Another explanation for the signal increase could be the occurrence of some constructive interference along the lines of Hyperechoes (Frank et al., 2003; Hennig and Scheffler, 2001). A thorough analytical solution for this problem is beyond the scope of this work, but there is a clear need to gain a better insight of this sequence.

The decision to empirically calculate b-values using controls with known ADC values was made because the analytical b-value calculation was inaccurate. The analytical calculation did not take into account the k-space sampling trajectory and thus provided only a rough estimate of the b-value. But, as shown in Fig. 27, the empirically calculated b-values are inconsistent. This brings to light another aspect of this technique that would need a thorough analytical solution, the influence of the longitudinal (T_1) and transverse (T_2) relaxation times on the total signal attenuation.

Conventionally, for quantitative diffusion weighted imaging, S_0, the signal without diffusion weighting gradient (Eq. [6.6]), is considered a separable component of the total signal S. For the multi-echo PROPELLER sequence, where each echo (acquired k-space line) has a different echo time and diffusion weighing, and the magnetization is repeatedly, though imperfectly, refocused, this is no longer true. The T_1 and T_2 relaxation effects cannot be separated from the diffusion effects. The simplistic b-value calculation in Fig. 27 did not take this into account, and could be the reason for inconsistent b-values. The two pairs of Agarose and CuSO4 solutions had similar relaxation times, and this is reflected in the calculations, where the b-values from each pair are in fairly good agreement.

The same non-separability argument can be further extended to the proposed in vivo quantitative DWI experiment, where an accurate determination of tissue ADC would first require the calculation of the T_1 and T_2 values for that tissue (Deoni et al., 2004).

6.5 Animal Experiments

6.5.1 Results

Figure 28 shows the comparison between baseline T_2-weighted 2-shot PROPELLER and diffusion-weighted PROPELLER using distributed diffusion gradients. The effective TE and TR for both acquisitions were kept constant. Identical slices from the two multi-slice datasets are shown in Fig. 28. The difference in the two images is most noticeable in the spine, where the diffusion-weighted image (Fig. 28b) has much higher contrast.

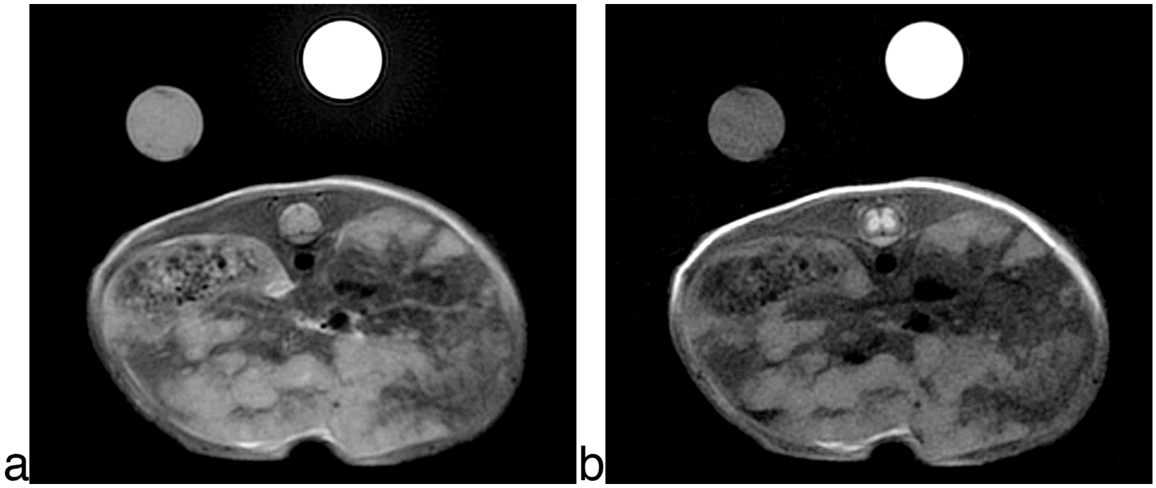

Figure 28: Diffusion-weighted images of liver tumors in free-breathing mice using 2-shot PROPELLER with distributed diffusion gradients. 125 μm in-plane, 1 mm slice thickness (9 slices), ESP/TE/TR = 8.4 ms/51 ms/3s, ETL = 6 (late echo ordering), imaging time ~ 20 minutes. (a) is the baseline image with the usual z-axis crushers, (b) is diffusion-weighted with 1.3 ms wide crusher gradients with an amplitude of 45 G/cm.

6.5.2 Discussion

From the results of the phantom experiments it was apparent that quantitative diffusion-weighted imaging using PROPELLER with distributed diffusion gradients was as yet not possible. Nevertheless, the technique showed promising results for qualitative diffusion-weighted imaging. In some diagnostic application, obtaining diffusion-weighted images with high SNR may be more important than obtaining accurate diffusion information (Conturo et al., 1995).

Diffusion-weighted imaging in small animals is a challenging task due to the higher sensitivity to motion. In addition, lower signal levels make obtaining high-spatial resolution images even more so. The images in Fig. 28 have an in-plane resolution of 125 μm, which is nearly a four-fold improvement over published work in small animals (Chen et al., 2007; Herneth et al., 2003; Sun et al., 2009). Furthermore, the multi-slice datasets were acquired without respiratory or cardiac gating in free-breathing mice. This reinforces the advantages of the 2-shot PROPELLER technique for small animal imaging.

For diffusion-weighted imaging in the liver, b-values ranging between 0 and 500 s/mm^2 are appropriate for lesion characterization (Koh et al., 2006; Nasu et al., 2006). Though the exact determination of the b-values is beyond the scope of this work, results from the phantom experiments suggest that the sequence is capable of b-values in this range. Moreover, the distributed diffusion gradients were only applied on the z axis. The technique could be easily extended to the x and y axes to get higher b-values.

6.6 Conclusion

2-shot PROPELELR with distributed diffusion gradients explores a novel technique for diffusion-weighted imaging using a multi-echo acquisition. Results in free-breathing mice with liver metastases are promising. This technique allowed us to obtain high-resolution diffusion-weighted images, even in the presence of severe motion.

Significant work is still needed to expand this technique into a fully functional quantitative protocol. A through analytical modeling of the sequence is first necessary to understand the interactions between the multiple refocused acquisitions (differences in relaxation and diffusion-weighting) and the k-space filling pattern.

7. Multimodality Longitudinal Liver Study

The preceding chapters describe the work done towards developing a rigorous cancer imaging protocol. The final step is its application to a biologically significant study. This chapter describes the high-throughput, longitudinal cancer study that was the main motivation behind the whole project. The disease model chosen for this study was liver metastases in a mouse model of human colon carcinoma.

7.1 Introduction

Colon and rectal cancer is the third most common type of cancer in both men and women (Jemal et al., 2009). Colorectal cancer commonly metastasizes to the liver, at which point morbidity and mortality drastically increases. In a third of the patients who die of colorectal cancer, metastatic disease is found only in the liver. Metastases in the liver are also seen in a number of other cancers, e.g. pancreas, stomach, breast, and lung cancers. Liver is one of the most common sites of distal metastases, second only to lymph nodes. Early detection and effective treatment of liver metastases would greatly improve the prognosis for many patients.

Preclinical orthotopic disease models, which closely mimic the conditions seen in human tumors, are a tremendous resource. Non-invasive visualization of these animal models provides the ability to longitudinally monitor tumor growth and the effect of therapies. But the location of the liver, under the diaphragm, makes it challenging due to severe motion effects. The PROPELLER MRI technique, with its motion correction ability and excellent T_2-weighted contrast, along with the infrastructure developed in this work are ideal for this application. But since there are several imaging modalities that are now available for detection and characterization of liver lesion, it is important to analyze the relative merits of this technique against them. To the best of our knowledge, a rigorous study of this kind has not been undertaken in preclinical research.

There is considerable published literature (Kinkel et al., 2002; Oliva and Saini, 2004; Reimer et al., 2000; Schima et al., 2005) in the clinical domain that has compared various imaging modalities, including Ultrasound (US), Computed Tomography (CT), Positron Emission Tomography (PET) and Magnetic Resonance Imaging (MRI). Due to their high sensitivity and specificity, as well as the ability to provide anatomic information, the modalities of choice for imaging liver metastases have been either contrast-enhanced CT or MRI, both non-enhanced and contrast-enhanced. The advantages of CT include its availability, lower cost, higher spatial resolution, and rapid imaging times. The benefits of MRI include superior tissue contrast, non-invasive and non-radioactive acquisitions, and increased flexibility afforded by the wide array of MR pulse sequences and contrast agents that are available.

In the preclinical domain too, mouse models of liver cancer have been studied using various modalities; PET (Zhao et al., 1999), Bioluminescence imaging (Inoue et al., 2007; Smakman et al., 2004), CT (Martiniova et al., 2009b), and MRI (Baboi et al., 2009; Cai et al., 2005; Kalber et al., 2008), albeit independently. PET imaging provides excellent functional information regarding tumor metabolism. But it is costly, not widely available, and in small animals is limited by spatial resolution. Optical techniques, like bioluminescence imaging, though highly sensitive are also limited by spatial resolution, as well as the need to generate mouse models that genetically express luciferase. CT is more readily available, and provides high spatial resolution. It is also the preferred modality for liver imaging clinically, making translational studies more appealing.

Thus, we decided to compare the relative merits of the proposed PROPELLER technique with the established contrast-enhanced CT, for the specific application of imaging liver metastases in mouse models.

7.2 Methods

7.2.1 Animal model

All animal studies were approved by the Duke University Institutional Animal Care and Use Committee. The tumor inoculation procedures were carried out at Piedmont Research Center (Morrisville, NC). Female athymic nude mice were implanted with 5×10^6 cells of HT29 colon carcinoma in a volume of 50 μl with a 25-gauge needle in the spleen. After a two-minute pause post-injection, a splenectomy was performed and the surgical site was closed. The procedure was conducted under isoflurane anesthesia. Animals were allowed to recover for 9 days before imaging.

This model was unique as it enabled the study of secondary tumor sites. The primary site of tumor, which normally dominates the disease model, was removed by splenectomy. This allowed for sufficient time for the secondary tumor sites to develop, which in this case were liver metastases. For a colon carcinoma cell line, the liver is the primary site of metastases. This was also a very aggressive disease model. After an initial two-week period, the tumors showed exponential growth in the liver. Thus the total duration of the experiment was restricted to about a month from the date of implantation, by which point the mice had reached the humane end point for acceptable tumor burden. Figure 29 shows a picture of an excised liver 31 days after tumor inoculation.

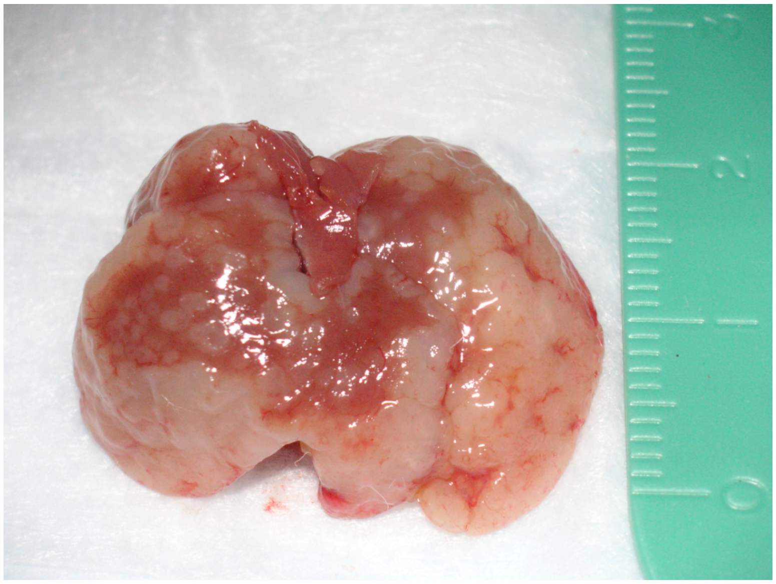

Figure 29: Excised liver 31 days after tumor inoculation. Tumor penetration (white) at this stage is more that 90% and the liver also has a significantly increased volume.

7.2.2 Experimental design

The experimental design was based on the constraints of the disease model. Figure 30 shows the experiment timeline. Day 0 is the tumor inoculation day, followed by a recovery period of 9 days. The imaging started at day 10 (after the surgery recovery period) and went upto day 31 (humane end point). 8 mice were imaged twice a week for a total of 7 time points with both MR and CT. Mice that were lost due to excessive tumor penetration before the last time point were replaced by others from the same cohort. 4 mice survived the entire study, and their histological data were acquired after the last imaging day. Data for the intermediate histology time points were acquired from a separate set of mice, which also underwent an in vivo MR imaging session.

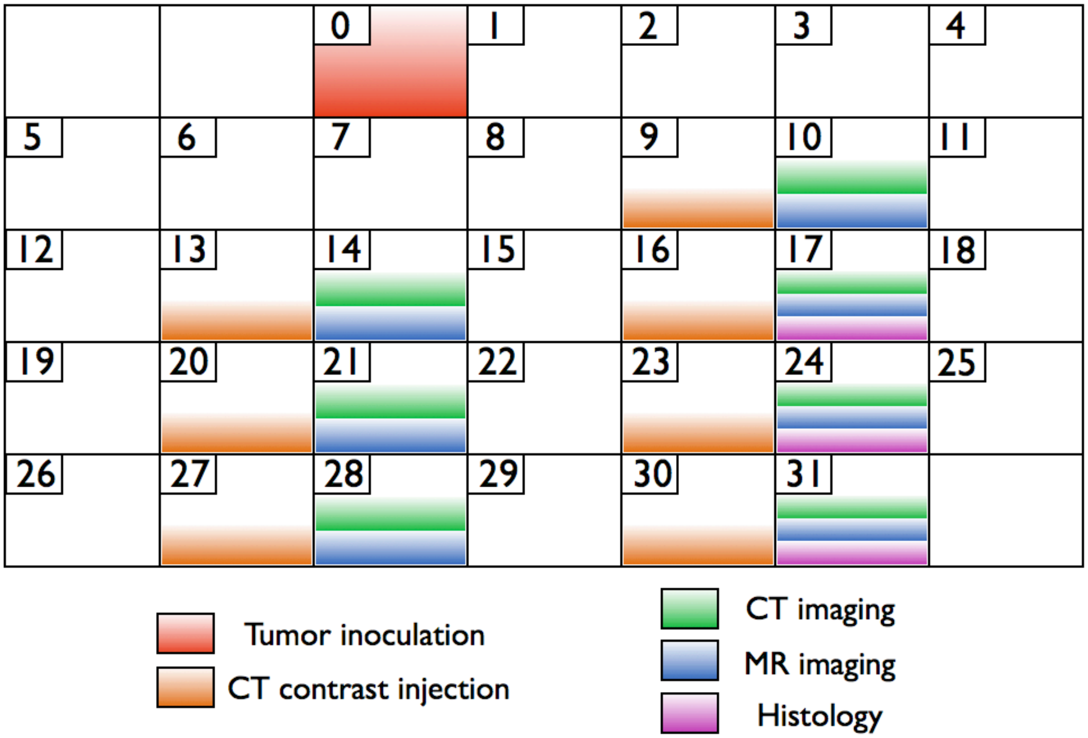

Figure 30: Experiment timeline for the longitudinal liver metastases study

The challenges of scaling CT imaging from the clinical (human) to the preclinical (small animal) domain include many of the same challenges that are faced in MRI. The most notable is that the scan time for most preclinical CT scanners is longer than that required for clinical imaging. In addition, the clearance of conventional iodinated contrast agent is relatively more rapid in the small animal since the blood transit time is shorter. The result is that contrast agents that are routine in the clinical arena are not as effective for small animal CT. This problem was addressed through the use of a contrast agent with a significantly longer biological half-life – a blood pool contrast agent. The contrast agent used was Lp-I (Mukundan et al., 2006). This is a vascular contrast agent that gets broken down in the liver. Thus the viable liver, which took up the contrast agent, was hyperintense in the CT images. The diseased liver, the tumors, remained unenhanced.

It was crucial to select an appropriate contrast injection schedule. Imaging too soon after the contrast injection meant that the liver was not sufficiently enhanced. On the other hand, waiting for too long after the injection meant that all the contrast agent had washed out of the blood vessels, making it hard to differentiate between the liver vasculature and the liver metastases. A preliminary experiment was undertaken to study the evolution and clearance of the CT contrast agent.

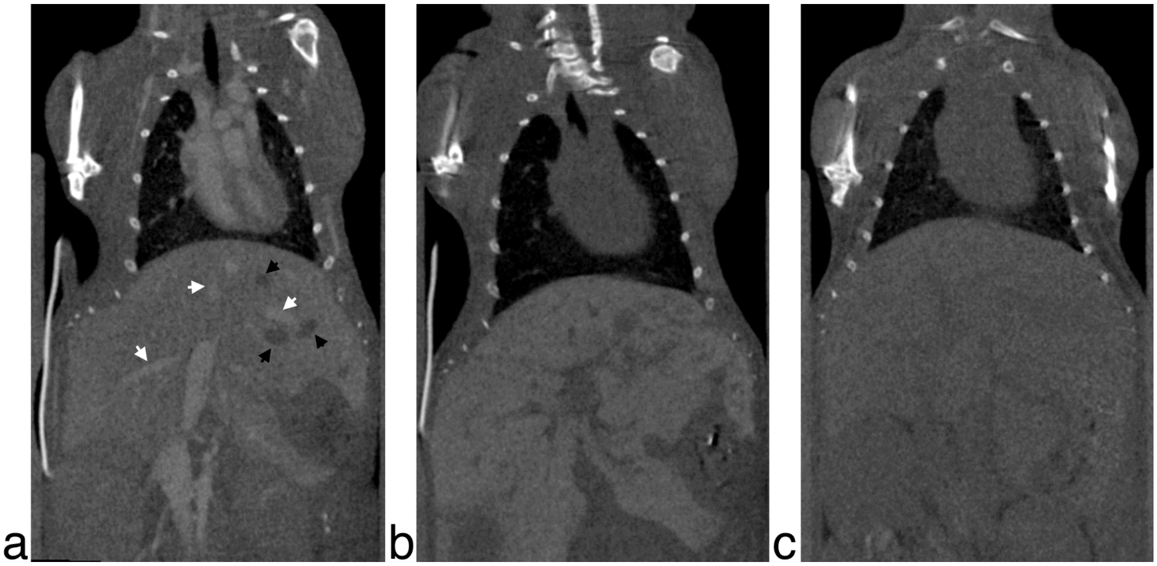

Figure 31: Contrast-enhanced CT images acquired (a) day 1, (b) day 5, and (c) day 8 post contrast injection. Arrowheads in (a) indicate tumors (black) and blood vessels (white).

Figure 31 shows the results of the experiment at three different time points after contrast injection – day 1 (Fig. 31a), day 5 (Fig. 31b) and day 8 (Fig 31c). As is evident from the images, administering the contrast agent one day (between 16-18 hours) before the imaging experiment provided the necessary level of control on the contrast levels in the image. The viable liver was enhanced due to the contrast agent; the tumors were dark (black arrowheads) due to the lack of contrast agent; and the vasculature (white arrowheads) remained bright, as the contrast agent had not yet washed out. The images acquired at day 5 post-injection showed similar low intensity values for both tumors and vasculature, while those at day 8 were virtually devoid of contrast (similar to pre-contrast images). The experiment also included a set of mice that were given an initial full dose (0.4ml/25g), followed by half doses (0.2ml/25g) for the later time points, but the results were unsatisfactory. A point to be noted here is the images shown in Fig. 31 were acquired after the first contrast injection, and in Fig. 31a, the vasculature is brighter than the viable liver. But as the contrast clearance rate from the liver (about 8-10 days) is slower than the rate at which it is injected (every 3-4 days), the liver got progressively brighter during the course of the experiment. Thus at later time points, the viable liver was brighter than the vasculature. Nonetheless, the three distinct contrast levels were maintained by this injection schedule.

A second concern was the effect that the CT contrast agent could potentially have on the contrast in the MR experiment. Iodinated contrast agents have been known to alter T_1 and T_2 (Hergan et al., 1995). To address this concern a separate set of experiments was conducted in which tumor-bearing mice were imaged with MR one day before the administration of CT contrast agent, as well as days 1, 2 and 3 post-contrast injection. But the CNR measurements between the tumor and the liver from these serial MR datasets showed no statistically relevant variations.

In all imaging experiments (CT and MRI), the mice were free-breathing and maintained under anesthesia by Isoflurane administered via a nose cone. The respiratory rate was monitored throughout the course of the study (SA Instruments Inc., Edison, NJ). Surface body temperature was measured with a thermistor that was placed snugly under the neck. The temperature was maintained between 33-34°C; by blowing warm air into the magnet bore for the MR studies, and by a heat lamp for the CT studies. An integrated animal cradle that addressed the anesthesia delivery, physiological signal monitoring, and animal-positioning needs for both CT and MRI was used for these studies. After the intermediate imaging sessions, the mice were administered 0.5 ml of saline and returned to their cages. At the conclusion of the final imaging timepoint, the mice were either euthanized with anesthesia-overdose or were perfusion-fixed for histology.

7.2.3 MR imaging protocol

All MR imaging was carried out on a 7T, 150 mm bore, Magnex magnet with a GE EXCITE console on the EPIC Lx12.4 software platform (GE Healthcare, Milwaukee, WI). The system uses shielded gradient coils (Resonance Research Inc., Billerica, MA) with a maximum gradient strength of 770 mT/m and a rise time of 100 μs. High-power amplifiers (Copley Controls, Canton, MA) drive the gradients. The strong gradients with high slew rate, high duty cycle and high power amplifiers were necessary to achieve the short inter-echo spacing (ESP) that is critical at high fields to minimize susceptibility-induced losses. The RF coil used for imaging was a 35 mm diameter quadrature transmit/receive volume coil (M2M Imaging Corporation, Cleveland, OH).

2-shot PROPELLER (Pandit et al., 2010a; Pandit et al., 2010b) was used to obtain ungated, heavily T2-weighted images with TE = 67ms, TR = 3s. Multi-slice axial datasets covering the entire abdominal region (125µm in-plane, 1mm slice) were acquired in ~30 minutes. Image reconstruction was carried out with an offline MATLAB program as described in Chapter 5.

7.2.4 CT imaging protocol

All CT imaging was performed with a dual imaging chain microCT system (Fig. 32), consisting of two x-ray tubes with a 0.8mm focal spot and two cooled CCD cameras

(Badea et al., 2004). The scanner has a vertical rotating stage on which the animals were placed in the integrated animal cradle. This system is optimized to have a high photon flux and thus provides what we believe to be the highest SNR currently available with microCT. Scans of 25 mm water phantom using the same acquisition parameters as used for the animal studies yielded an average noise level of 68 HU.

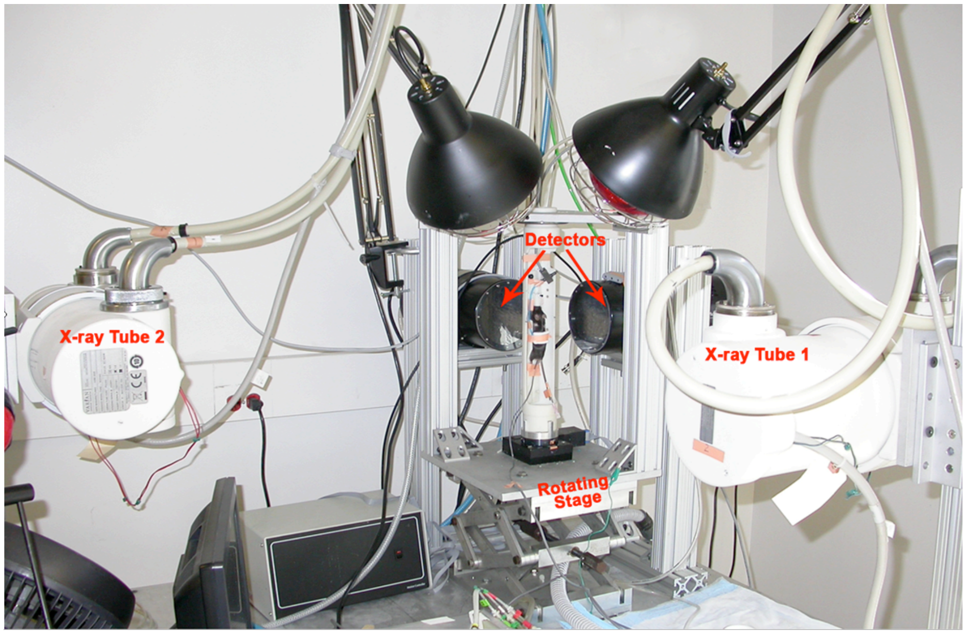

Figure 32: Dual CT scanner with vertical, rotating animal stage.

Only one imaging chain was used for this experiment. Each scan consisted of 300 projections with a 0.65° step angle, acquired at 80 kVp, 160 mA, and 10ms exposure. A pressure-sensitive sensor in the cradle provided the necessary signal for respiratory-triggered acquisitions. Volume imaging with 88μm isotropic resolution were acquired in ~5 minutes. Images were reconstructed in MATLAB with 512 x 512 x 640 array covering a 45 x 45 x 56 mm^3 field of view. To enable a fair comparison with the MR images, the same CT data were also reconstructed with isotropic resolution of 125 μm, the same resolution as the in-plane resolution in the MR data. 8 contiguous slices were averaged together to generate 1mm thick slabs, thus yielding a second set of axial CT images with the same (anisotropic) resolution as the MR data.

7.2.5 Conventional Histology

Conventional histology was performed in a fashion that would permit correlation between hematoxylin and eosin (H & E) slides and in vivo CT and MR images. The mice were transcardially perfused with 10% buffered formalin in such a way that the abdominal region (from diaphragm and below) remained intact. The fixation procedure was carried under Isoflurane anesthesia delivered via a nosecone. An initial 4 minute saline flush at 8ml/min was followed by 10% formalin for 5 minutes at the same rate. The fixed specimens were kept in 10% formalin solution for atleast a week and then transferred to 70% alcohol one day prior to histology sectioning. Based on the in vivo MR datasets, the specimens were sectioned into 4 slabs around regions that clearly showed both viable liver tissue as well as diseased tumor tissue. 2/3 H & E slides with a thickness of 5 μm were created from each slab.

7.3 Results

A representative T_2-weighted MR image acquired in this study is shown in Fig. 33. Multi-slice datasets with an in-plane resolution of 125 μm and 1mm slice thickness were acquired in 30 minutes. The entire thorax and abdomen of the mouse was imaged with a total of 31 slices. The slice in Fig 33 shows a number of anatomical features – kidneys (thick arrows), stomach (thin arrow on left), and intestines (thin arrow on right). In a T_2-weighted image, the liver tumors are hyperintense (arrowheads) on the darker background, which is the viable liver.

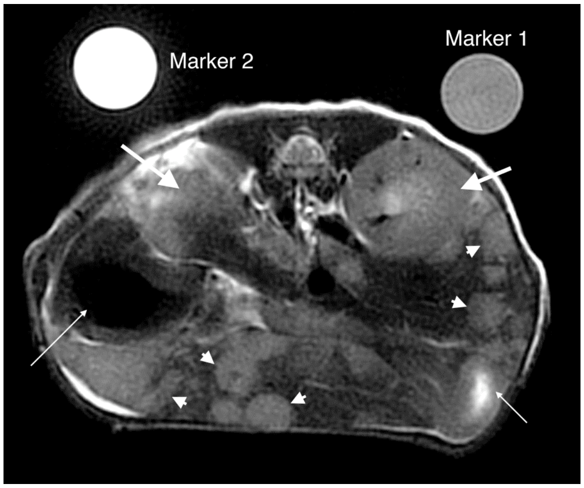

Figure 33: Representative slice showing T_2-weighted MR image of a mouse with liver metastases. Arrowheads point towards liver metastases, which are hyperintense on the lower intensity viable liver. Also seen in the image are kidneys (thick arrows), stomach (thin arrow on left) and intestines (thin arrow on right). Marker 1 (3% Agarose) and Marker 2 (CuSO4) were used for quality control.

Also seen in the image are the two markers used for assessing the measurement consistency in the MR datasets. Marker 1 has signal intensity (~10,000) comparable to the intermediate values in the live animal while marker 2 (~30,000) is representative of the higher intensities. The markers showed minimal deviation (6.3% and 5.3% respectively) in measurements taken over multiple slices, different datasets, and all seven imaging days. These shifts were considered to be within acceptable bounds imposed by systemic variations.

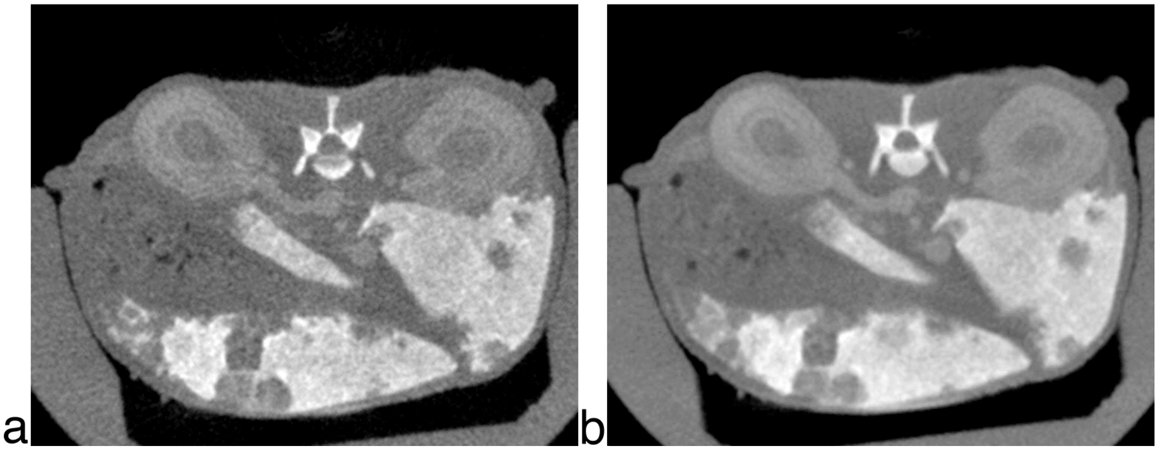

Figure 34: Representative slice of contrast-enhanced microCT image of a mouse with liver metastases. (a) Reconstruction with 88 μm isotropic resolution, (b) Reconstruction with 1 mm slice thickness and 125 μm in-plane resolution.

Figure 34 shows the corresponding slice from the same mouse on the same day with contrast-enhanced CT. Respiratory-gated CT images had an acquisition time between 5 to 7 minutes. The acquired data in CT can be reconstructed in multiple different ways. On the left (Fig. 34a) is the highest resolution, 88 μm isotropic resolution that is the default reconstruction for the scanner. The image on the right (Fig. 34b) has been reconstructed at a lower resolution to match that of the MR images and make contrast to noise measurements more meaningful. In the CT images, the viable liver is hyperintense due to the contrast agent uptake. In contrast, the tumors, which do not take up any contrast agent, are dark. The blood vessels, as well as the kidneys, have medium signal intensity, as the contrast agent has not yet completely washed out. The stomach (on the left) can be differentiated by the presence of small air pockets. 8 consecutive slices, each 125 μm thick, are averaged together to generate the 1 mm thick slice (slab) for the lower resolution images. As expected, the lower resolution images have a CNR that is higher than the high-resolution images, 11.91 versus 8.25 (Ford et al., 2003).

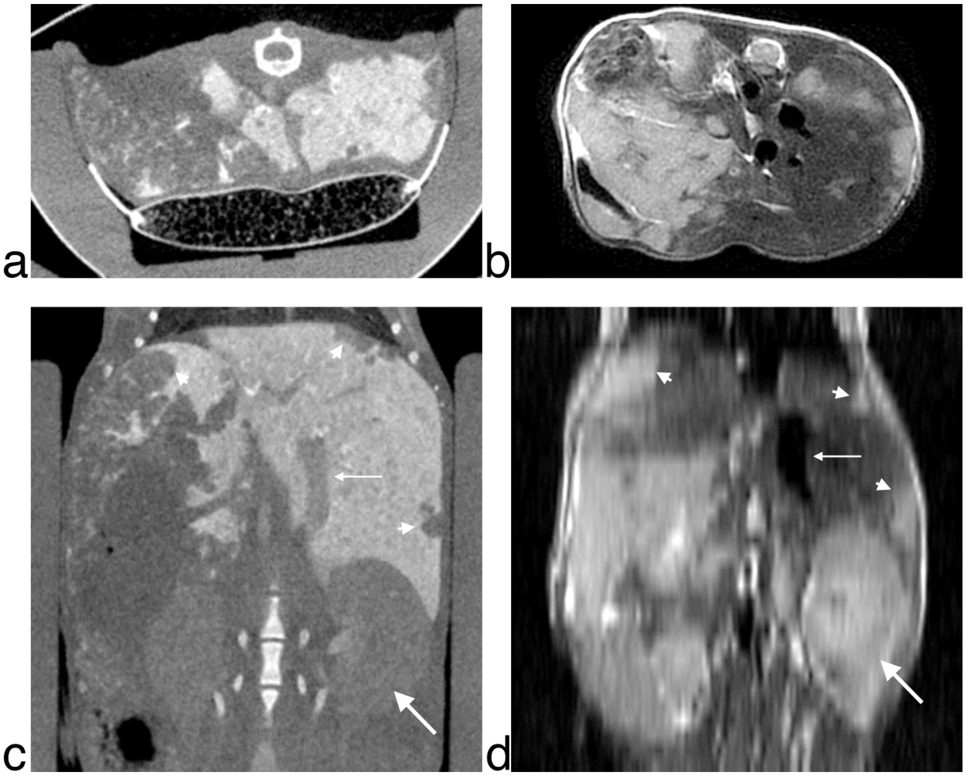

Figure 35: Axial dataset (a, b) along with coronal resection (c, d) with CT and MR respectively. The coronal section shows the left kidney (thick arrow), the inferior vena cava (thin arrow) and multiple tumor nodules (arrowheads).

As the CT images have high isotropic resolution, it is possible to resection the data in any plane. Figure 35 shows coronal resections for both CT and MR. Comparison between Fig 35c and 35d clearly shows the benefits of the isotropic CT resolution. As the MR images have a much lower resolution (1 mm) in the slice direction, coronal resections have a blocky appearance due to excessive interpolation.

The animal is placed horizontally (prone) for the MR studies, while for the CT studies it is vertical. The difference in gravitational effects during the two positions makes it difficult to obtain exactly matching slices from the two modalities, though such an attempt has been made in all the images shown here. Coronal section in Fig. 35c and 35d are roughly at the same level in the mouse. The left kidney (thick arrow) can be clearly seen in both datasets. Also seen is a section of the inferior vena cava (thin arrow). Tumors in the CT data are hypointense, while in the MR data, they are hyperintense (arrowheads). The region on the lower left, with the same intensity levels as the tumors, is the intestine. It is easier to differentiate it on the MR images by the presence of a brighter lumen.

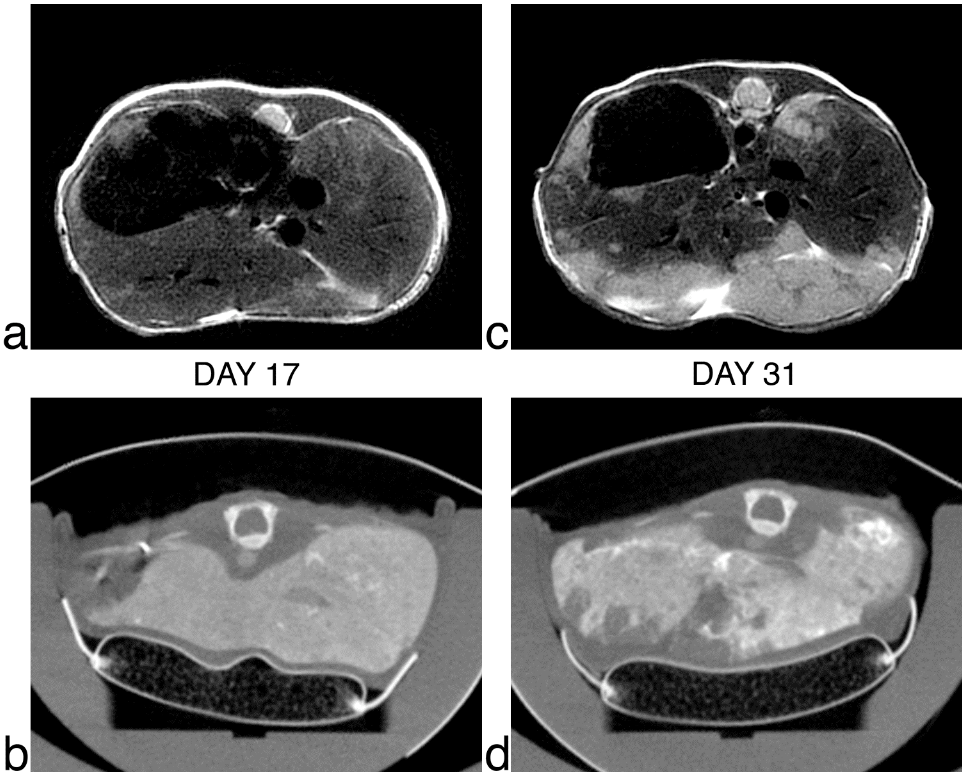

Figure 36: Representative slices from MR (top) and CT (bottom) datasets acquired at an early (a, b) and late (c, d) timepoint during the longitudinal study. In-plane resolution = 125 μm, slice thickness = 1 mm. Ungated, T_2- weighted MR datasets (a, c) were acquired with 2-shot PROPELLER in 30 minutes. Contrast-enhanced, respiratory-gated CT datasets (b, d) were acquired in 6 minutes.

Figure 36 shows an early and a late time point in the same animal during the course of disease progression, with both MR (Fig. 36a, 36c) and CT (Fig. 36b, 36d). All images have been reconstructed to have an in-plane resolution of 125 μm and a slice thickness of 1 mm. The early time point (Fig. 36a, 36b) is 17 days after tumor-inoculation and the late time point (Fig. 36c, 36d) shows the same slice at day 31. The tumors can be clearly seen at day 31— hyperintense on the MR image (Fig. 36c) and hypointense on the CT image (Fig. 36d). At day 17, the tumors are too small to enable clear differentiation with either MR or CT. But, while the CT image provides almost no information, the MR images appear to have increased intensity in the regions that at the later timepoint are clearly tumors.

A more detailed time course in a different mouse is shown in Figure 37. The first time point is again at day 17, as datasets from earlier timepoints do not provides much information with either modality. The top row (Fig. 37a-e) shows the MR time series, while the bottom row (Fig. 37f-j) shows the corresponding CT images. The slice depicted in Fig. 37 shows three distinct tumor nodes in the lower liver lobe that can be tracked with both modalities. The tumors are easier to distinguish in the early MR images than in the early CT images. MR images also show greater heterogeneity within the tumor. Note for example, the darker central region in the tumor (top node) in Fig 37d and 37e, which likely represents a necrotic core. Both modalities show good contrast between viable liver and tumors. The contrast increases for later time points, as is demonstrated in Fig. 38.

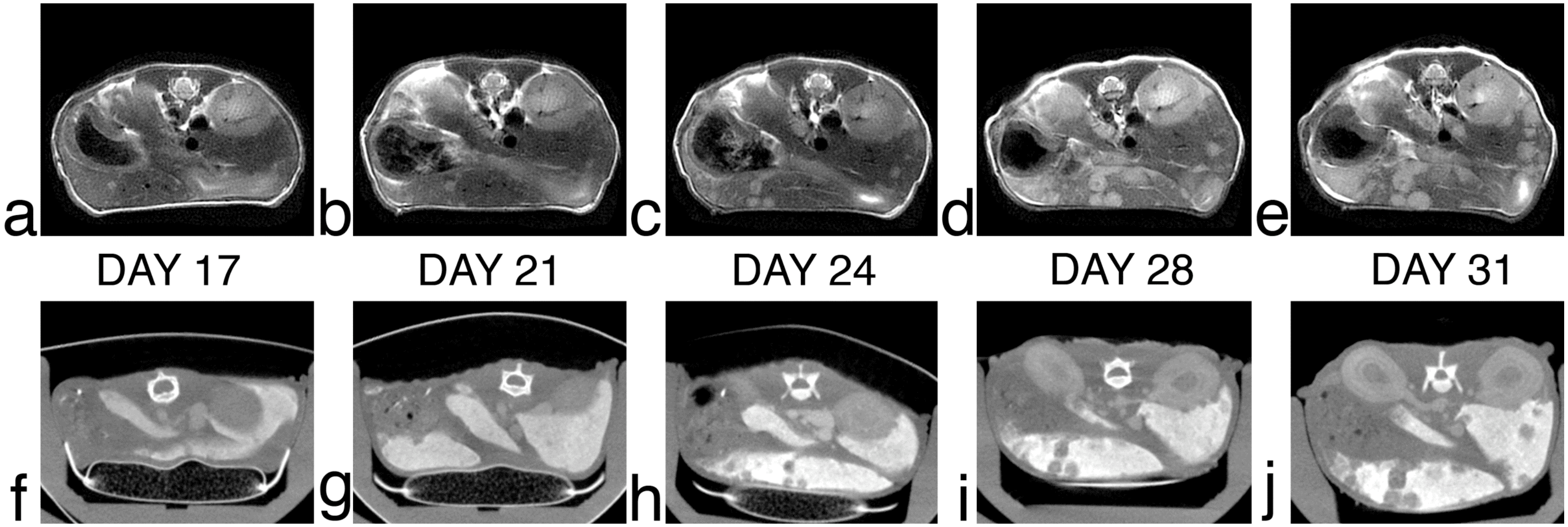

Figure 37: A set of T_2-weighted MR images (top) and contrast-enhanced CT images (bottom) from similar anatomic location from the same mouse showing liver metastases from HT29 colon carcinoma at day 17 (a, f), day 21 (b, g), day 24 (c, h), day 28 (d, i), and day 31 (e, j) post-inoculation. The growth of three metastatic nodes in the lower liver lobe can be followed over the course of the study.

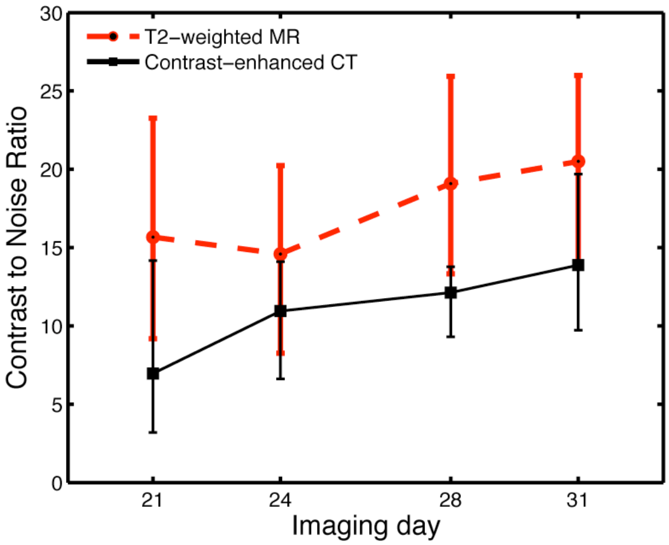

Figure 38: CNR between viable liver and tumors as a function of imaging day for T_2-weighted MR (red) and contrast-enhanced CT (black).

The contrast-to-noise ratio (CNR) for both modalities was calculated according to Eq. (7.1), where SI represents signal intensity.

$$CNR=\left(\frac{|SI_{liver}-SI_{tumor}|}{\sigma_{noise}}\right) \tag{7.1}$$

Figure 38 shows data averaged over three different mice. Six slices with regions of both viable liver and tumors were chosen from each dataset, and three distinct ROIs for liver and tumor were manually selected from each slice to determine the signal intensities for liver and tumor. CNR was calculated for each slice using the standard deviation of the noise for that slice. Thus for a particular imaging day, CNR calculations for 6 different slices for each of the 3 mice were included (a total of 18 measurements). As there exist variations in the rate of tumor growth between animals, there is considerable variability in CNR. Nevertheless, the following two observations can be made from the graph in Fig. 38.

1. The CNR in both modalities shows a gradual increase at later time points.

2. The CNR in the T_2-weighted MR images is higher than that in the contrast-enhanced CT images.

Another animal for which data exist for these corresponding imaging days, was administered a double dose of contrast agent before day 24. If data from that mouse are included in the above plot, the average CNR in the CT images for day 24 increases, while that from the MR images shows a slight decrease, though it is still higher than CT.

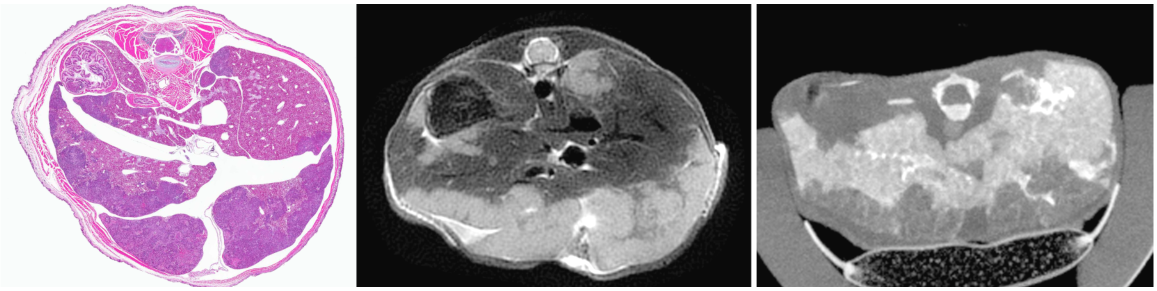

Figure 39: Correlation of conventional histology (left) with in vivo MR (center) and CT (left).

The final set of figures shows the correlation between conventional histology and in vivo MR and CT images. Figure 39 shows an anatomically matching slice from the same mouse 31 days post-inoculation; on the right is an H&E section, in the middle is in vivo T2-weighted MRI, and on the left is in vivo contrast-enhanced CT. The perfusion fixation followed by sectioning with the microtome caused separation of the hepatic lobes. Nonetheless, the correspondence between the three modalities is obvious. The darker, purple regions (tumors) in the histology section match with the hyperintense tumors in T_2-weighted MR and hypointense tumors in contrast-enhanced CT. The heterogeneous region in the lower right hepatic lobe in the MR image correlates with histology where the central tumor node has a necrotic core (and stroma) and is surrounded by viable liver. This demarcation is not as apparent in the CT image.

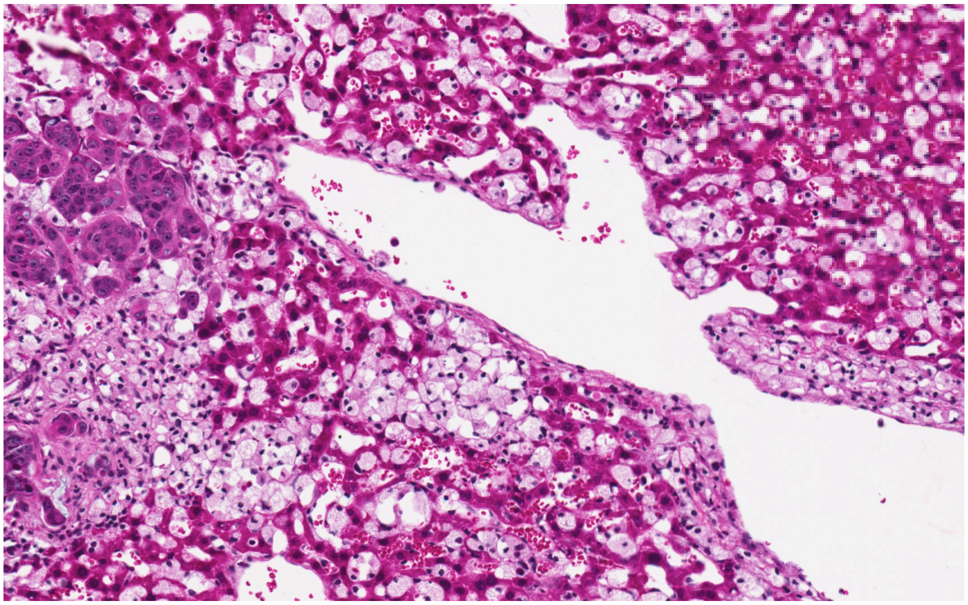

Figure 40: Higher resolution histology section showing tumor (purple), viable liver (red), and contrast accumulation in Kupffer cells (pale pink).

The higher resolution H&E section in Fig. 40 shows tumor, as well as viable liver. The white space is a larger blood vessel in the liver. The pale pink cells are Kupffer cells. The Liposomal contrast agent appears to have accumulated in these cells and hence they have considerably swollen cytoplasm than is usually observed. Additionally, the Kupffer cells also seem to be proliferating in an unnatural manner, particularly around blood vessels. This is in turn causing compression of the normal hepatocytes, though no unusual cell death is observed. The contrast agent also appears to be accumulating in the stoma supporting the liver tumors, though not in the actual tumor cells.

7.4 Discussions

T_2-weighted MR imaging is routinely used for abdominal imaging due to the excellent soft tissue contrast. It is used for detection and characterization of liver lesions clinically (Altbach et al., 2002; Ito et al., 1997; McFarland et al., 1994), as well as in small animals (Baboi et al., 2007; Inderbitzin et al., 2007). T_2 is an inherent tissue property. Thus changes in the tumor microstructure and/or changes in the tumor tissue water content cause changes in the T_2 values (Huang et al., 2008), which are reflected in T_2-weighted MR images.

The 2-shot PROPELLER technique developed in this work is particularly appropriate for the small animal application at high magnetic fields. The PROPELLER trajectory is inherently motion-insensitive and is self-navigated, which allows for motion correction. Thus it was possible to carry out ungated acquisitions in free-breathing mice. The 2-shot modification, along with the high-field correction provided excellent T_2-weighted contrast as well as high SNR. Multi-slice datasets covering the entire abdominal region with a high in-plane spatial resolution of 125 μm and 1mm thick slices were acquired in 30 minutes each.

The MR protocol along with the infrastructure for efficient animal setup was highly conducive for high-throughput studies. With an acquisition time ~6 minutes, the CT protocol was even more so. CT also had a higher spatial resolution of 88 μm, and the datasets were isotropic, thus allowing for resections in any plane. This flexibility is beneficial for tumor visualization and detection during diagnosis. On the other hand, due to superior soft-tissue contrast, anatomical landmarks were much easier to discern in the MR images than in the CT images. The CT data interpretation, at times relied on MR images to localize the anatomy.

Unlike MR that was based on endogenous contrast, CT required the administration of exogenous contrast agent. The blood pool contrast agent, Liposomal Iodine, was injected one day before each imaging session. With this contrast regime it was possible to differentiate viable liver, liver vasculature and liver tumors with a single acquisition as opposed to two separate acquisitions required for dual-phase contrast enhancement to distinguish blood vessels and tumors (Martiniova et al., 2009b).

For animals that already had compromised liver function, twice-weekly contrast injections were a little cause for concern. Conventional H&E section revealed that the contrast agent accumulated in the Kupffer cells in the liver as well as other macrophages throughout the body (Fig. 40). The rate of contrast clearance was slower than the rate of injection, which caused swelling and vacuolation of the macrophages along with excessive proliferation. This in turn caused compression of the healthy hepatocytes, and it is likely that the liver perfusion was compensated. Nonetheless, no unusual cell deaths were observed and no toxicity has yet been reported. In addition to the contrast injections, the CT studies also exposed the mice to repeated radiation, which again is a potential limiting factor in longitudinal studies. MR on the other, being completely non-invasive and non-radioactive had no such limitations.

The sensitivity of the exogenous CT contrast agent was lower than the pathology-dependent T_2 contrast in the MR images, particularly at the early time points (Fig. 36a). The early MR images provide precursory tumor information that is not evident from the CT images. A possible explanation for this could be the contrast uptake in the stroma, which is the connective tissue supporting the tumors. Thus at earlier time points, when the tumors are very small, the signal from the stroma might be more dominant. Additionally, CT images have a negative contrast, i.e. though we are imaging tumors, we are trying to detect the lack of signal. In contrast, MR images have a positive contrast, i.e. objects being imaged, tumors have increased signal intensity. This is typically easier to interpret.

At later time points, both modalities were able to detect liver metastases, but MR had higher CNR than CT. These results confirm those previously reported (Martiniova et al., 2009a), though both modalities, and in particular the CT, have significantly higher values in our study as the protocols were optimized for this application. The CNR measurements from MR showed a larger variability (Fig. 38) than CT. Since T_2 is tissue dependent, the MR images showed increased heterogeneity even within the tumors (Fig. 37) as the disease progressed. Also, for both modalities, the CNR progressively increased at later time points. In MR this can be attributed to the nature of the tumor growth, which at later time points was solid and clearly demarcated. In CT, this increase was most likely due to the accumulation of the contrast agent in the liver due to the repeated injections. This was reaffirmed with the data acquired with a double dose of contrast agent, which caused a 10% increase in the CT CNR. The effect of the CT contrast agent on the MR data was minimal.

7.5 Conclusion

In conclusion, both high-field T_2-weighted MRI and contrast-enhanced microCT were sufficiently simple and fast to permit rapid acquisitions required for high-throughput studies, and were also sufficiently non-invasive to allow multiple scans. We imaged up to 8 mice/day with both MR and CT, for a total of 7 imaging time-points. Each modality has its strengths (and weaknesses). MicroCT has higher spatial resolution and isotropic datasets enabling resections in any plane. With a respiratory-triggered acquisition of ~5 minutes, microCT is more conducive for high-throughput studies than MRI (~30 minutes). T_2-weighted MRI has higher contrast-to-noise ratio than contrast-enhanced microCT (between viable liver and metastatic tumors). Additionally, heterogeneity within the tumors can also be seen in the MR images. We speculate that this represents different stages of tumor growth. We believe that this technique could be used in the future to quantify additional tumor properties in this model, compared to tumor detection alone. Finally, MRI is less invasive than microCT, which requires both contrast injections as well as radiation dose, and is thus more suitable for longitudinal studies.

8. Summary

Non-Cartesian MR Microscopy is a valuable tool for imaging cancer in mouse models. The integration of several factors, including hardware optimization, animal handling procedures and pulse sequence design allows for the translation of clinical MRI techniques to the murine domain. The technique described here represents a robust protocol for high throughput, longitudinal experiments in free-breathing mice for acquiring both structural and functional information with minimal motion artifacts and excellent spatial resolution. Using this technique, the progression of liver metastases was studied in a mouse model of colon carcinoma. Whole body datasets with planar resolution of 125 x 125 μm^2 (1 mm slice thickness) were acquired in ~30 minutes. Novel modifications to the PROPELLER trajectory and reconstruction algorithm afforded the necessary gains in signal and contrast at high-field strengths, and in image quality in the presence of motion. The contrast mechanisms targeted here were T_2-weighted and diffusion-weighted contrast. This work presents new opportunities for studying cancer onset, progression, and therapy response in disease models that have thus far been unrealizable.

Appendix

This appendix consists of documentation relevant to the PROPELLER sequence that is part of the CIVM knowledge base, CIVMCentral.

1. PROPELLER Documentation
2. Running the PROPELLER sequence
3. Installing the PROPELLER Reconstruction

PROPELLER Documentation

PSD: propeller
Author: Prachi Pandit
Date: January, 2010

PROPELLER is a 2D multi-slice sequence that has been developed to enable in vivo whole body imaging in free-breathing mice. More specifically, this sequence is intended to be used as a screening tool for tumor visualization by employing the T2-weighted and diffusion-weighted contrast mechanisms.

PROPELLER is a non-cartesian imaging sequence where data is acquired as a collection of narrow rectangular strips (blades) passing through the center of k-space. The blades are rotated about the k-space origin so that together they cover the whole of the k-space while the central region is sampled by all blades. Due to this oversampling of the k-space center, this sequence is inherently insensitive to motion. In addition, PROPELLER also provides the ability to correct for in-plane (translation and rotation) motion and reject data corrupted by through-plane motion.

This sequence builds on the standard Fast Spin Echo (FSED) sequence provided by GE. The fseD sequence is the fse sequence tailored for our system (larger gradient, lower SAR/dbdt limits)

Prerequisites:

This sequence is an adaptation of the standard FSE sequence and hence knowledge of the implementation of FSE is useful. More information regarding this sequence can be found in standard GE documentation. The source code is in civmEPIC12:/usr/home/ese124/psd12/fseD_diff.

Running the sequence:

- Choose the Fast spin echo - FSEXL option psd name : psd/propeller
- Choose isotropic resolution in the imaging place (opxres =opyres)
- Uncheck the 'Phase Correct' button
- Choose TE to be 'Min Full'
- Choose the appropriate echo train length and bandwidth
- Do the proper Graphics Prescription
- Save and download the sequence
- Go to the Display CVs option and set acqsperblade to 2 if you want to acquire a

blade with two shots (the default is 1)

- Set the correct value for orderinblade (1 = intermediate, 2 = early, 3 = late). Default is intermediate
- Set psd_grd_wait to 215

For step-by-step instructions refer to PropellerforDummies

Variables:

- prop_mode (alwasy set to 1 for PROPELLER)
- opetl : Echo train length
- num_et : Number of echo trains acquired
- num_blades : Number of blade in the image (for one slice)
- acqsperblade : Flag to set number of shots per blade (1 or 2)
- orderinblade : Flag to choose the blade acquisition order (1, 2 or 3)

Data Layout:

The data is presorted and stored in the BAM according to the GE format. One BAM slice location is assigned for an actual acquired slice. Within the BAM slice the data acquired from all blade is stored in the order in which it was acquired. Each blade data is stored in the top-down order (not necessarily in the order it was acquired within the echo train, but sorted in the right order for easier reconstruction).

Reconstruction

Refer to PropellerReconstruction

-- PrachiPandit - 04 Apr 2008

You are here: TWiki>CIVMCentralWeb>CivmSoftwareDocumentation>MrSoftware>

PropellerSequence

r8 - 12 Mar 2010 - 13:27:41 - PrachiPandit

Running the PROPELLER sequence

Start New Series

- (*start a new series for the first scan, you can copy/paste for later scans, but do not copy/paste from fsed*)
- Prone/Head first
- Coil–CIVM0064
- Axial–2D
    - *If you're doing coronal or sagittal scans make sure the FOV is large enough to cover the coil (~5cm)*
- Fast Spin Echo – FSE-XL
    - Psd/propeller - *Choose Extended Dynamic Range*
- TE = min
- TR = 3s (or whatever you want. I try to have it so that all slices fit in one pass)
- ETL = between 4 and 20
- BW = 125
- Freq = Phase = 256 (*you can gave it 128 or 512 too, but make sure that freq and phase are the same*)
- NEX – set this depending on how long a scan you want (*atleast 15-20 mins, usually my scans are 30-40 mins long*)
- Choose FOV / sl thick (*typically 1, can have 0.8*) / sl spacing (*typically 0*)
- Set the # slices in Graphics Rx.
    - *Center the three planes (in-plane needs to be centered, slices can be off but centered is better as you will have higher signal)*

Save – Download

Display CVs –

- Set psd_grd_wait = 215
- If you want to use wider blades (2 excitations per blade) , set acqsperblade = 2
- If you want more flexibility in setting eff_te, set orderinblade to choose central(1, default), early(2) or late echo(3).
- Check min_esp and eff_te (TE)

Download – Manual scan

- In manual scan, set flip angle with TG, Scan TR does not display
- Set R1 to max and R2 to 28/29 (you can actually set this with fsed, these values stay the same for fsed and propeller)

SCAN

Reconstruction

- Delos/Tinos : login – omega (Password – 4.signa!)

Getting the rawdata from kamy

- Using terminal window go to rawdata directory *cd Experiments/*
- Make a new directory for you studies *mkdir My_Study*
- Go to that directory *cd My_Study*
- Copy over the correct raw file in the directory - *getPfile P*****.7*

Matlab recon

- Working directory – /Volumes/CIVMUsers/omega/PropellerReconEngine (this is where you installed the recon code PropellerReconstruction)
- Run Matlab and change current working directory to PropellerReconEngine (see matlab help for set path and changing the current directory).
- On the matlab command prompt, type
  - propLxCorrection('My_Study', 'P*****', 'S*****', 1, 0 , 0)
  - rawdata directory name => My_Study
  - Pfile name (P*****) => your Pfile name (do not add .7 extension)
  - Run number (S*****) => enter your S#
- It will read the header and then prompt you on the matlab command window for
  - Specimen ID => enter it
  - Project ID => enter it
- This will create your reconstructed images on the recon engine big disk (eg delosspace).

Archivedata

Use archiveme pp S# command on the terminal window

> *The archivetag file is written with pp as the creator, if you want that to be different, update it on Line 293 in file readRawHeaderLx.m in the PropellerReconEngine directory.*

-- PrachiPandit - 17 Dec 2009

You are here: TWiki>CIVMCentral Web>CivmSoftwareDocumentation>MrSoftware>PropellerSequence>PropellerforDummies

r3 - 13 Mar 2010 - 17:40:43 - PrachiPandit

Installing the PROPELLER reconstruction

This is a MATLAB reconstruction for the PROPELLER sequence. It consists of 90+ m-files provided by GE and are internally documented. All the files live in the PropellerReconEngine folder.

Prerequisites for the new system for PROPELLER recon installation

- MATLAB
- Ability to connect to the scanners to pull Pfiles (to allow ftp for getPfile)

To install the PROPELLER recon on a new machine, get the recon DVD (*Prachi's Propeller - Dec 15,2009*) from Lucy

- Copy the PropellerReconEngine folder and getPfile (file-script that pulls Pfile from the scanner to the recon mac) into omega's home directory
- Create the Experiments folder in omega's home directory. This folder holds the rawdata (Pfiles) from the scanner.
- You have to modify 2 m-files to get the correct paths for the new machine
  1. propLxCorrection.m
     path declarations right in the beginning of the file (*change references to /prachi/Experiment and delosspace to the appropriate ones for the new machine. These are in the* Get User Input *section*)
  2. readRawHeaderLx.m
     path declarations towards the end of the file where the archive tags are declared (*change references to delos and delosspace to the appropriate ones for the new machine*)
- Make sure /Users/omega is in your path so you can run the getPfile from anywhere on the system. If it is not in your path, you can add it in the .cshrc file by adding the following line:

  `set path = ($path ~omega)`

For step-by-step instructions on running the reconstructions, refer to PropellerforDummies

-- PrachiPandit - 09 Nov 2007

You are here: TWiki>CIVMCentral Web>MagneticResonance>PropellerReconstruction

r6 - 13 Mar 2010 - 17:41:17 - PrachiPandit

References

Ahn, C.B., Cho, Z.H., 1987. A new phase correction method in NMR imaging based on autocorrelation and histogram analysis. IEEE Trans Med Imaging 6, 32-36.

Alsop, D.C., 1997. Phase insensitive preparation of single-shot RARE: application to diffusion imaging in humans. Magn Reson Med 38, 527-533.

Altbach, M.I., Outwater, E.K., Trouard, T.P., Krupinski, E.A., Theilmann, R.J., Stopeck, A.T., Kono, M., Gmitro, A.F., 2002. Radial fast spin-echo method for T2-weighted imaging and T2 mapping of the liver. J Magn Reson Imaging 16, 179-189.

Attenberger, U.I., Runge, V.M., Stemmer, A., Williams, K.D., Naul, L.G., Michaely, H.J., Schoenberg, S.O., Reiser, M.F., Wintersperger, B.J., 2009. Diffusion Weighted Imaging: A Comprehensive Evaluation of a Fast Spin Echo DWI Sequence With BLADE (PROPELLER) k-Space Sampling at 3 T, Using a 32-Channel Head Coil in Acute Brain Ischemia. Invest Radiol.

Baboi, L., Pilleul, F., Milot, L., Lartizien, C., Poncet, G., Roche, C., Scoazec, J.Y., Beuf, O., 2009. Magnetic resonance imaging follow-up of liver growth of neuroendocrine tumors in an experimental mouse model. Magn Reson Imaging 28, 264-272.

Baboi, L.M., Milot, L., Lartizien, C., Roche, C., Scoazec, J.Y., Pilleul, F., Beuf, O., 2007. Characterization of neuro-endocrine tumors in an athymic nude mouse model using dedicated synchronization strategies for T2-weigted MR imaging at 7T. Conf Proc IEEE Eng Med Biol Soc 2007, 2879-2882.

Badea, C., Hedlund, L.W., Johnson, G.A., 2004. Micro-CT with respiratory and cardiac gating. Med Phys 31, 3324-3329.

Blankenberg, F.G., 2008. In vivo detection of apoptosis. J Nucl Med 49 Suppl 2, 81S-95S.

Bloch, F., 1946. Nuclear Induction. Physical Review 70, 460.

Block, W., Pauly, J., Nishimura, D., 1997. RARE spiral T2-weighted imaging. Magn Reson Med 37, 582-590.

Bloembergen, N., Purcell, E.M., Pound, R.V., 1948. Relaxation Effects in Nuclear Magnetic Resonance Absorption. Physical Review 73, 679.

Bottomley, P.A., Foster, T.H., Argersinger, R.E., Pfeifer, L.M., 1984. A review of normal tissue hydrogen NMR relaxation times and relaxation mechanisms from 1-100 MHz: dependence on tissue type, NMR frequency, temperature, species, excision, and age. Med Phys 11, 425-448.

Brindle, K.M., 2003. Molecular imaging using magnetic resonance: new tools for the development of tumour therapy. Br J Radiol 76 Spec No 2, S111-117.

Cai, S.R., Garbow, J.R., Culverhouse, R., Church, R.D., Zhang, W.H., Shannon, W.D., McLeod, H.L., 2005. A mouse model for developing treatment for secondary liver tumors. International Journal of Oncology 27, 113-120.

Carr, H.Y., Purcell, E.M., 1954. Effects of Diffusion on Free Precession in Nuclear Magnetic Resonance Experiments. Physical Review 94, 630-638.

Cassidy, P.J., Schneider, J.E., Grieve, S.M., Lygate, C., Neubauer, S., Clarke, K., 2004. Assessment of motion gating strategies for mouse magnetic resonance at high magnetic fields. J Magn Reson Imaging 19, 229-237.

Chen, F., De Keyzer, F., Wang, H., Vandecaveye, V., Landuyt, W., Bosmans, H., Hermans, R., Marchal, G., Ni, Y., 2007. Diffusion weighted imaging in small rodents using clinical MRI scanners. Methods 43, 12-20.

Choe, K.A., Smith, R.C., Wilkens, K., Constable, R.T., 1997. Motion artifact in T2-weighted fast spin-echo images of the liver: effect on image contrast and reduction of artifact using respiratory triggering in normal volunteers. J Magn Reson Imaging 7, 298-302.

Conturo, T.E., McKinstry, R.C., Aronovitz, J.A., Neil, J.J., 1995. Diffusion MRI: precision, accuracy and flow effects. NMR Biomed 8, 307-332.

de Dios, E., 2002. The use of animal models in cancer research. Clinical and Translational Oncology 4, 55-58.

Degrassi, A., Russo, M., Scanziani, E., Giusti, A., Ceruti, R., Texido, G., Pesenti, E., 2007. Magnetic resonance imaging and histopathological characterization of prostate tumors in TRAMP mice as model for pre-clinical trials. Prostate 67, 396-404.

Delakis, I., Moore, E.M., Leach, M.O., De Wilde, J.P., 2004. Developing a quality control protocol for diffusion imaging on a clinical MRI system. Physics in Medicine and Biology 49, 1409-1422.

Deoni, S.C., Peters, T.M., Rutt, B.K., 2004. Quantitative diffusion imaging with steady-state free precession. Magn Reson Med 51, 428-433.

Devaraj, A., Pipe, J.G., 2009. Elliptical field-of-view PROPELLER imaging. Magn Reson Med 62, 808-814.

DiFrancesco, M.W., Rasmussen, J.M., Yuan, W., Pratt, R., Dunn, S., Dardzinski, B.J., Holland, S.K., 2008. Comparison of SNR and CNR for in vivo mouse brain imaging at 3 and 7 T using well matched scanner configurations. Med Phys 35, 3972-3978.

Fei, B., Wang, H., Meyers, J.D., Feyes, D.K., Oleinick, N.L., Duerk, J.L., 2007. High-field magnetic resonance imaging of the response of human prostate cancer to Pc 4-based photodynamic therapy in an animal model. Lasers Surg Med 39, 723-730.

Ford, N.L., Thornton, M.M., Holdsworth, D.W., 2003. Fundamental image quality limits for microcomputed tomography in small animals. Med Phys 30, 2869-2877.

Frank, L.R., Wong, E.C., Liu, T.T., Buxton, R.B., 2003. Increased diffusion sensitivity with hyperechos. Magn Reson Med 49, 1098-1105.

Gambarota, G., Leenders, W., Maass, C., Wesseling, P., van der Kogel, B., van Tellingen, O., Heerschap, A., 2008. Characterisation of tumour vasculature in mouse brain by USPIO contrast-enhanced MRI. British Journal of Cancer 98, 1784-1789.

Garbow, J.R., Wang, M., Wang, Y., Lubet, R.A., You, M., 2008. Quantitative monitoring of adenocarcinoma development in rodents by magnetic resonance imaging. Clin Cancer Res 14, 1363-1367.

Glover, G.H., Pauly, J.M., 1992. Projection reconstruction techniques for reduction of motion effects in MRI. Magn Reson Med 28, 275-289.

Grimm, J., Potthast, A., Wunder, A., Moore, A., 2003. Magnetic resonance imaging of the pancreas and pancreatic tumors in a mouse orthotopic model of human cancer. International Journal of Cancer 106, 806-811.

Hall, L.D., Sukumar, S., 1984. Rapid Data-Acquisition Technique for Nmr Imaging by the Projection Reconstruction Method. Journal of Magnetic Resonance 56, 179-182.

Henkelman, R.M., Hardy, P.A., Bishop, J.E., Poon, C.S., Plewes, D.B., 1992. Why fat is bright in RARE and fast spin-echo imaging. J Magn Reson Imaging 2, 533-540.

Hennig, J., Nauerth, A., Friedburg, H., 1986. RARE imaging: a fast imaging method for clinical MR. Magn Reson Med 3, 823-833.

Hennig, J., Scheffler, K., 2001. Hyperechoes. Magn Reson Med 46, 6-12.

Hergan, K., Doringer, W., Langle, M., Oser, W., 1995. Effects of iodinated contrast agents in MR imaging. Eur J Radiol 21, 11-17.

Herneth, A.M., Guccione, S., Bednarski, M., 2003. Apparent diffusion coefficient: a quantitative parameter for in vivo tumor characterization. Eur J Radiol 45, 208-213.

Howles, G.P., Nouls, J.C., Qi, Y., Johnson, G.A., 2009. Rapid production of specialized animal handling devices using computer-aided design and solid freeform fabrication. J Magn Reson Imaging 30, 466-471.

Huang, M.Q., Pickup, S., Nelson, D.S., Qiao, H., Xu, H.N., Li, L.Z., Zhou, R., Delikatny, E.J., Poptani, H., Glickson, J.D., 2008. Monitoring response to chemotherapy of non-Hodgkin's lymphoma xenografts by T(2)-weighted and diffusion-weighted MRI. NMR Biomed 21, 1021-1029.

Inderbitzin, D., Stoupis, C., Sidler, D., Gass, M., Candinas, D., 2007. Abdominal magnetic resonance imaging in small rodents using a clinical 1.5 T MR scanner. Methods 43, 46-53.

Inoue, Y., Izawa, K., Tojo, A., Nomura, Y., Sekine, R., Oyaizu, N., Ohtomo, K., 2007. Monitoring of disease progression by bioluminescence imaging and magnetic resonance imaging in an animal model of hematologic malignancy. Exp Hematol 35, 407-415.

Ito, K., Mitchell, D.G., Outwater, E.K., Szklaruk, J., Sadek, A.G., 1997. Hepatic lesions: discrimination of nonsolid, benign lesions from solid, malignant lesions with heavily T2-weighted fast spin-echo MR imaging. Radiology 204, 729-737.

Jansen, S.A., Conzen, S.D., Fan, X., Krausz, T., Zamora, M., Foxley, S., River, J., Newstead, G.M., Karczmar, G.S., 2008. Detection of in situ mammary cancer in a transgenic mouse model: in vitro and in vivo MRI studies demonstrate histopathologic correlation. Physics in Medicine and Biology 53, 5481-5493.

Jemal, A., Siegel, R., Ward, E., Hao, Y., Xu, J., Thun, M.J., 2009. Cancer statistics, 2009. CA Cancer J Clin 59, 225-249.

Johnson, G., Wadghiri, Y.Z., Turnbull, D.H., 1999. 2D multislice and 3D MRI sequences are often equally sensitive. Magn Reson Med 41, 824-828.

Kalber, T.L., Waterton, J.C., Griffiths, J.R., Ryan, A.J., Robinson, S.P., 2008. Longitudinal in vivo susceptibility contrast MRI measurements of LS174T colorectal liver metastasis in nude mice. J Magn Reson Imaging 28, 1451-1458.

Keogan, M.T., Edelman, R.R., 2001. Technologic advances in abdominal MR imaging. Radiology 220, 310-320.

Kim, H., Morgan, D.E., Zeng, H.D., Grizzle, W.E., Warram, J.M., Stockard, C.R., Wang, D.L., Zinn, K.R., 2008. Breast tumor xenografts: Diffusion-weighted MR imaging to assess early therapy with novel apoptosis-inducing anti-DR5 antibody. Radiology 248, 844-851.

Kim, T., Murakami, T., Takahashi, S., Hori, M., Tsuda, K., Nakamura, H., 1999. Diffusion-weighted single-shot echoplanar MR imaging for liver disease. AJR Am J Roentgenol 173, 393-398.

Kinkel, K., Lu, Y., Both, M., Warren, R.S., Thoeni, R.F., 2002. Detection of hepatic metastases from cancers of the gastrointestinal tract by using noninvasive imaging methods (US, CT, MR imaging, PET): a meta-analysis. Radiology 224, 748-756.

Koh, D.M., Collins, D.J., 2007. Diffusion-weighted MRI in the body: applications and challenges in oncology. AJR Am J Roentgenol 188, 1622-1635.

Koh, D.M., Scurr, E., Collins, D.J., Pirgon, A., Kanber, B., Karanjia, N., Brown, G., Leach, M.O., Husband, J.E., 2006. Colorectal hepatic metastases: quantitative measurements using single-shot echo-planar diffusion-weighted MR imaging. Eur Radiol 16, 1898-1905.

Koo, V., Hamilton, P.W., Williamson, K., 2006. Non-invasive in vivo imaging in small animal research. Cell Oncol 28, 127-139.

Laubach, H.J., Jakob, P.M., Loevblad, K.O., Baird, A.E., Bovo, M.P., Edelman, R.R., Warach, S., 1998. A phantom for diffusion-weighted imaging of acute stroke. J Magn Reson Imaging 8, 1349-1354.

Le Roux, P., 2002. Non-CPMG Fast Spin Echo with full signal. Journal of Magnetic Resonance 155, 278-292.

Low, R.N., Francis, I.R., Sigeti, J.S., Foo, T.K., 1993. Abdominal MR imaging: comparison of T2-weighted fast and conventional spin-echo, and contrast-enhanced fast multiplanar spoiled gradient-recalled imaging. Radiology 186, 803-811.

Lyons, S.K., 2005. Advances in imaging mouse tumour models in vivo. J Pathol 205, 194-205.

Mai, W., Badea, C.T., Wheeler, C.T., Hedlund, L.W., Johnson, G.A., 2005. Effects of breathing and cardiac motion on spatial resolution in the microscopic imaging of rodents. Magn Reson Med 53, 858-865.

Malisch, T.W., Hedlund, L.W., Suddarth, S.A., Johnson, G.A., 1991. MR microscopy at 7.0 T: effects of brain iron. J Magn Reson Imaging 1, 301-305.

Martiniova, L., Kotys, M.S., Thomasson, D., Schimel, D., Lai, E.W., Bernardo, M., Merino, M.J., Powers, J.F., Ruzicka, J., Kvetnansky, R., Choyke, P.L., Pacak, K., 2009a. Noninvasive monitoring of a murine model of metastatic pheochromocytoma: a comparison of contrast-enhanced microCT and nonenhanced MRI. J Magn Reson Imaging 29, 685-691.

Martiniova, L., Schimel, D., Lai, E.W., Limpuangthip, A., Kvetnansky, R., Pacak, K., 2009b. In vivo micro-CT imaging of liver lesions in small animal models. Methods 50, 20-25.

Marzola, P., Osculati, F., Sbarbati, A., 2003. High field MRI in preclinical research. Eur J Radiol 48, 165-170.

McConville, P., Hambardzumyan, D., Moody, J.B., Leopold, W.R., Kreger, A.R., Woolliscroft, M.J., Rehemtulla, A., Ross, B.D., Holland, E.C., 2007. Magnetic resonance imaging determination of tumor grade and early response to temozolomide in a genetically engineered mouse model of glioma. Clinical Cancer Research 13, 2897-2904.

McFarland, E.G., Mayo-Smith, W.W., Saini, S., Hahn, P.F., Goldberg, M.A., Lee, M.J., 1994. Hepatic hemangiomas and malignant tumors: improved differentiation with heavily T2-weighted conventional spin-echo MR imaging. Radiology 193, 43-47.

Meiboom, S., Gill, D., 1958. Modified Spin-Echo Method for Measuring Nuclear Relaxation Times. Review of Scientific Instruments 29, 688-691.

Mitchell, M.D., Kundel, H.L., Axel, L., Joseph, P.M., 1986. Agarose as a tissue equivalent phantom material for NMR imaging. Magn Reson Imaging 4, 263-266.

Mook, O.R.F., Jonker, A., Strang, A.C., Veltien, A., Gambarota, G., Frederiks, W.M., Heerschap, A., Van Noorden, C.J.F., 2008. Noninvasive magnetic resonance imaging of the development of individual colon cancer tumors in rat liver. Biotechniques 44, 529-535.

Mori, S., van Zijl, P.C.M., 1998. A motion correction scheme by twin-echo navigation for diffusion-weighted magnetic resonance imaging with multiple RF echo acquisition. Magnetic Resonance in Medicine 40, 511-516.

Moteki, T., Sekine, T., 2004. Echo planar MR imaging of the liver: comparison of images with and without motion probing gradients. J Magn Reson Imaging 19, 82-90.

Mukundan, S., Jr., Ghaghada, K.B., Badea, C.T., Kao, C.Y., Hedlund, L.W., Provenzale, J.M., Johnson, G.A., Chen, E., Bellamkonda, R.V., Annapragada, A., 2006. A liposomal nanoscale contrast agent for preclinical CT in mice. AJR Am J Roentgenol 186, 300-307.

Mulkern, R.V., Melki, P.S., Jakab, P., Higuchi, N., Jolesz, F.A., 1991. Phase-encode order and its effect on contrast and artifact in single-shot RARE sequences. Med Phys 18, 1032-1037.

Mulkern, R.V., Wong, S.T., Winalski, C., Jolesz, F.A., 1990. Contrast manipulation and artifact assessment of 2D and 3D RARE sequences. Magn Reson Imaging 8, 557-566.

Nastiuk, K.L., Liu, H., Hamamura, M., Muftuler, L.T., Nalcioglu, O., Krolewski, J.J., 2007. In vivo MRI volumetric measurement of prostate regression and growth in mice. BMC Urol 7, 12.

Nasu, K., Kuroki, Y., Nawano, S., Kuroki, S., Tsukamoto, T., Yamamoto, S., Motoori, K., Ueda, T., 2006. Hepatic metastases: diffusion-weighted sensitivity-encoding versus SPIO-enhanced MR imaging. Radiology 239, 122-130.

Norris, D.G., Bornert, P., Reese, T., Leibfritz, D., 1992. On the application of ultra-fast RARE experiments. Magn Reson Med 27, 142-164.

Oliva, M.R., Saini, S., 2004. Liver cancer imaging: role of CT, MRI, US and PET. Cancer Imaging 4 Spec No A, S42-46.

Ong, H., Chin, C.L., Wehrli, S.L., Tang, X., Wehrli, F.W., 2005. A new approach for simultaneous measurement of ADC and T2 from echoes generated via multiple coherence transfer pathways. Journal of Magnetic Resonance 173, 153-159.

Pandit, P., King, K., Johnson, G.A., 2008. Abdominal imaging in free-breathing mice using PROPELLER. Proceedings 16th Scientific Meeting, International Society for Magnetic Resonance in Medicine, Toronto, p. 420.

Pandit, P., Qi, Y., King, K.F., Johnson, G.A., 2010a. Reduction of artifacts in T2-weighted PROPELLER in high-field preclinical imaging. Magn Reson Med Submitted.

Pandit, P., Qi, Y., Story, J., King, K.F., Johnson, G.A., 2010b. Multi-shot PROPELLER for high-field MRI. Magn Reson Med In Press.

Peters, D.C., Derbyshire, J.A., McVeigh, E.R., 2003. Centering the projection reconstruction trajectory: reducing gradient delay errors. Magn Reson Med 50, 1-6.

Pipe, J.G., 1999. Motion correction with PROPELLER MRI: application to head motion and free-breathing cardiac imaging. Magn Reson Med 42, 963-969.

Pipe, J.G., Farthing, V.G., Forbes, K.P., 2002. Multishot diffusion-weighted FSE using PROPELLER MRI (vol 47, pg 42, 2002). Magnetic Resonance in Medicine 47, 621-621.

Reimer, P., Jahnke, N., Fiebich, M., Schima, W., Deckers, F., Marx, C., Holzknecht, N., Saini, S., 2000. Hepatic lesion detection and characterization: value of nonenhanced MR imaging, superparamagnetic iron oxide-enhanced MR imaging, and spiral CT-ROC analysis. Radiology 217, 152-158.

Roth, Y., Tichler, T., Kostenich, G., Ruiz-Cabello, J., Maier, S.E., Cohen, J.S., Orenstein, A., Mardor, Y., 2004. High-b-value diffusion-weighted MR imaging for pretreatment prediction and early monitoring of tumor response to therapy in mice. Radiology 232, 685-692.

Sarlls, J.E., Pierpaoli, C., 2008. Diffusion-weighted radial fast spin-echo for high-resolution diffusion tensor imaging at 3T. Magn Reson Med 60, 270-276.

Saxena, V., Gonzalez-Gomez, I., Laug, W.E., 2007. A non-invasive, in vivo technique for monitoring vascular status of glioblastoma during angiogenesis. Technol Cancer Res Treat 6, 641-650.

Schima, W., Kulinna, C., Langenberger, H., Ba-Ssalamah, A., 2005. Liver metastases of colorectal cancer: US, CT or MR? Cancer Imaging 5 Spec No A, S149-156.

Smakman, N., Martens, A., Kranenburg, O., Borel Rinkes, I.H., 2004. Validation of bioluminescence imaging of colorectal liver metastases in the mouse. J Surg Res 122, 225-230.

Stejskal, E.O., Tanner, J.E., 1965. Spin Diffusion Measurements - Spin Echoes in Presence of a Time-Dependent Field Gradient. Journal of Chemical Physics 42, 288-&.

Sun, X., Wang, H., Chen, F., De Keyzer, F., Yu, J., Jiang, Y., Feng, Y., Li, J., Marchal, G., Ni, Y., 2009. Diffusion-weighted MRI of hepatic tumor in rats: comparison between in vivo and postmortem imaging acquisitions. J Magn Reson Imaging 29, 621-628.

Takahashi, M., Kubo, S., Kiryu, S., Gee, J., Hatabu, H., 2007. MR microscopy of the lung in small rodents. Eur J Radiol 64, 367-374.

Torrey, H.C., 1956. Bloch Equations with Diffusion Terms. Physical Review 104, 563.

Vinitski, S., Mitchell, D.G., Einstein, S.G., Rao, V.M., Flanders, A.E., Schweitzer, M.E., Listerud, J., Schnall, M.D., 1993. Conventional and fast spin-echo MR imaging: minimizing echo time. J Magn Reson Imaging 3, 501-507.

Walker, P., Lerski, R.A., Mathur-De Vre, R., Binet, J., Yane, F., 1988. Preparation of agarose gels as reference substances for NMR relaxation time measurement. EEC Concerted Action Program. Magn Reson Imaging 6, 215-222.

Weissleder, R., 2002. Scaling down imaging: molecular mapping of cancer in mice. Nat Rev Cancer 2, 11-18.

Zhao, M., Pipe, J.G., Bonnett, J., Evelhoch, J.L., 1996. Early detection of treatment response by diffusion-weighted 1H-NMR spectroscopy in a murine tumour in vivo. Br J Cancer 73, 61-64.

Zhao, S., Moore, J.V., Waller, M.L., McGown, A.T., Hadfield, J.A., Pettit, G.R., Hastings, D.L., 1999. Positron emission tomography of murine liver metastases and the effects of treatment by combretastatin A-4. Eur J Nucl Med 26, 231-238.

Zhong, J.H., Gore, J.C., Armitage, I.M., 1989. Relative contributions of chemical exchange and other relaxation mechanisms in protein solutions and tissues. Magn Reson Med 11, 295-308.

Zhou, X.H., Liang, Z.P., Cofer, G.P., Beaulieu, C.F., Suddarth, S.A., Johnson, G.A., 1993. Reduction of Ringing and Blurring Artifacts in Fast Spin-Echo Imaging. Jmri-Journal of Magnetic Resonance Imaging 3, 803-807.

Biography

Prachi Pandit

Education

Duke University, *Durham, NC*
Ph. D. in Biomedical Engineering, 2010

Cornell University, *Ithaca, NY*
M. Eng. in Electrical Engineering, 2003

Pune University, *Pune, India*
B. Eng. in Electronics and Telecommunication Engineering, 2002

Awards and Affiliations

Duke Univeristy Biomedical Biomedical Engineering Graduate Fellowship, 2005-2010
International Society of Magnetic Resonance in Medicine (ISMRM), Member, 2007-
ISMRM Education Stipend/Travel Award, 2007-2010
National Talent Search Scholarship, 1996-2002
National Merit Scholar, 1996, 1998

Publication

P. Pandit, S. M. Johnston, Y. Qi, J. Story, B. Hollister, G. A. Johnson, Multi-modal assessment of longitudinal growth of liver metastases in a mouse model of colon carconima, *In Preparation*

P. Pandit, Y. Qi, K. F. King, G. A. Johnson, Reduction of artifacts in T2-weighted PROPELLER in high-field preclinical imaging, *Magnetic Resonance in Medicine, Submitted, December 2009*

P. Pandit, Y. Qi, J. Story, K. F. King, G. A. Johnson, Multi-shot PROPELLER for high-field preclinical MRI, *Magnetic Resonance in Medicine, Accepted, January 2010*

Conference Proceedings

P. Pandit, S. M. Johnston, Y. Qi, J. Story, B. Hollister, G. A. Johnson, Multi-modal assessment of longitudinal growth of liver metastases in a mouse model of colon carconima, *International Society for Magnetic Resonance in Medicine, Joint Annual Meeting ISMRM-ESMRMB, Stockholm, Sweden, May 2010*

P. Pandit, Y. Qi, K. F. King, G. A. Johnson, High-field MRI for non-invasive preclinical imaging in free-breathing mice, *International Society for Magnetic Resonance in Medicine, Joint Annual Meeting ISMRM-ESMRMB, Stockholm, Sweden, May 2010*

P. Pandit, Y. Qi, K. F. King, G. A. Johnson, High-field MRI for non-invasive preclinical imaging in free-breathing mice, *Duke Comprehensive Cancer Center, Annual Meeting, Durham, NC, September 2009*

P. Pandit, Y. Qi, K. F. King, G. A. Johnson, Diffusion-weighted imaging with PROPELLER using distributed diffusion gradients, *ISMRM Workshop on Data Sampling and Image Reconstruction, Sedona, AZ, January 2009*

P. Pandit, K. F. King, G. A. Johnson, Abdominal imaging in free-breathing mice using PROPELLER, *International Society for Magnetic Resonance in Medicine, 16th Scientific Meeting, Toronto, Canada, May 2008*

P. Pandit, K. F. King, G. A. Johnson, In vivo MR imaging of mice at high field strengths, *Fitzpatrick Institute of Photonics, 7th Annual Meeting, Durham, NC, October 2007*